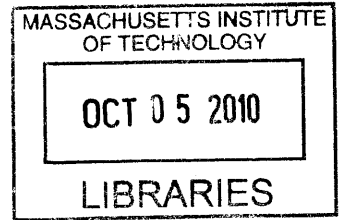# Integrated high-repetition-rate femtosecond lasers at 1.55 μm

by

Hyunil Byun

B.S., Korea Advanced Institute of Science and Technology (2000)
S.M., Massachusetts Institute of Technology (2006)

Submitted to the Department of Electrical Engineering and Computer Science
in partial fulfillment of the requirements for the degree of

Doctor of Philosophy

ARCHIVES

at the

MASSACHUSETTS INSTITUTE OF TECHNOLOGY

September 2010

Author . . . .
Department of Electrical Engineering and Computer Science
June 22, 2010

Certified by . . . .
Franz X. Kärtner
Professor
Thesis Supervisor

Accepted by . . . .
Terry P. Orlando
Chairman, Department Committee on Graduate Theses

Integrated high-repetition-rate femtosecond lasers at 1.55 μm

by

Hyunil Byun

Submitted to the Department of Electrical Engineering and Computer Science
on June 22, 2010, in partial fulfillment of the
requirements for the degree of
Doctor of Philosophy

Abstract

Performance of state-of-the-art, electronic analog-to-digital converters is currently limited by the 100-fs aperture jitter. However, optical sampling can overcome the jitter limit by using femtosecond lasers that have jitter as low as 100 as, which is a three orders of magnitude improvement when compared to electronics.

Currently, most of these lasers exist as bulk or fiber lasers. While such configurations can provide flexibility in order to tailor the behavior of the lasers to specific needs, they are usually as expensive as \$10,000 to \$100,000 and require precisely adjustable mounts and high-quality optical components. To realize the possibility of femtosecond lasers replacing current electronics for unprecedented performance in the future, these lasers must be as compact, robust, and affordable as electronic circuits.

A monolithically integrated mode-locked laser can lower the cost of building such femtosecond lasers and, at the same time, make them less vulnerable to environmental perturbation. This can be achieved by mass-producing them with less expensive materials such as silicon, silicon oxide, or compatible materials. Since all necessary optical components are integrated monolithically on a silicon substrate, bulky and expensive high-precision discrete components can be excluded.

The goal of this thesis is the development of femtosecond lasers that can overcome the limit of electronics and potentially replace them. Possible approaches and current achievements are discussed towards this goal.

Thesis Supervisor: Franz X. Kärtner
Title: Professor

Acknowledgments

First and foremost, I would like to thank my research advisor Prof. Franz X. Kärtner for generous support and thoughtful guidance. I admit that my experiments could not be assembled as one story without his supervision. He also trusted me and approved almost all purchase requisitions for the lab experiments, which enabled me to enjoy implementing many different ideas in the lab.

I express thanks to Prof. Erich P. Ippen for helpful advice not only on general understanding of mode-locked lasers, but also on details of the experiment setup. His appreciation on even small results encouraged me to maintain the research efforts. I also thank Prof. Kärtner and Ippen for their opening house and arranging the group party every year, which was wonderful experience to get closer with other group members.

I thank Prof. Rajeev Ram for serving on my committee despite his limited time. His class on semiconductor and optoelectronics equipped me with the insight into the interaction between light and semiconductor. I believe what I learned in the class will be very useful for my next position at Samsung Electronics.

I thank my academic advisor Professor Haeseung Lee for warm advice on my academic life.

I would like to thank all members of Optics and Quantum Electronics group for generous discussions, suggestions, equipment loans, and good friendship. Special thanks to Michelle Sander for taking over what I've been doing and improving it further. Hanfei Shen designed the SBR that enabled the femtosecond mode-locking of numerous lasers. Gale Petrich fabricated the designed SBR that worked beautifully. Orit Shamir and Sheila Nabanja helped with cleaving and thinning the SBR samples. I thank Prof. Leslie Kolodziejski for leading all activities toward high quality SBRs. Ali Motamedi in Prof. Ippen's group put considerable efforts in pump probe characterization of the in-house SBRs and the extracted SBR parameters were essential in analyzing the laser behavior. I thank Michelle Sander, Jonathan Birge, Amir Nejad-malayeri, and Dorothy Fleisher for proofreading my thesis and providing invaluable

suggestions.

I thank our administrative assistants Dorothy Fleisher and Donna Gale for their hidden efforts to keep the lab running smoothly. They also always welcomed my requests on purchase, reimbursement, and so on.

Joe Schmulovich, Sergey Frolov, Amir Hanjani, and Allan Bruce at CyOptics did great job in fabricating the wonderful Er-waveguide devices.

Peter O'Brien at the MIT Lincoln Laboratory provided high quality dielectric coatings on SBRs as pump-reflective coating and enabled femtosecond GHz-fiber lasers. I also thank T.Y. Fan for allowing the coating runs.

I thank Jonathan Birge for initially building the spectrally integrated interferometry setup for dispersion measurement. He also did not spare advice and lab support to improve the measurement setup.

Thanks to Michael Watts at Sandia National Laboratory who provided integrated Sagnac loop devices with fast phase modulators to enable low-jitter RF signal extraction. I thank Jungwon Kim for initial design of the chip and the experiment setup and Amir Nejadmalayeri for collaboration in the experiments to examine the devices.

I appreciate Gilberto Abram's effort on the MATLAB code that implements the Hankel transformation for beam propagation simulation.

This thesis would not have been possible unless we had funding from AFOSR and DARPA. I also thank Korea Foundation for Advanced Studies for financial supports for my study at MIT.

I thank my family, my parents, my sister's family and my mother-in-law for their love and support. In particular, I thank my wife, Soonmin, for being such a wonderful friend and understanding wife. And thanks to my daughter for being a happy toddler and giving us smile. I thank pastor Tae Kim and other members in First Korean Church in Cambridge for their prayer. I thank colleagues in KGSA-EECS for encouraging me and attending my defense.

Last but not least, I owe my deepest gratitude to the Lord for His grace.

Contents

List of Figures

14

15

16

19

20

THIS PAGE INTENTIONALLY LEFT BLANK

List of Tables

THIS PAGE INTENTIONALLY LEFT BLANK

Chapter 1

Introduction

1.1 Motivation and statement of problem

The performance of state-of-the-art, electronic analog-to-digital converters (ADCs) is currently limited by the 100-fs aperture jitter [11, 12]. At a given effective number of bit (ENOB) or resolution, the processable input signal bandwidth is limited due to the uncertainty of the sampling clock. For example, the highest signal frequency that allows 7.8 ENOB for current electronic ADCs is 2 GHz. However, optical sampling can overcome the jitter limit by using femtosecond lasers that have jitter as low as 100 attosecond (as), which is three orders of magnitude improvement when compared to current electronics. For example, a femtosecond laser with a 30-fs jitter enables resolution of 8 bits at 40-GHz sampling rate [13]. Femtosecond lasers that generate a stable train of pulses as short as a few femtoseconds up to several hundred femtoseconds with very low timing jitter, enable emerging applications, such as frequency metrology, high-speed sampling, and ultrafast diagnostics.

Currently, most of these lasers exist as bulk or fiber lasers. Although such configurations can provide flexibility in order to tailor the behavior of the lasers to specific needs, they are usually as expensive as $10,000 to $100,000 and require precisely adjustable mounts and high-quality optical components. To realize the possibility of femtosecond lasers replacing current electronics for unprecedented performance in the future, these lasers must be as compact, robust, and inexpensive as electronic

circuits.

A monolithically integrated mode-locked laser can lower the cost of building such femtosecond lasers and, at the same time, make them less vulnerable to environmental perturbations. This can be achieved by mass-producing them with cheaper materials, such as silicon, silicon oxide, or compatible materials. Since all necessary optical components are integrated monolithically on a silicon substrate, bulky and expensive high-precision discrete components can be avoided. As long as the yield can be improved beyond a specific level, the price per unit will be dramatically reduced by several orders using mass production. For example, the manufacturing cost of the waveguide laser/interleaver chip discussed in Section 3.3.3 can be less than \$30 per chip for a quantity larger than 100,000[1]. This cost savings will promote the use of femtosecond lasers in general.

The goal of this thesis is the development of femtosecond lasers that can overcome the jitter limit of electronics. An approach to achieve this goal is discussed in the next section.

1.2   The approach

The laser sources that fulfill the expectation in Section 1.1 will possess the following characteristics.

- A pulse repetition rate of multi-GHz: this is needed for various applications, such as high data rate sampling, ultrafast measurement techniques, and microwave photonics.

- A low timing jitter and femtosecond pulse duration: this is needed for a precise and stable pulse source. A shorter pulse width ensures broad optical spectrum.

- Compactness, robustness, and affordability: this is needed to enable an efficient prototype-to-market transition without challenging current production methods and techniques.

[1]The calculation assumes that the waveguide chip is fabricated using Er-waveguide and Ge-waveguide to allow a smaller footprint.

1.2.1 Wavelength range and gain medium

We first consider possible laser emission wavelength that will enable the above-mentioned characteristics. There is a wide choice of laser gain media, such as laser crystals and glasses (e.g.: Nd:YAG, Ti:sapphire, Er:YAG, Er:glass, Yb:glass) and semiconductor quantum wells, laser dyes, gas mixture (e.g.: CO_2). Different gain media usually result in different emission wavelength ranges. For the following reasons, 1.5-1.6 μm is chosen as our wavelength range and Er:glass is used as the gain medium:

1. Compatibility with telecommunication wavelength range.

   Fabrication of a laser requires not only cavity components, but also auxiliary components, such as couplers, wavelength-division multiplexers (WDM), isolators, etc. A laser that operates near the telecommunication wavelength can benefit from reliable commercial components that are readily available. In addition, signals over such a wavelength range propagate through optical fiber with very low loss, thus enabling long-haul transmission.

2. Low timing jitter produced.

   Er:glass has a long upper-state lifetime. The long upper-state lifetime of Er-doped glass results in the strong suppression of pump noise and helps to minimize the timing jitter.

3. Available integration technology.

   An Er-doped waveguide can be defined on a silicon wafer by using an Er-doped glass film of only a few μm thickness [14]. This technology will play an important role in the monolithic integration of high-quality laser sources. The integration will be an effective solution to decrease the manufacturing cost of such lasers by mass production.
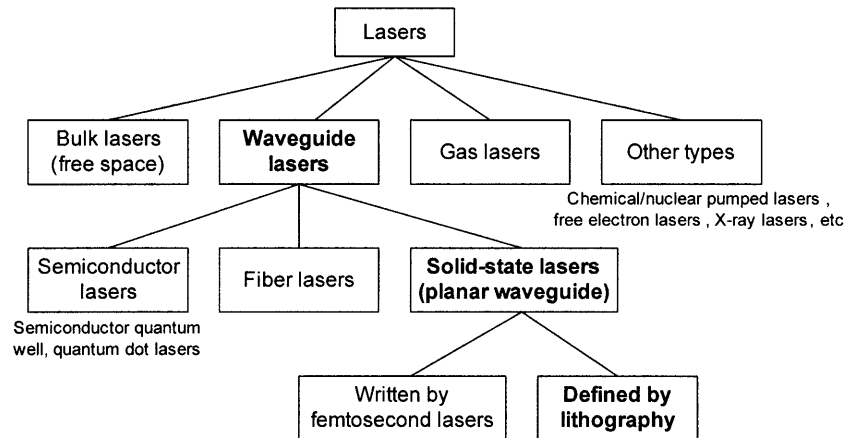
Figure 1-1: Laser classification by gain material and cavity configuration. The best choices are indicated with shaded boxes.

1.2.2 Laser configuration

A variety of different lasers generate 1.5-1.6 μm wavelengths. The classification shown in Figure 1-1 visualizes the different options. In the first-level classification, only bulk lasers and waveguide lasers are considered, since gas lasers and others generally do not support our wavelength range.

In terms of bulk lasers $\sim$1.55 μm, considerable research has been done on solid-state lasers that employ crystal- or glass-based gain media. ErYb:glass-based lasers demonstrated femtosecond pulse generation with a maximum repetition rate of 170 MHz [15, 16]. Zeller *et al.* built a 77-GHz ErYb:glass laser [17], but here we consider only lasers that form sub-picosecond pulse trains, since the jitter is closely related to the pulse width. By using a different gain material, Cr^{4+}:Yag crystal, Leburn *et al.* demonstrated a 81-fs pulse train at a repetition rate of 4 GHz [18]. These lasers may produce a high-repetition-rate pulse train with low jitter, but they are bulky and expensive, and sensitive to their environment. In addition, some materials, such as Cr^{4+}:Yag, are not yet fully developed and they are difficult to integrate.

The waveguide lasers are categorized in the following:

1. Semiconductor lasers

   Near the telecommunication wavelength, there are monolithically integrated

30

semiconductor diode lasers based on III-V materials. Deriyagin *et al.* demonstrated pulses with durations as short as 650 fs at 110-GHz repetition rate from a monolithic mode-locked diode laser, and Lohe *et al.* produced 600-fs pulses at a 42-GHz repetition rate by using a more advanced device structure [19, 20]. However, the timing jitter of the mode-locked quantum well lasers is reported to be in ps-range [21] and even the mode-locked quantum dot lasers with improved jitter performance show several hundred fs of timing jitter [22].

2. Fiber lasers

Fiber lasers user optical fibers as a gain medium, which are doped with rare earth ions, such as erbium, ytterbium, or neodymium. Due to the small mode area, the gain efficiency is high and the laser can operate at a lower threshold than bulk lasers. Fiber lasers can be constructed at a much lower cost, especially when minimum free-space optics are used. Several different investigations have demonstrated low-jitter femtosecond pulse generation by using optical gain fibers [23, 24]. Although fiber lasers can be very compact and produce high-quality pulses, planar waveguide lasers will enable more compact and reliable laser devices.

3. Planar waveguide lasers

While inheriting the fundamental characteristics of fiber lasers, such as low noise and moderate power efficiency, planar waveguide lasers are more compact and stable than fiber lasers, and they can also lower the manufacturing cost per laser for large quantities. In addition, lasers based on planar waveguide technology can be integrated with other optical elements, such as multiplexers, filters, tap couplers, or mode adaptors. Even electronic circuits using CMOS technology can potentially be integrated with these optical devices.

The planar waveguides can be either written on a rare-earth-ion-doped bulk material by using femtosecond lasers, or defined by using conventional lithography. The former method permits low-cost and fast prototyping, but all lasers based on such waveguides require free-space optics in the cavity because they

31
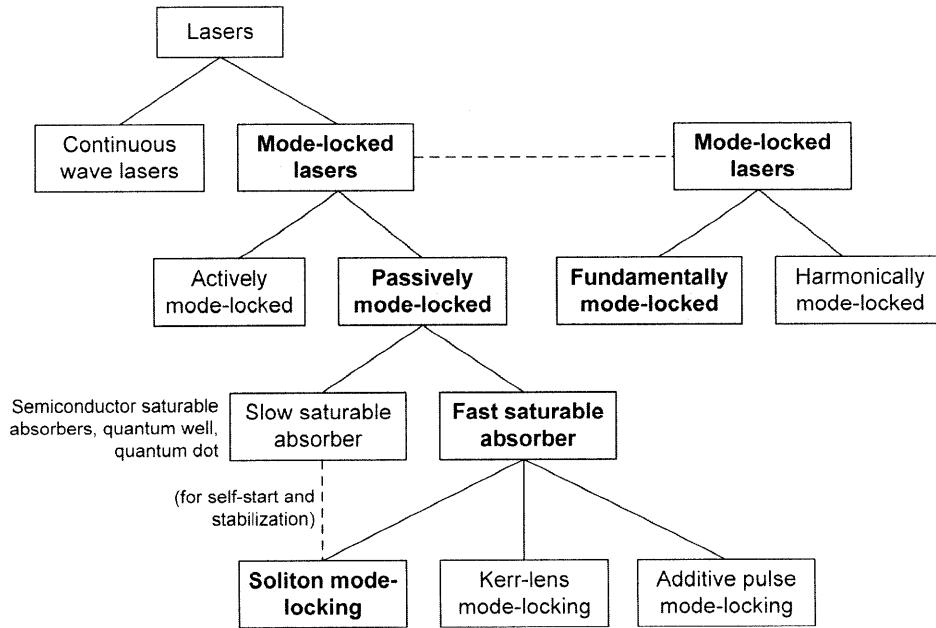
Figure 1-2: Laser classification by output type and mode-locking method. The best choices are indicated with shaded boxes.

can not be integrated into the bulk material where the gain waveguides were written [25, 26]. On the other hand, the lithographically defined waveguides can be easily integrated with other passive optical components, which satisfies the need for low-cost and robust femtosecond lasers, and opens the door to complex, hybrid monolithical optoelectronic systems in the future.

For the above reasons, we have chosen planar waveguide lasers defined by conventional lithography. The next subsection discusses how a femtosecond pulse train can be generated.

1.2.3   Mode-locking method

Many different devices and methods of mode-locking a laser have been demonstrated in order to generate an optical pulse train. (Figure 1-2)

A laser can be either fundamentally mode-locked or harmonically mode-locked. This depends on whether its cavity contains a single-pulse or multiple, regularly spaced, pulses traveling inside. In harmonic mode-locking, a pulse is split into multiple

pulses, for example, by placing a partial reflector at a proper position. Although this technique can apply to mode-locking at a high repetition rate that reaches multi-GHz, it is often difficult to maintain constant spacing between two consecutive pulses, thus resulting in increased timing jitter, which is not appropriate for our application. For this reason, only fundamentally mode-locked lasers will be considered in this thesis.

Active mode-locking uses an amplitude modulator inside the cavity to change the loss with a rate equal to the laser round-trip frequency, thus resulting in a pulse train. Although it is relatively simple to design and implement, active mode-locking has several limitations. One major disadvantage of active mode-locking is that it is difficult to scale down the pulse width, which generally ranges from several picoseconds to tens of picoseconds.

On the other hand, in passive mode-locking, a device with intensity-dependent loss is placed in the cavity [27]. If the loss decreases with higher intensity, pulse formation is favored. Passive mode-locking generates much shorter pulses than active mode-locking, since the pulse inside the laser modulates itself more rapidly than what would be possible with active modulation. Devices with intensity-dependent loss are generally called saturable absorbers. Depending on how fast the saturable absorption recovers after saturation by a single pulse, it is classified as either a slow saturable absorber (SSA) or a fast saturable absorber (FSA). The SSA has a recovery time longer than the generated pulse, while the FSA has a shorter recovery time [28].

The SSA is generally implemented by a semiconductor saturable absorber mirror [29], which is a compact semiconductor device with widely adjustable parameters that mode-locks various kinds of lasers. In passive mode-locking that uses an SSA, the generated pulse width is usually limited from one to several picoseconds. In addition, when the absorber parameters are inappropriate, the laser can operate in Q-switched mode-locking, where the pulse train is modulated over multiple roundtrips in the cavity.

The FSA is often referred to an artificial saturable absorber that uses a nonlinear phase shift. Kerr lens mode-locking, additive pulse mode-locking, and nonlinear polarization rotation mode-locking generates femtosecond pulses, based on the FSA

mechanism. As one way to exploit the nonlinear phase shift, soliton mode-locking that balances the nonlinear phase shift with cavity dispersion is a successful candidate. When compared to other methods, such as Kerr lens mode-locking or nonlinear polarization rotation, the soliton mode-locked laser can be much simpler, since no additional control is necessary once the cavity itself has proper material properties. Particularly, given that we chose the planar waveguide type laser, the soliton formation can benefit from the small mode area of the waveguide that will create relatively high nonlinearity.

In this thesis, the soliton formation is pursued in order to generate pulses as short as possible and, as a result, to minimize the timing jitter of output pulses. As a means to initiate and stabilize the soliton formation, semiconductor saturable absorbers will be used.

1.2.4 Summary

A femtosecond laser with high repetition rate (multi-GHz) and low timing jitter of a few femtoseconds will be built using the laser technology described below. This laser is expected to satisfy the characteristics described in the beginning of this section.

1. Emit telecommunication wavelengths ($\sim$1.55 μm).

2. Employ Er-doped planar waveguide technology for monolithic integration.

3. Fundamentally mode-locked by soliton formation

1.3 Applications

The photonic analog-to-digical convertors (ADCs), shown in Section 1.3.1, is the primary application of the laser specified in Section 1.2 because the laser's low timing jitter is critical to the application. Although this work has been motivated by high-speed optical sampling for the photonic ADC application, the integrated femtosecond laser at 1.55 μm can benefit other applications, which are briefly described in Sections 1.3.2 through 1.3.4.
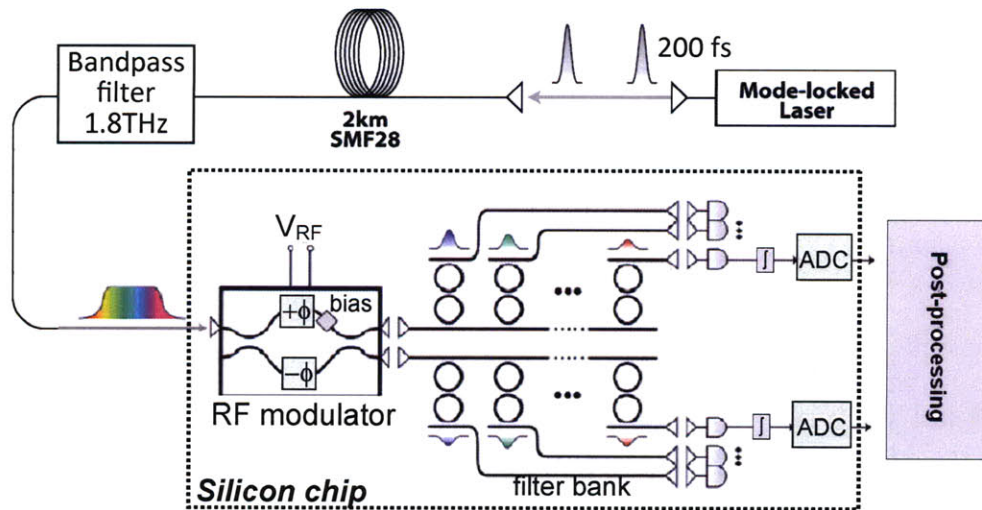
Figure 1-3: High-speed, high-resolution optical sampling system [2]. The mode-locked laser provides a low-jitter pulse train that is chirped and encrypted with the signal to be sampled.

1.3.1 Photonic analog-to-digital conversion

The layout of the photonic ADC system is sketched in Figure 1-3. The high-speed, high-resolution photonic ADC has been investigated by multi-disciplinary research teams at MIT sponsored by DARPA. The major goal is to achieve >8 bit resolution at 40 Gbps sampling bandwidth, which is beyond electronic capabilities. The high-speed signal is parallelized into multiple channels of lower speed signals by using wavelength division multiplexing on silicon chips.

A low-jitter pulse train that is generated by a mode-locked laser passes through 2-km SMF-28 fiber. In this way the pulses are chirped over time and there is continuous coverage between consecutive pulses. The chirped pulses are modulated by a Mach-Zehnder (MZ) modulator whose drive voltage is the signal to be sampled. The modulated chirped signal is demultiplexed into N channels through filter banks by using second-order ring resonators. Each channel can be processed through a detector array followed by low-rate electronic ADCs, and the digitized bitstream from each channel is serialized for the final output. This approach allows an improvement of the sampling rate over what is available in electronic ADCs by a factor of N.

35
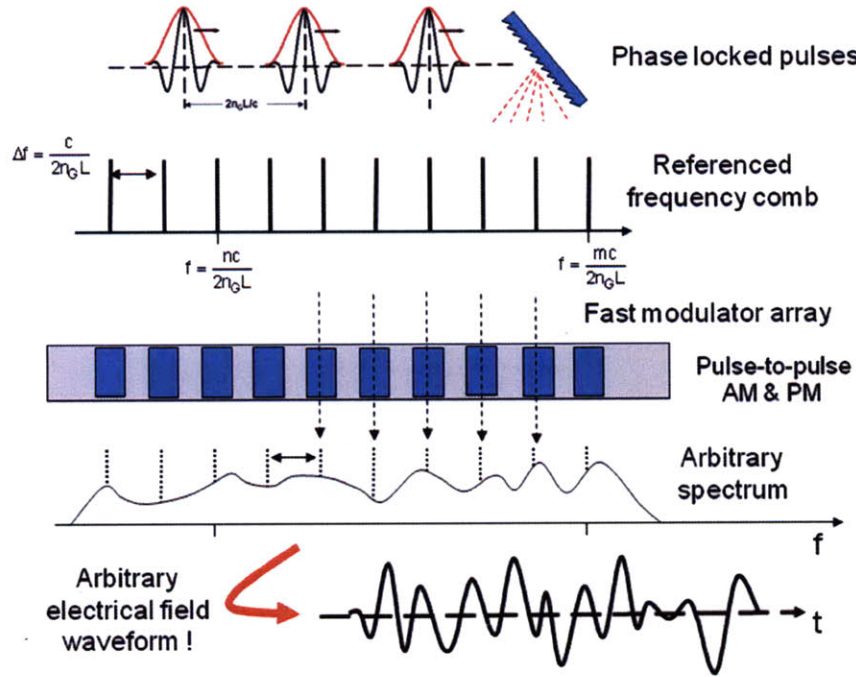
Figure 1-4: Optical arbitrary waveform generation [3].

More detailed technologies on each component of the photonic ADC can be found in Holzwarth *et al.* [2].

1.3.2 Optical arbitrary waveform generation (OAWG)

The generation of arbitary optical waveform consists of the following components, as shown in Figure 1-4:

1. An optical oscillator with stabilized phase to generate the frequency comb.

2. A demultiplexing system to separate the frequencies in the comb.

3. A system to adjust the amplitude and phase of each frequency.

4. A multiplexer to recombine the frequencies.

The femtosecond lasers in this thesis can be used to develop an oscillator for OAWG. The pulse train from the oscillator should have not only stable amplitude,
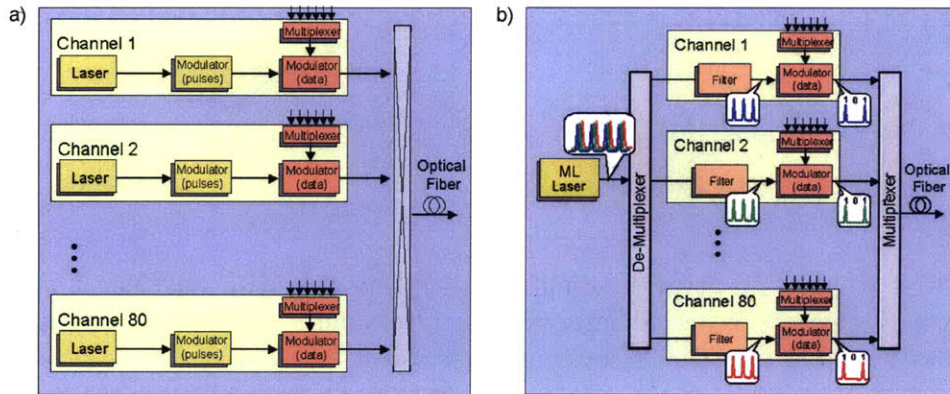
Figure 1-5: Comparison between (a) conventional dense wavelength division multi-pelxing (DWDM) system and (b) future DWDM system. In the future, a mode-locked (ML) laser will replace the current array of discrete lasers and reduce the cost of building a DWDM system [4].

but also stable frequency and phase under the pulse envelope. A separate investigation of a phase-stabilized femtosecond laser at 1.55 μm is being conducted by David Chao and Jonathan Morse in the Optics and Quantum Electronics Group at MIT's Research Laboratory of Electroncis [30].

1.3.3 Cost-efficient optical communication system

The high-repetition-rate mode-locked laser is an attractive multi-wavelength source for optical communication. Conventional optical communication systems employ tens of distributed-feedback (DFB) lasers to transmit data over C-band from 1530 nm to 1565 nm. Figure 1-5 compares the conventional and future transceivers for optical communication. One mode-locked laser that covers the same band and a de-multiplexing filter array can replace all DFB lasers in the transceiver and significantly reduce the system cost. The cost reduction will have a stronger impact when the other components, such as filters, modulators, or multiplexers, are integrated, based on electronic-photonic integrated circuit (EPIC) technologies, as shown in Section 1.3.1.

The optical communication transceiver is one of many examples where a mode-locked laser can substitute for several tens of DFB lasers. An optical interconnect is
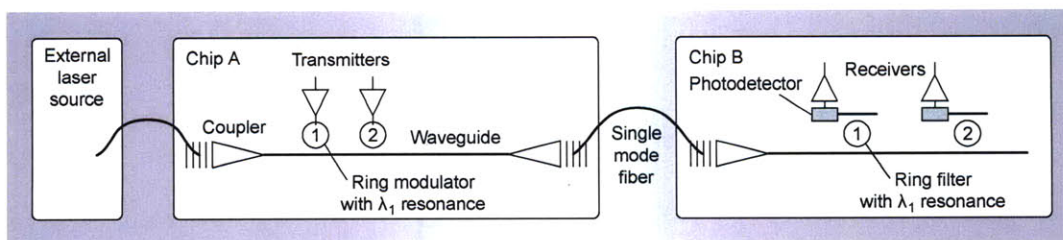
Figure 1-6: Two point-to-point photonic links implemented with wavelength division multiplexing. One mode-locked laser with a filter bank can replace the array of external laser sources in order to cover multiple wavelengths [5].

one such example [5]. Processors already include tens to hundreds of cores in one chip, and the memory bandwidth should increase correspondingly so that a greater number of cores will enhance the performance. The photonic link, where the electrical signal is converted to an optical signal, is transmitted over the waveguide and converted back to an electrical signal by a photodetector. This can produce memory bandwidth that is not possible with copper wires. The transmitter of a photonic link requires a light source, usually a laser source with a narrow bandwidth around a specific wavelength. Similar to the communication system shown above, a mode-locked laser can substitute for the individual laser sources with different center wavelengths. Thus, the mode-locked laser can reduce the chip dimension and the manufacturing cost.

1.3.4 Characterizing the low-jitter property of superconducting nanowire single photon detectors

Single photon detectors using superconducting nanowire (SNSPDs) have advantages when compared to other mature technologies, such as photo-multipliers or single-photon avalanche detectors (SPADs), because the single photon detection occurs over a very broad wavelength from gamma ray to infrared. SNSPDs also provide low noise (no known intrinsic noise source reported [31]) and low jitter <100 ps. The low-temperature requirement to maintain the SNSPD under superconducting conditions may be a weak point, but its unique property of high detection efficiency and low timing jitter is broadening the applications. SNSPDs were first commercialized in

38
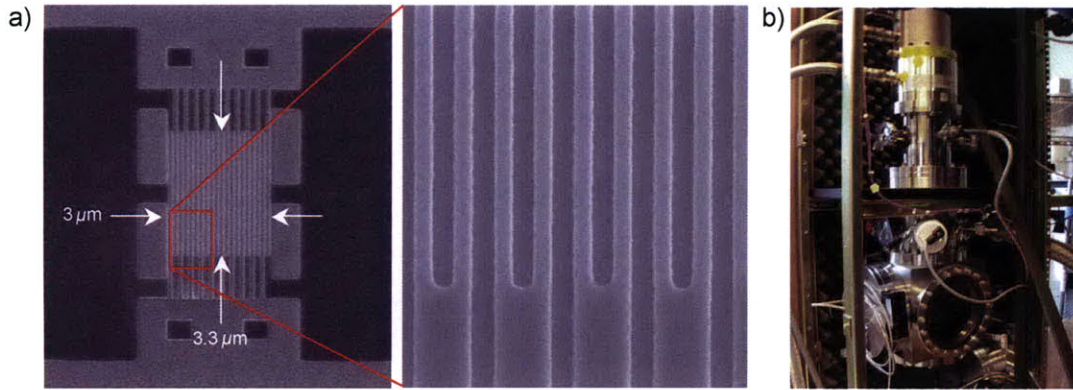
Figure 1-7: (a) Scanning-electron micrograph of the electron-beam resist pattern used to define the meander structure of the detectors. This particular device has a wire width of 100 nm, with 100 nm gaps between the wires [6]. (b) The two-stage cryocooler for the testing of superconductive nanowire single-photon detectors [7]. Our mode-locked femtosecond lasers can be used to measure the jitter of the superconducting nanowire detectors.

circuit fault identification systems by detecting infrared photons [32] and research area such as quantum key distribution has adopted the SNSPD [33]. Introductory articles to the SNSPDs is found in Kerman *et al.* [6] and Dualer [34].

A typical implementation of the SNSPD and an experimental setup used to test it is shown in Figure 1-7. Our mode-locked femtosecond lasers can be used to measure the jitter of the SNSPD, because sub-picosecond pulses are required for the measurement, which is due to the low-jitter property of the SNSPD. A 72-MHz soliton Er-fiber laser with a pulse width of 340 fs was built in a 8"×6"×2" case to test a packaged SNSPD at Prof. Karl Berggren's group at MIT [35].

1.4   Thesis outline

Chapter 2 introduces the available technologies for planar waveguides and discusses the effort to achieve soliton mode-locking at a repetition rate of 400 MHz by using a limited set of waveguide devices.

Chapter 3 examines several options to increase the repetition rate of femtosecond pulses to several GHz while using the same waveguide technologies and summarizes

recent progress in this area.

Chapter 4 addresses soliton fiber lasers that use a commercially available Er-doped fiber. Such lasers were constructed to demonstrate the generation of solitons through a anomalously dispersive cavity, but they also served as compact femtosecond laser sources that can be built from off-the-shelf components. The performance and the technical details of the Er-fiber lasers are demonstrated.

Chapter 5 describes the method of measuring dispersion for different types of samples, such as fibers, planar waveguides, and thin films. The dispersion of laser cavity elements is critically important for soliton formation. Two different approaches used to measure the dispersion are explained in separate sections: spectrally resolved interferometry and spectrally integrated interferometry respectively.

Chapter 6 discusses an experiment in which the low-jitter characteristic of a mode-locked laser is transferred into a microwave signal by using an Sagnac-loop with phase modulators integrated on a silicon wafer.

Chapter 2

Er-doped waveguide laser

2.1 Waveguide characteristics

This section summarizes the characteristics of the planar waveguides used in the integrated femtosecond lasers. The waveguide chips have been designed in collaboration with CyOptics (South Plainfield, NJ) who also did the fabrication.

Planar waveguides usually contain a lower cladding, a core and an upper cladding. All three layers, made of silica glass, are deposited on top of a silicon wafer that functions as a stable handle and heat sink. The core layer is doped with impurities to raise the index higher than the surrounding cladding and thus to enable a waveguide structure. The dopant can be germanium or phosphor for a passive waveguide, and erbium for an active gain waveguide. Erbium ions are doped into aluminosilicate glass, rather than pure fused silica, to exploit better solubility of erbium ions. Fused silica glass shows a low solubility for erbium ions and limit the concentration due to the quenching effects from clustering of dopant ions.

A planar waveguide is fabricated in the following procedure. First, a SiO_2 lower cladding layer is established on a Si wafer to isolate the guided mode from the high index material, that is, the Si wafer. The core layer material is RF-sputtered onto the SiO_2 layer with dopants. Using conventional lithography, waveguides are defined and SiO_2 upper cladding of ~ 10 μm thickness is deposited on top. A scanning electron micrograph of the phosphor-doped waveguide is shown in Figure 2-1. Note that the

41
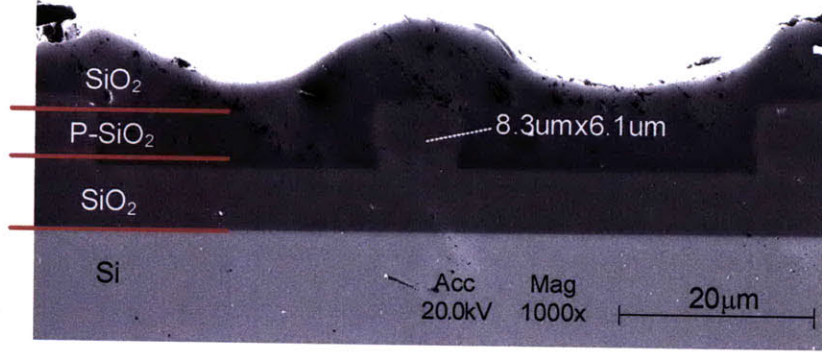
Figure 2-1: Scanning electron microscope (SEM) image of the phosphor-doped waveguide.

	width	height	index contrast	bending radius
P-doped fused silica	$\geq 3~\mu$m	$7~\mu$m	0.75%	>6-7 mm
Ge-doped fused silica	$\geq 2.5~\mu$m	$4~\mu$m	1.5%	>1-2 mm
Er-doped aluminosilica	$\geq 2~\mu$m	1.2-1.5 μm	10%	>0.10-0.15 mm

Table 2.1: Comparison of available planar waveguides

upper cladding layer is wavy and it traces the trench-like shape around the waveguide structure.

Table 2.1 compares three different types of planar waveguides available from Cy-Optics. The higher the index contrast is, the thinner the waveguide becomes to provide as high loss as possible for higher-order modes. Different types of waveguides can coexist in one chip through a proprietary transition region. In a single chip, the target height of each type of waveguide is kept identical, while the width can vary as needed. However, the width of the waveguides mostly should be larger than 3 μm to keep the field strength below a specific point at the waveguide walls for a reasonably low scattering loss. The actual height may vary ~$\pm$10% for various positions on a wafer.

2.1.1 Er-doped waveguide (active section)

Er-doped waveguides are attractive candidates for the gain medium of an integrated mode-locked laser because they can be built by using only silicon-compatible fabrication processes. Several structures of planar optical waveguides doped with Er ions

42
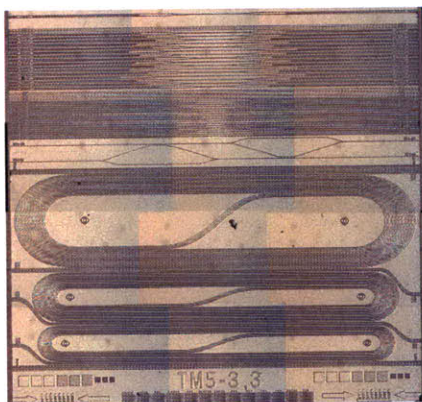
Figure 2-2: Microscope image of the erbium waveguide chip. 2 cm × 2 cm.

were reported [36, 37, 38, 39, 14, 40].

The microscope image of the Er-doped waveguide chip is shown in Figure 2-2, with a dimension of 2 cm × 2 cm. In the lower half part, several track-shaped waveguides are shown. Each track corresponds to a waveguide with different lengths, from 2 cm to 26 cm. In each length, a bundle of four waveguides with different cross-sectional areas are defined parallel. The cross-sectional dimension ranges from 2 μm × 1.2 μm to 5 μm × 1.2 μm.

The Er-doped waveguide chip (Figure 2-2) is characterized for single pass gain (SPG) to verify the possibility of whether it can be used as a gain medium of a laser. The measured single pass gain for a 2-cm long 5-μm wide waveguide is plotted in Figure 2-3. With 80-240 mW of pump power, the single pass gain curves are measured for an input signal at -21 dBm over 1520-1580 nm. The curves show that the gain peaked near 1535 nm. The peak gain was 1.8 dB/cm, which proves that the erbium-doped waveguide can be used as a gain medium of an on-chip laser.

The dispersion of Er-doped waveguides is measured by using a whitelight interferometry in frequency domain (Chapter 5). Figure 2-4 shows the measured dispersion of the waveguides. The dispersion at 1550 nm ranged from +28 to +35 fs^2/mm as the waveguide cross-section area decreases from 5×1.5 μm^2 to 2×1.5 μm^2. The increased dispersion for smaller cross-section waveguides may be attributed to the waveguide dispersion. The waveguide dispersion refers to the dispersion that originates from

43
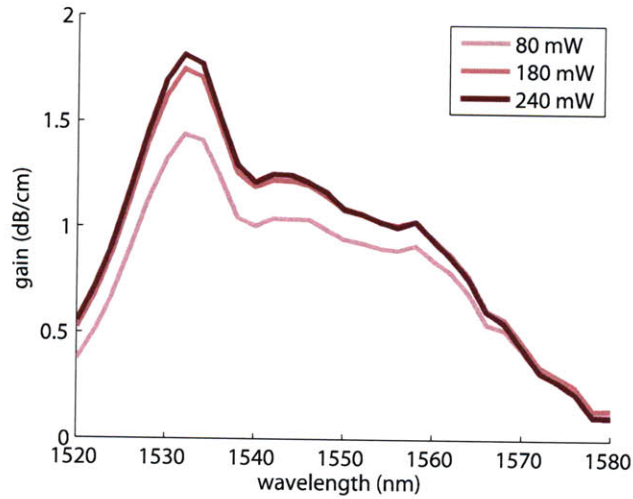
Figure 2-3: Single pass gain of the Er-waveguide per unit length. Measured by using 2-cm long waveguide with a cross-sectional dimension of 5.0 μm $\times$ 1.2 μm. Different colors correspond to different pump power levels from 80 mW to 240 mW. Coupled signal intensity was -21 dBm.
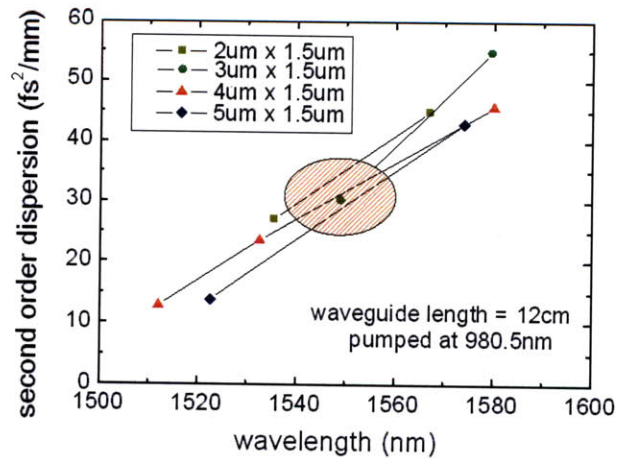
Figure 2-4: Measured dispersion for the Er-waveguides of different cross-sections.
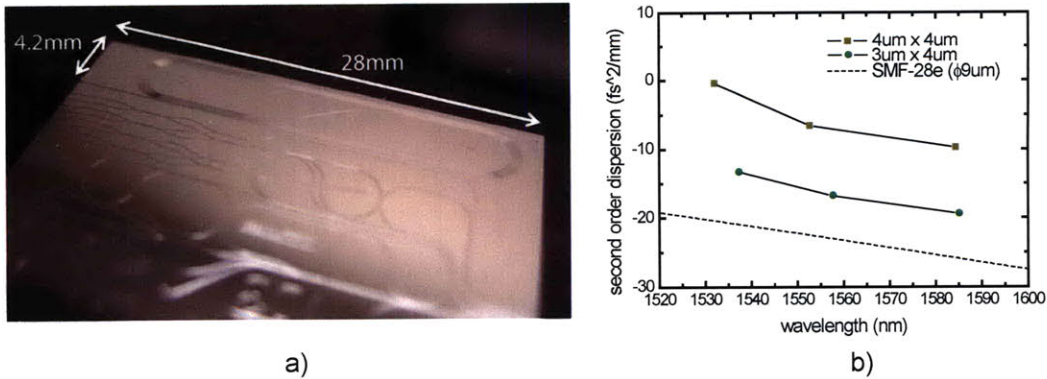
Figure 2-5: Ge-doped fused silica waveguide chip: (a) Picture with dimensions. The thin tracks in the upper part are the fused silica waveguides used for the dispersion measurement. (b) Measured dispersion for different wavelengths and cross-sections, compared to the dispersion of SMF-28.

frequency-dependent propagation constants[1].

2.1.2   Fused silica waveguide (passive section)

Passive waveguides are also important to engineer the cavity dispersion to enable soliton formation or femtosecond-pulse generation. CyOptics provided a sample chip containing 28-cm Ge-doped fused silica waveguides, which have cross-sectional dimension of 3 μm $\times$ 4 μm and 4 μm $\times$ 4 μm, shown in Figure 2-5(a). The dispersion of each waveguide is measured using a white-light interferometry and the measurement results are shown in Figure 2-5(b). For both waveguides with 3 μm and 4 μm width, anomalous dispersions were measured, -5 fs^2/mm and -15 fs^2/mm at 1550 nm respectively. The difference from SMF-28 is attributed to the waveguide dispersion that contributes larger normal dispersion with a smaller mode area. This result indicates that the combination of Er-doped waveguides and fused silica waveguides with a proper length ratio would enable the engineering of the total cavity dispersion and, eventually, soliton formation.

---

[1]The total dispersion of a single-mode waveguide is sum of material dispersion and waveguide dispersion.
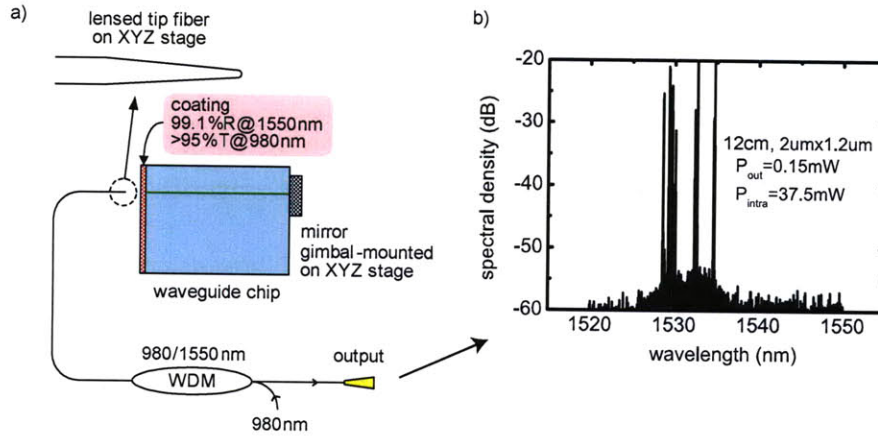
Figure 2-6: (a) Schematic of the experimental setup for a continuous wave (CW) Er-waveguide laser and (b) optical spectrum of the output.

2.2 Continuous wave operation

A continuous wave (CW) waveguide laser setup, shown in Figure 2-6, is built. In order to construct a laser cavity, one side of the waveguide chip is coated with high reflectivity at output wavelength (1550 nm) and high transmission at pump wavelength (980 nm). The other side of the waveguide chip was butt-coupled with a silver mirror mounted on a gimbal mount. The pump beam is coupled into one of the waveguides through a lensed-tip fiber mounted on a piezo-controlled XYZ stage (Thorlabs MAX302), while the output is coupled back into the same fiber and separated through a WDM. When the 12-cm long waveguide with a cross-section of 2 μm × 1.2 μm is pumped with a launched power level of 150 mW, an output power of 0.15 mW is obtained over the wavelength of 1530-1535 nm. The corresponding intracavity power of 37.5 mW should produce enough pulse energy to mode-lock the laser by a SBR.

2.3 Q-switched mode-locked operation

In order to form soliton pulses, the cavity nonlinearity should be balanced with net anomalous dispersion. Because the Er-doped waveguide is normally dispersive, we construct a extended-cavity waveguide laser by using an Er-doped waveguide chip,

46

an anomalously dispersive fiber, and a semiconductor SBR. The laser setup is expected to generate soliton pulses with calculated nonlinear phase shift and total cavity dispersion, but did not mode-lock. We suspect that (1) the long recovery time of the SBR and/or (2) the back-reflection at the waveguide-fiber interface prevent the soliton formation[2]. We verify the first hypothesis (SBR recovery time) by split step simulations.

2.3.1 Extended cavity experiment

Figure 2-7 shows the second version of the waveguide chip and the setup schematic for a mode-locked laser using the chip. The second version integrates output couplers and pump input ports, which bring the laser closer to a fully integrated mode-locked laser and allow a simpler experimental setup. The waveguide chip includes Er-doped waveguides with three different lengths: 1 cm, 5 cm and 10 cm. For each waveguide, the left side is open, while the right side has an integrated output coupler. The output coupler is based on a loop mirror structure with coupling ratio of 50%, which can be adjusted down to 5% or up to 95% as per necessity.[3] There is a 980-nm pump beam port from the right side. The pump and output ports at the right side are glued to a pair of fibers to simplify the experiment. The cross-sectional dimension of each waveguide is 4 μm $\times$ 1.2 μm for the inside and 5 μm $\times$ 1.25 μm near the edge of the chip. The cross-section is larger near the edge in order to align the waveguides to external fibers with a smaller loss. In order to build a soliton mode-locked laser using the above waveguide chip whose dispersion was measured positive in section 2.1.1, an additional section with negative dispersion is attached. In Figure 2-7(b), the waveguide chip is extended by adding a single mode fiber to achieve net negative dispersion for soliton formation. The left open end of the waveguide is aligned with a high-NA fiber (Thorlabs UHNA4) on a V-groove. The high-NA fiber is spliced[4] with a single mode fiber with the other end cleaved and butt-coupled to an SBR (R921),

---

[2]The waveguide index contrast is 10% and may require the polish angle to be larger than 8°

[3]The closer the coupling ratio approaches the extremes, the more the coupling ratio becomes wavelength-dependent.

[4]The splice loss between the UHNA4 fiber and SMF-28 fiber is estimated to be ~0.8 dB.
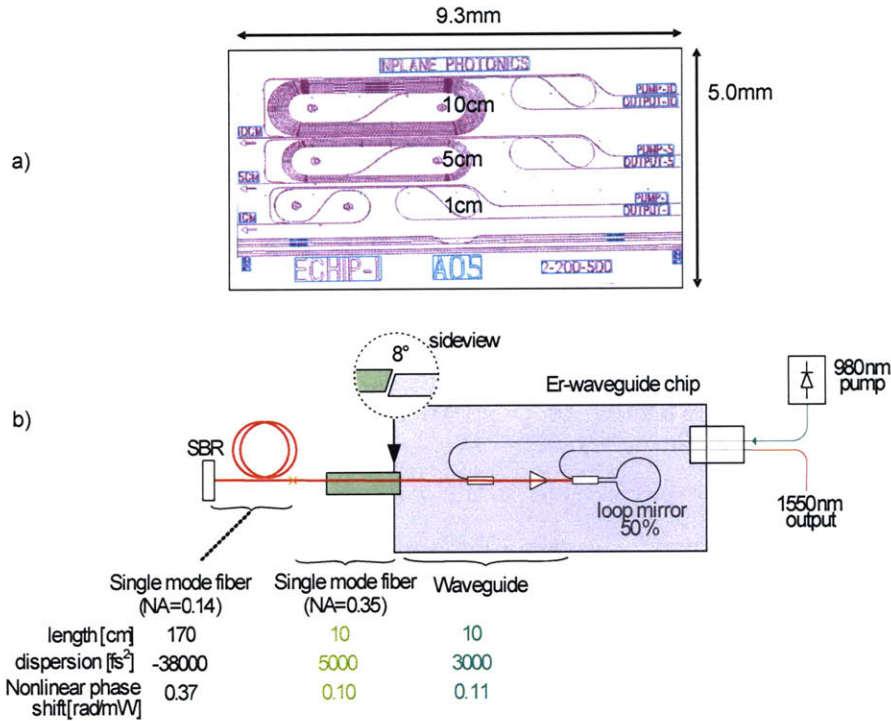
Figure 2-7: (a) Schematic of the waveguide chip and (b) schematic of the experiment setup for the Q-switched mode-locked waveguide laser. Below the schematic is the length, dispersion and nonlinear phase shift of each section in the waveguide laser. The laser setup in this figure shows the Q-switching instabilities.

which was grown in Prof. Kolodziejski's group at MIT using III-V semiconductor materials. Pump-probe measurements determine the saturable loss to reach up to 13.5% at 1540 nm, with a relatively slow recovery time of 43 ps [4, 41]. The interface between the high-NA fiber and the waveguide chip is 8-degree polished to reduce back reflections.

With a target pulse width of τ=225 fs and a target total nonlinear phase shift of Φ=0.6 rad, necessary negative dispersion is $|D| = \Phi\tau^2 = 30000$ fs^2. Figure 2-7(b) shows how we obtain the necessary negative dispersion. A 10-cm Er-doped waveguide has measured positive dispersion of 3000 fs^2 and a 10-cm high-NA fiber has 5000 fs^2 from its datasheet. 170-cm SMF-28 fiber is spliced to the high-NA fiber in order to achieve net negative dispersion of 30000 fs^2. The total cavity length corresponds to a repetition rate of 53 MHz. At the same time, we verify that the available intracavity power provides an appropriate level of nonlinear phase shift and fluence on the SBR.

symbol	value	unit	description
Φ	0.7	rad	Nonlinear phase shift per round trip at E_p=30 pJ
D_2	-30000	fs^2	Cavity dispersion
E_p	$0\sim 43$	pJ	Pulse energy
τ_A	0.43, 4.3, 43	ps	SBR recovery time

Table 2.2: Parameters for the soliton mode-locking simulation of an extended-cavity waveguide laser.

However, the extended cavity waveguide laser fails in forming soliton.

2.3.2 SBR recovery time

The relatively slow recovery time (43 ps) of the saturable absorber used in the experiments in Section 2.3.1 is suspected to prevent soliton mode-locking. The recovery time of a saturable absorber refers to how fast the absorber can return to its initial condition after being bleached by a pulse. A slower recovery time of a SBR facilitates the growth of noise on the tail of pulses. Once the noise in the tail grows enough, multiple pulses travel inside the cavity and the soliton cannot be sustained stably [28].

Laser cavities with different absorber recovery times are simulated using the split step method. More details on the simulation method can be found in Agrawal [42] and Birge [43].

Table 2.2 describes the key parameters used to simulate the waveguide laser in soliton mode-locking regime. Negative dispersion is assumed for soliton mode-locking and the gain relaxation time is neglected to simulate a Q-switching-free laser. Q-switching happens in the timescale of μs-ms, so simulating femtosecond pulse shaping together with Q-switching will take impractically long time for wide-spread personal computers. It is assumed that single pulse formation can suppress Q-switching instabilities, while multiple pulses cannot.

Figure 2-8 presents the simulation result for the absorber recovery time τ_A of 0.43 ps and 4.3 ps. For τ_A=0.43 ps, the single pulse mode-locking is maintained over the entire range of pulse energy with a pulse width approaching to a theoretical limit of

49
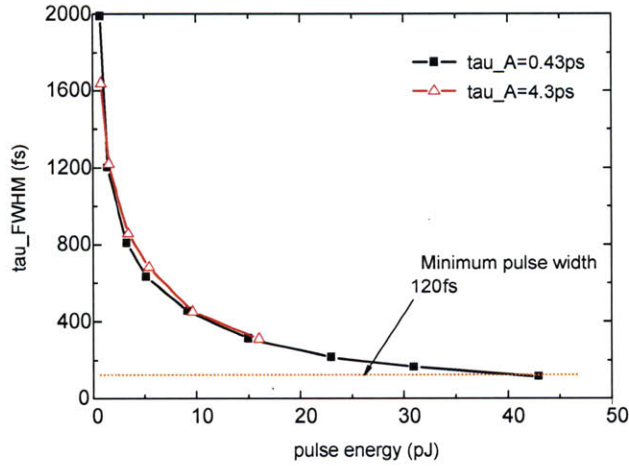
Figure 2-8: Simulated pulse width versus pulse energy of the 920 MHz waveguide laser for two different absorber recovery times – 0.43 ps (black) and 4.3 ps (red). A data point in squares or triangles denotes that there exists a steady-state single pulse mode-locking solution. There is no corresponding data point for 43-ps case.

120 fs [28]. On the other hand, multiple pulse break-up begins at a pulse energy of 15 pJ for τ_A=4.3 ps. With an even larger τ_A, the laser always experiences multiple pulse break-up. Figure 2-9 shows the case of τ_A=43 ps, where the pulse break-up occurs in both time and frequency domain.

The simulation results suggest that the recovery time of SBR critically affects the mode-locking stability and the SBR needs to be engineered for a proper recovery time, preferably less than a few picoseconds.

2.4 Mode-locked operation

A waveguide chip is fabricated by using both Er-doped waveguide for gain medium and phosphor-doped (P-doped) fused-silica waveguide for dispersion engineering. The P-doped waveguide is attached to the Er-doped waveguide despite a considerably lower repetition rate, because it is the most reliable technology for dispersion engineering, given that anomalously dispersive gain waveguide is not available.

The laser cavity consists of a 5-cm section of Er-doped waveguide with a group-velocity dispersion of 30 fs^2/mm. A 20-cm section of phosphor-doped silica waveguide

50
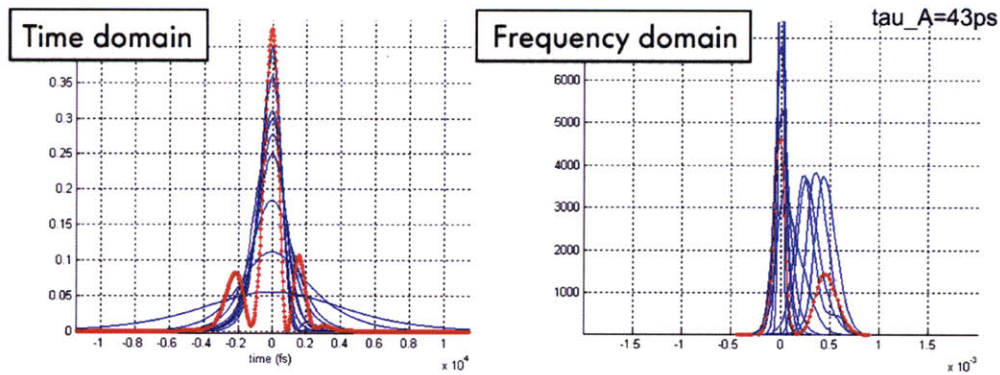
Figure 2-9: Evolution of pulses in the 920 MHz waveguide laser for a SBR recovery time of 43 ps and pulse energy of 10 pJ. For the entire range of pulse energy, there are no stable soliton pulses. Red lines trace the pulse envelope in time (left) and frequency domain (right) after 6000 round trips, while blue lines show the pulse envelopes every 600 round trips.
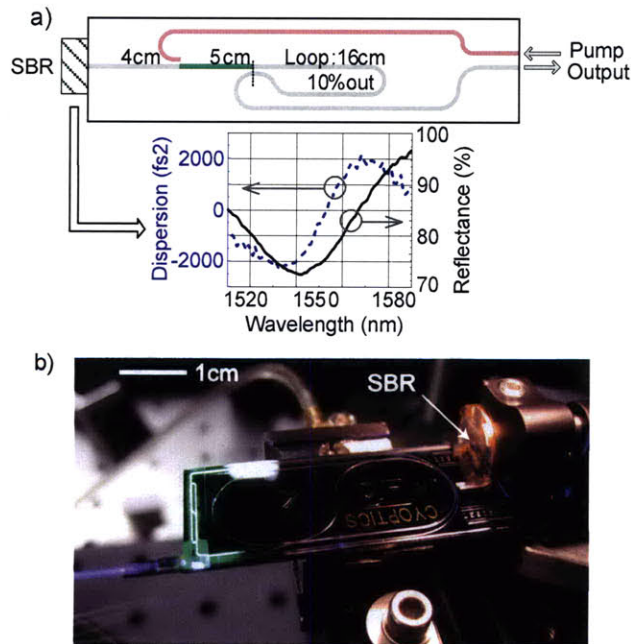
Figure 2-10: Waveguide soliton laser setup: (a) schematic with the characteristic of SBR and (b) picture of the setup. In the schematic, the gray line indicates the fused silica section, green line the Er-doped section and red line the pump input.

with a dispersion of -25 fs^2/mm [5] is used to obtain a net anomalous intracavity dispersion to enable soliton mode-locking. The length of the Er-doped section is determined to generate the necessary intracavity power, while the length of silica waveguide is determined in order to achieve appropriate dispersion for soliton operation. Decreasing the average dispersion shortens the pulse width, but too little dispersion can lead to instability due to the insufficient suppression of the continuum. The Er-doped section and the P-doped silica-glass section have an effective mode area of 10 μm^2 and 40 μm^2 respectively. A loop mirror is used at one end to provide 10% output coupling, while the other end is butt-coupled to an external SBR. The SBR is a commercial unit with 14% modulation depth, a 2 ps recovery time and a saturation fluence of 25 μJ/cm^2. Pump power is provided by an external 976 nm laser diode coupled to the waveguide chip. The laser is operated with 400 mW of cavity-coupled pump power; the intracavity signal power is measured to be 12 mW, corresponding to a 30-pJ intracavity pulse energy. The output pulses with an average power of 1.2 mW are then amplified to 18 mW using an EDFA, detected using a photodiode, and measured with a sampling scope and a signal source analyzer.

The fabrication of Er-doped films of aluminosilicate glass is done by radio frequency (RF) sputtering on oxidized Si substrates. Waveguide cores are defined using conventional lithography and etching; and finally a silica upper cladding was deposited [14]. A similar process using P-doped glass is applied to fabricate the passive waveguide section. The Er-doped section and the P-doped silica-glass section are connected through a mode convertor with loss less than 0.15 dB. The P-doped section is tapered to be wider near the chip edge to minimize the coupling loss to single mode fiber.

Figure 2-11 depicts the measurement results. The 5-second persistence trace shows excellent signal stability, while the RF spectrum in (c) indicates a side-mode suppression ratio of 80 dB. The 8.4-nm full width half maximum (FWHM) optical bandwidth before amplification implies 300-fs-duration transform-limited pulses. After amplifi-

---

[5]This P-doped silica waveguide has larger effective mode area than that in Figure 2-5 and correspondingly larger negative dispersion, which is close to that of SMF-28.
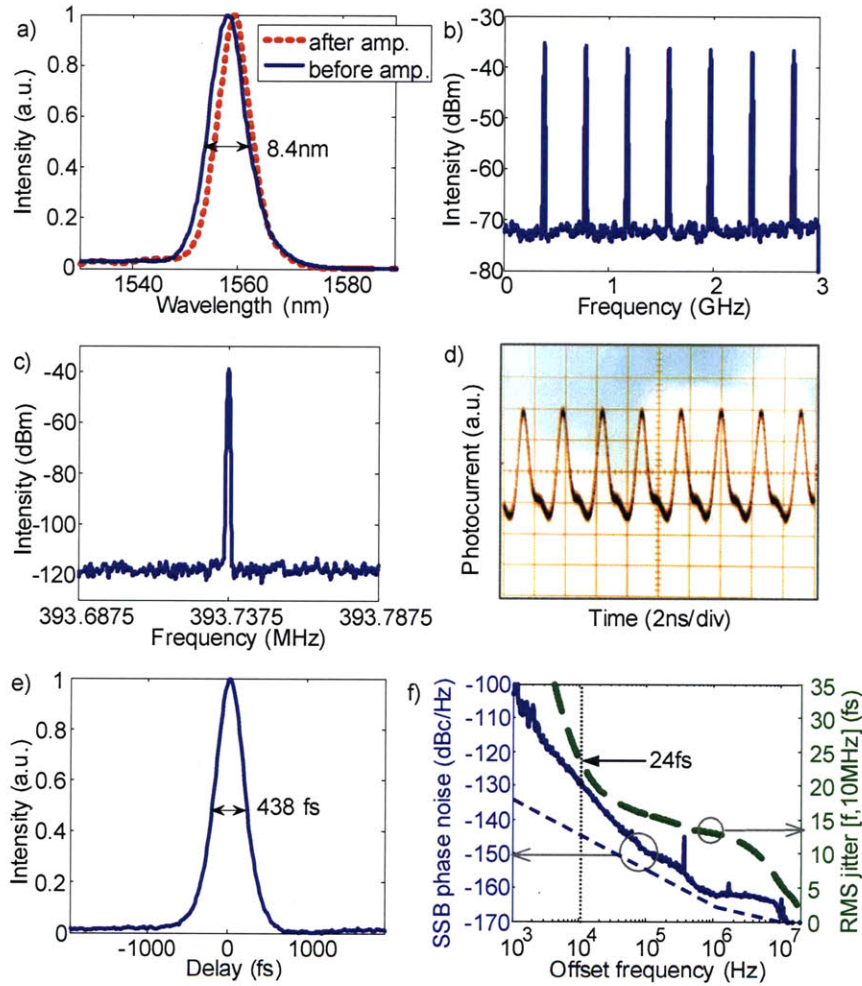
Figure 2-11: Er-waveguide laser - measurement traces at 394 MHz: (a) normalized optical spectrum before and after amplification (dashed), (b) RF spectrum (3 GHz span, 10 MHz resolution), (c) RF spectrum (100 kHz span, 500 Hz resolution), (d) 10 second persistence trace, (e) background free autocorrelation trace and f) single side band (SSB) phase noise of the first harmonic of the laser with instrument noise limit (short-dashed) and integrated root-mean-square (RMS) timing jitter (long-dashed).

	Er-doped section	P-doped section
A_{eff} (μm^2)	10	40
β_2 (fs^2/mm)	+30	-25
n_2 (m^2/W)	2.5×10^{-20}	
$\beta_{2,SBR}$ (fs^2)	+1000	

Table 2.3: Laser parameters for split-step Fourier simulation.

Repetition rate (MHz)	394	
Intracavity pulse energy (pJ)	30	
Pulse width (fs)	Measured	Simulated
	300*	310
Optical spectrum FWHM (nm)	Measured	Simulated
	8.4	8.6

Table 2.4: Experimental and simulated results. (* a transform-limited pulse width calculated from the measured optical spectrum FWHM)

cation, the optical bandwidth decreases to 7.4 nm, corresponding to 340 fs. The autocorrelation measurement yielded a pulse duration of 440 fs. The difference is attributed to incomplete compensation of the chirp added by the Er-doped fiber. The laser is self-starting and, as the pump power is increased, the laser first operates in a mode-locked Q-switching state before transitioning to a continuous-wave soliton mode-locked state at a pump power of 160 mW. Pump powers much higher than 400 mW resulted in pulse breakup as the intracavity energy was too high to sustain a single soliton for the given round-trip dispersion. Figure 2-11(f) shows the phase noise of the first harmonic (394 MHz) of the laser. The timing jitter integrated from 20 MHz progressively down to 1 kHz is also shown. The timing jitter integrated from 10 kHz to 20 MHz is 24 fs, which is close to the noise sensitivity limit of the Agilent E5052 signal analyzer. We expect that the timing jitter can be further reduced to a few- or even sub-femtosecond range with a different measurement method using optical cross correlators [44].

The experimentally observed pulse characteristics can be compared with theoretical predictions based on the split-step Fourier method, using our waveguide and SBR parameters. The second order dispersion, the Kerr effect and gain filtering with parabolic gain shape are considered in the simulation. The SBR is modeled using

the rate equation for a slow saturable absorber [45]. Table 2.3 summarizes the values used in the simulation, while Table 2.4 compares the predicted and experimental laser characteristics. Good agreement, within 3%, between the experimental and predicted spectral characteristics is obtained. In order to remove the effect of uncompensated chirped, the comparison is based on the transform-limited pulse width both for the simulated and measured results. Some discrepancy may be attributed to the non-uniform dispersion profile of the SBR, as its dispersion can change as much as 1000 fs^2 within the optical bandwidth of the laser output (inset of figure 2-10).

2.5 Summary

Starting from the characteristic of available planar waveguides, a flow of building a femtosecond waveguide laser was discussed. The CW-mode operation of the Er-doped waveguide chip demonstrated that enough pulse energy can be generated for mode-locking. However, the Er-doped waveguide laser did not form solitons due to the long recovery time of the SBR although the normally dispersive Er-waveguide was extended with a single mode fiber (SMF) for an anomalous dispersive cavity. Thus, the SBR was replaced with another one with a faster recovery time, and, instead of an external SMF, the phosphor-doped silica waveguide was integrated with the Er-doped waveguide to turn the total cavity dispersion into negative. Consequently, the waveguide laser could produce femtosecond soliton pulses.

Chapter 3

Higher-repetition-rate waveguide lasers

Higher pulse repetition rates, such as a few GHz to tens of GHz, can benefit a broader range of applications. For photonic ADC applications, the necessary number of channels can be reduced by higher sampling frequencies. For example, an ADC system with 40 GSPS (giga samples per second) requires 80 channels of 0.5-GSPS ADC, while 20 channels of 2-GSPS ADC would alleviate the strict bandwidth specification of the filter banks.

Optical frequency reference for astro-comb is another application that prefers higher repetition rates [46]. In order to use optical combs as frequency reference, one frequency component needs to be separated from the others and sparse combs are easier to separate in terms of the required sharpness of the optical filter response. Usually, at least, a 10-GHz separation (or repetition rate) is required.

The approaches to increasing the repetition rate of a laser are generally categorized into three; 1) making the cavity smaller, 2) generating more than one pulse inside the cavity (also known as harmonically mode-locked lasers), and 3) multiplying the repetition rate externally. Details about these approaches are well explained in Sickler [47]. The first approach of shrinking the cavity dimension may be the most elegant way, but it is quite challenging due to the limited available technologies, such as available pump power and maximum gain per unit length. The third option of ex-

ternal multiplication requires extra setup and space, but it can usually provide higher repetition rates than the cavity-shrinking can do. In this chapter, the first and the third approaches are discussed.

3.1 Reduced cavity: 1.5-2 GHz waveguide lasers

This section discusses the approach of scaling down the cavity length for higher repetition rates and keeping the laser fundamentally mode-locked. A fundamentally mode-locked laser provides an attractive design for a low-jitter femtosecond laser source because of its simplicity and low cost. Additionally, the fundamentally mode-locked laser can avoid losses that are induced during the multiplication of the repetition rate, thus enabling a higher efficiency.

3.1.1 Design

Waveguide lasers were mode-locked in section 2.4 by using a 5-cm Er-doped waveguide attached to a 20-cm P-doped silica waveguide for dispersion compensation. When we scale down the cavity length, the gain waveguide cannot become shorter to ensure high enough intracavity power; removing the P-doped silica waveguide allows to increase the repetition rate by a factor of five, which is about 2 GHz. Instead, the corresponding dispersion should be added externally. Among many ways of engineering the dispersion, thin-film coatings will be used since they are the only solution that do not increase cavity length significantly.

Figure 3-1(a) sketches the GHz-repetition-rate waveguide laser that consists of an Er-doped waveguide chip butt-coupled to a SBR and an output coupler on each end. The output coupler uses a GTI (Gires-Tournois Interferometer) structure to add anomalous dispersion at the lasing wavelength. The reflectivity and dispersion of an exemplary output coupler coating are shown in Figure 3-1(b). The coating is composed of about 6-μm TiO_2 layer on a 6-pair SiO_2/TiO_2 high-reflectivity mirror. Anomalous dispersion of -3000 fs^2 – -4000 fs^2 is obtained over about 15 nm near 1560 nm, which will be roughly the lasing wavelength.
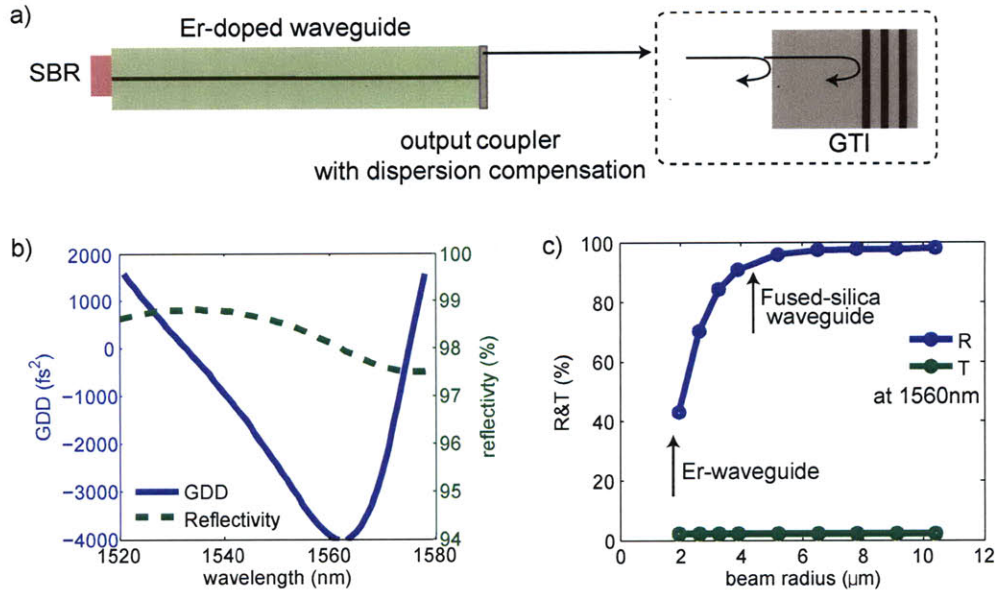
Figure 3-1: (a) A schematic of the GHz-repetition-rate waveguide laser with dispersion-compensation coatings made of a GTI-like structure, (b) Reflectivity and group delay dispersion of the example GTI, and (c) Reflectivity and transmission of the GTI as a function of incident beam radius. GTI: Gires-Tournois Interferometer.

One practical problem not mentioned so far is the beam divergence over the output coupler coating. The Er-doped waveguide provides 10% index contrast and the height needs to be as small as 1.2 – 1.5 μm. The beam out of the Er-doped waveguide is not guided through the coating and diverged substantially. Figure 3-1(c) shows the simulated reflectivity and transmission of the output coupler coating along the beam radius that exits the waveguide. The simulation considers Gaussian beam propagation inside the coating structure. For the Er-waveguide case, the reflectivity drops from 98% to only 40% due to the beam divergence. Thus, a short taper-out that enlarges the output beam radius is required. The P-doped fused silica waveguide will provide 92% reflection, according to the simulation. Therefore, minimum length of fused silica waveguide is attached on both ends of the Er-doped waveguide.

The final design layout is shown in Figure 3-2 with a photograph of an actual sample. Each waveguide chip contains Er-doped waveguides with four different lengths of 35, 40, 45 and 50 mm. The Er-waveguides are tapered out by using P-doped fused silica waveguides with a length of 5.5 mm on both ends. The two different waveguides

* Grid: 1mm

22 x 6 mm²

Fused silica

Mode convertor
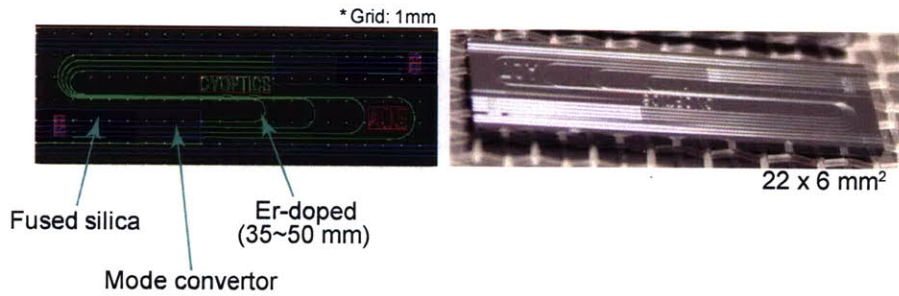
Er-doped
(35~50 mm)

Figure 3-2: The layout and a photograph of the short Er-doped waveguide chip. Chip layout courtesy of CyOptics.

are smoothly connected by using mode-convertors.

3.1.2 Characterization

CW-mode operation

The waveguide chip is first characterized for CW-mode operation to check if enough intracavity power can be generated. Figure 3-3(a) describes the experimental setup for the CW-mode operation. The waveguide chip is butt-coupled to a silver mirror on its right side and to a partial reflector (PR1-1550-90-0525, CVI lasers) on its left side. The 980-nm pump beam is focused by using an aspheric lens (C220TME-C, Thorlabs) and the output is separated by a dichroic beam splitter (DBS). The measured output power as a function of the pump diode current is shown in Figure 3-3(b) for two different output couplers (OCs). The 1.40%-OC provides up to 70-mW intracavity power, which is about 30% more than the 6.50%-OC does. Considering about 30 mW of intracavity power is required for mode-locking at 2-GHz repetition rate, this intracavity power would suffice the requirement even with a SBR that is usually more lossy than a silver mirror.

The saturation of the output power at higher pump currents can originate from (1) the gain saturation (or bleaching) and/or (2) the alignment degradation due to the thermal expansion of the chip. From a separate experiment, about 35% of pump is absorbed over a single pass through a 5-cm Er-waveguide. The residual pump is reflected by the silver mirror and absorbed again by the same ratio, resulting in about
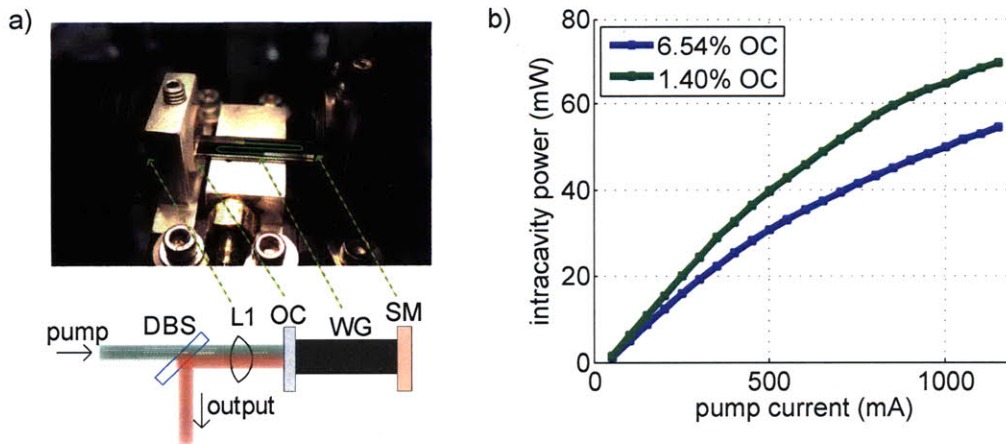
Figure 3-3: (a) A photo and schematic to evaluate the CW-mode operation of the Er-doped waveguide laser, and (b) output power versus pump current. DBS: dichroic beam splitter, L1: aspheric lens, OC: output coupler, WG: waveguide chip, SM: silver mirror.

55% pump absorption over the round trip. Thus, for a pump current of 1100 mA, 350 mW of pump is launched into the waveguide and 192 mW of pump is absorbed, most of which is converted to heat. Although more investigation is needed to examine how much the absorbed pump affects the alignment, a temporal change of the output power for various pump power levels, shown in Figure 3-4, supports the degradation of the alignment due to the pump absorption and consequent thermal expansion of the chip.

Figure 3-4 compares the 10-minute log of the output power for pump currents from 100 mA to 1100 mA with an incremental step of 100 mA. While the output power with 100 – 200 mA pump current remains at the same level, a higher level of pump current drops the output power over time. For example, a 1100-mA pump current induces 0.2-mW drop of the output power for the first 10 minutes. However, after longer time passes and the thermal expansion of the chip is settled down, the output power converges to a constant level. These pump-power-dependent changes of the output power supports the misalignment of the setup due to the thermal expansion from the absorbed pump power. In order to avoid the misalignment, a more robust butt-coupling mechanism is required that tolerates slight thermal expansion.
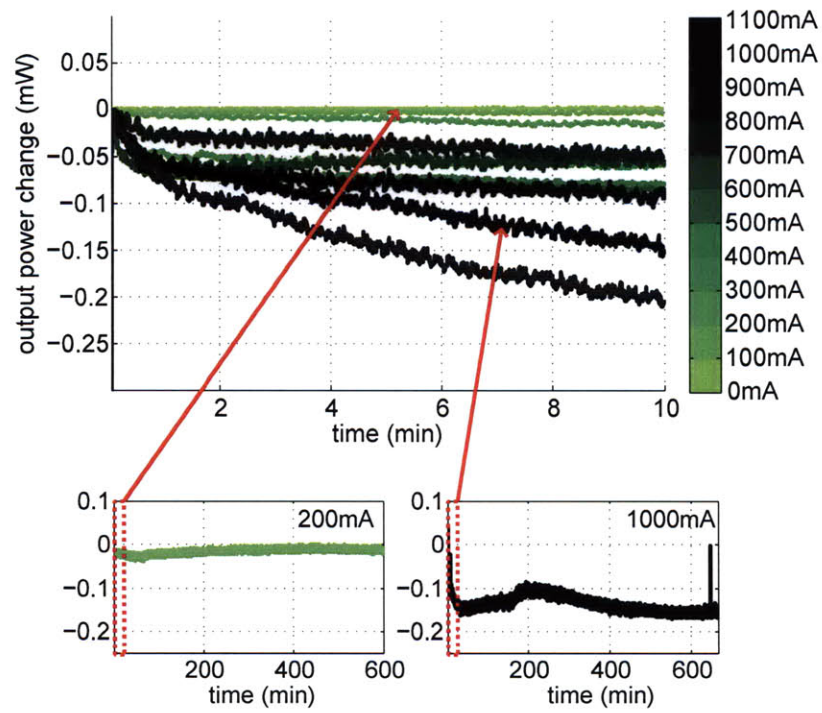
Figure 3-4: Output power change for various pump diode currents. The butt-coupling condition is considered being affected by thermal expansion of the waveguide chip caused by pump absorption.
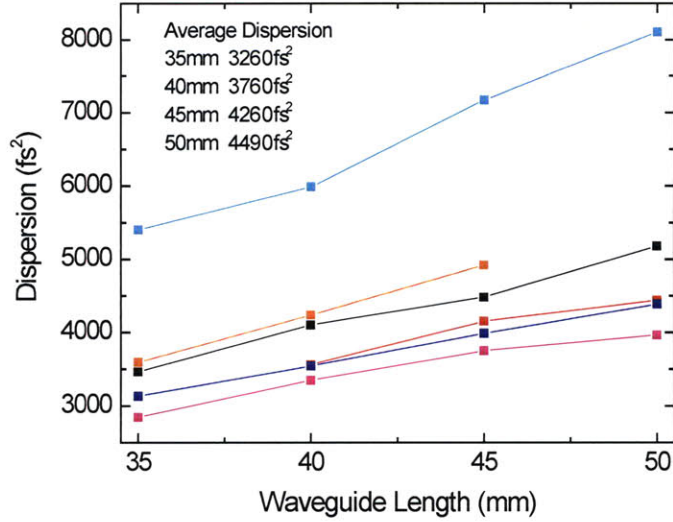
Figure 3-5: Measured second-order dispersion of selected waveguide chips at 1560 nm. Plot courtesy of Michelle Sander.

Dispersion

The anomalous cavity dispersion is an important condition to enable soliton formation. The dispersion of various waveguides is measured to verify if the normal dispersion of the Er-doped waveguides can be compensated by output coupler coatings with reasonably small thickness. In order to compensate larger dispersion, the coating should become thicker and the effect of beam divergence can significantly reduce the reflectivity of the coating. The dispersion is measured by using the setup and procedure in Section 5.1.

A total of 145 waveguides are examined for the dispersion, and the measured dispersion for 23 waveguides that show the lowest waveguide losses is shown in Figure 3-5. The second-order dispersion of 50-mm waveguides averages 4500 fs^2, while the 35-mm waveguides measures 3300 fs^2 on average. The difference reveals that the Er-doped waveguide contributes a dispersion of $+40$ fs^2/mm. The measured dispersion is about two times larger than we predicted from previous measurements in Chapter 2. The large normal dispersion makes it difficult to compensate with external coatings with reasonably small beam divergence. The larger normal dispersion may be attributed to the thin Er-layer, which was targeted for 1.2 μm. Thus, we conclude

63
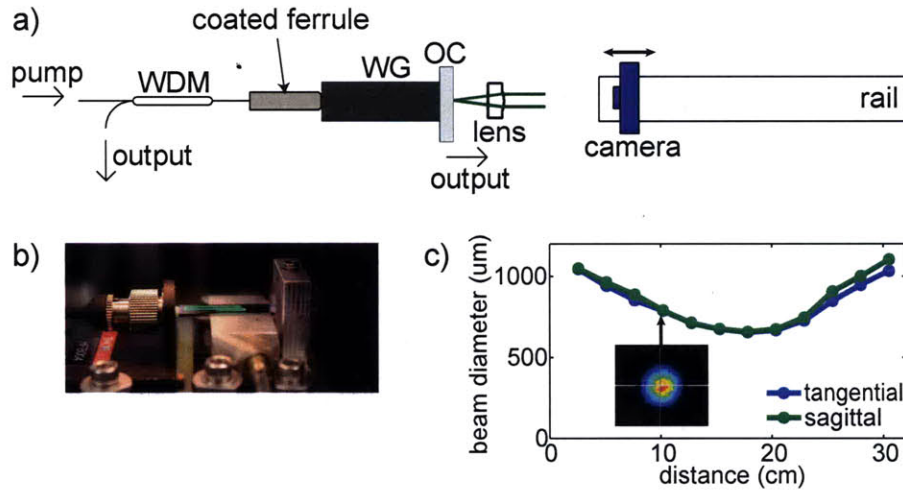
Figure 3-6: Experimental verification of single mode operation. (a) Setup schematic, (b) a photograph of the experimental setup, and (c) beam profile after the collimating lens.

that the same design is re-fabricated with a thicker Er-waveguide of 1.5-μm height.

3.1.3   Re-fabricated waveguide chip

Verification of single-mode operation

The same design as in Figure 3-2 is re-fabricated with thicker Er-doped waveguides; the target height increases from 1.2 μm to 1.5 μm. Both heights actually allow the waveguide to support multimode at a wavelength of 1550 nm with a 4-μm width. The multimode signal is suppressed through the bent waveguide section such that only a single transverse mode is supported for lasing. The multimode suppression decreases from 80% to 60% for the increased Er-waveguide height from 1.2 μm to 1.5 μm. Although we expect that even 60% loss of multimode wave is enough to eliminate the higher-order modes from lasing, a single mode operation is verified by using an experimental setup for the CW-mode operation with the re-fabricated waveguide chip, shown in Figure 3-6.

In the experimental setup in Figure 3-6(a), the waveguide chip is butt-coupled to a fiber ferrule coated with a 90% partial reflector (custom coating run, OzOptics) and a flat output coupler with 90% reflectivity. The coated ferrule and the output coupler

transmit 980-nm pump ~90% and ~80% respectively. The 980-nm pump beam is injected through the fiber and the output is separated by a WDM. The fiber-coupled output from the WDM is used to monitor the alignment of the waveguide chip and the free-space beam from the output coupler is used to examine the beam profile. The collimating lens (C220TME-C, Thorlabs) near the output coupler is aligned such that the beam forms a waist near the middle of the rail. An IR-camera (WinCamD-IR, DaraRay) is translated along a 50-cm rail to capture the beam profile. A photograph of the experimental setup around the waveguide chip is shown in Figure 3-6(b).

The single-mode operation of the waveguide laser is confirmed by measuring the beam profile after the collimating lens. Assume that a beam has a waist of w_0. Then the half-angle beam divergence at wavelength λ is given by

$$\theta = M^2 \frac{\lambda}{\pi w_0}, \tag{3.1}$$

where M^2 is called beam qualify factor or beam propagation factor. $M^2=1$ implies that the beam is diffraction-limited or single-mode. The captured beam profile along the propagation direction is plotted in Figure 3-6(c). θ and w_0 can be extracted from the beam profile. Using Equation 3.1, M^2 values are estimated to be 1.1 for both tangential (horizontal) and sagittal (vertical) axes. Thus, we conclude that only single-mode is supported in the waveguide laser.

Measured dispersion

The dispersion of the re-fabricated waveguides is measured to verify the reduced normal dispersion. Approximately 100 waveguide chips were delivered and the dispersion of 11 waveguide chips were examined over different positions on a wafer. The measured dispersion is shown in Figure 3-7 with horizontal axis of the Er-waveguide length and vertical axis of the second-order dispersion, in separate plots for two wafers.

When compared to the dispersion in Figure 3-5, the average dispersion decreased by ~3000 fs^2 for the 50-mm long Er-waveguide, which proves the increased thickness of the Er-doped layer. The Er-layer thickness varies over the entire wafer by a few %
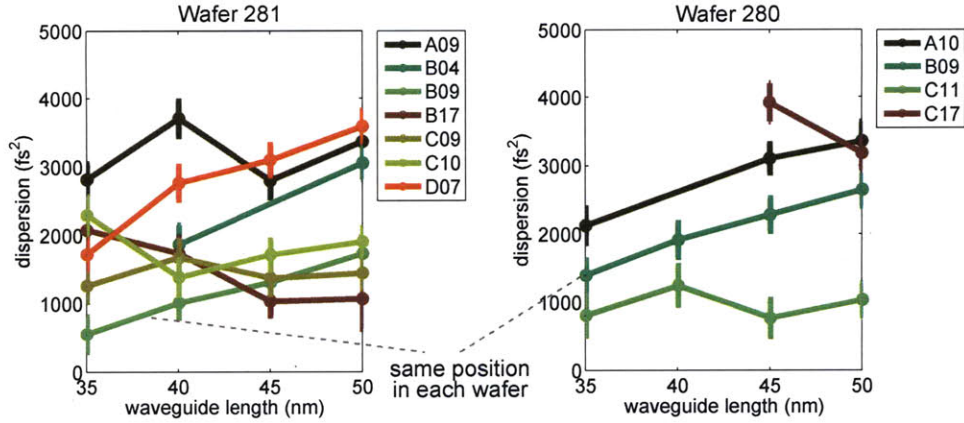
Figure 3-7: Measured dispersion of the re-fabricated waveguides from two wafers. Each wafer contains slightly different thickness of Er-doped waveguides and each chip inside one wafer also does. By comparison of B09 sample, the average thickness of Er-doped layer is considered to be larger in the wafer 281.

with a cylindrical symmetry. As a result, each waveguide chip shows different trend of dispersion along the waveguide length since the Er-layer thickness can vary even in one chip. The wafer 281 is known to have a thicker Er-layer from the fabricator, which is supported by the measurement results. When we compare the dispersion of B09 sample, both wafers give similar linear trend over the Er-waveguide length with different slopes, but the dispersion of B09 in wafer 281 is smaller than that in wafer 280 by about 1000 fs^2. That is the reason why more samples were investigated in wafer 281, looking for waveguides with a smaller normal dispersion.

The average dispersion for 50-mm long Er-waveguides is measured 1500 fs^2 as expected originally and enabled the design of output coupler coating with necessary anomalous dispersion.

Simulation on the soliton formation

Laser cavities that use 50-mm long Er-waveguides are simulated using the split-step Fourier method. The second order dispersion, the Kerr effect and gain filtering with parabolic gain shape are considered in the simulation. The SBR is modeled by using the rate equation for a slow saturable absorber [45]. Table 3.1 summarizes the parameters used to simulate the waveguide laser including a 50-mm long Er-waveguide.

66

	variable	value
Cavity (P-doped)	length	11.5 mm
	A_{eff}	55 μm^2
	β_2	-24 fs^2/mm
	n_2	2.8 $\times$ 10^{-16} cm^2/W
Cavity (Er-doped)	length	50.0 mm
	A_{eff}	10 μm^2
	β_2	+21 fs^2/mm
	n_2	2.8$\times$10^{-16} cm^2/W
SBR	saturation fluence	7 μJ/cm^2
	modulation depth	6 %
	recovery time	3 ps
	dispersion	-1000 fs^2
Output coupler	coupling ratio	2.5 %
	dispersion	-1500$\sim$-3000 fs^2
Operation (typical)	wavelength	1.56 μm
	repetition rate	1.56 GHz
	intracavity power	15.0 mW
	pulse width	450 fs
	soliton phase shift	13 mrad

Table 3.1: Parameters for the simulation of a 1.56-GHz waveguide laser.

The dispersion of Er-doped waveguide is calculated from the known dispersion of P-doped waveguide and the measured total dispersion. The parameters for the SBR are based on the measurement of an in-house SBR. The operation parameters contain one typical set within some range, shown in Figure 3-8.

The simulation results are plotted in Figure 3-8 with horizontal axis of intracavity power and vertical axis of pulse width. Four different values of the cavity dispersion are examined, from -1000 fs^2 to -2500 fs^2. Pulse width versus intracavity power is plotted for each cavity dispersion. The operation region is limited by the following boundaries.

1. Intracavity power

    The pulse width of a soliton is inversely proportional to the pulse energy or the intracavity power, given that other parameters remain the same. The intracavity power is limited by the available pump power and the intrinsic cavity loss. From a separate experiment that uses a similar setup as in Figure 3-6, we veri-
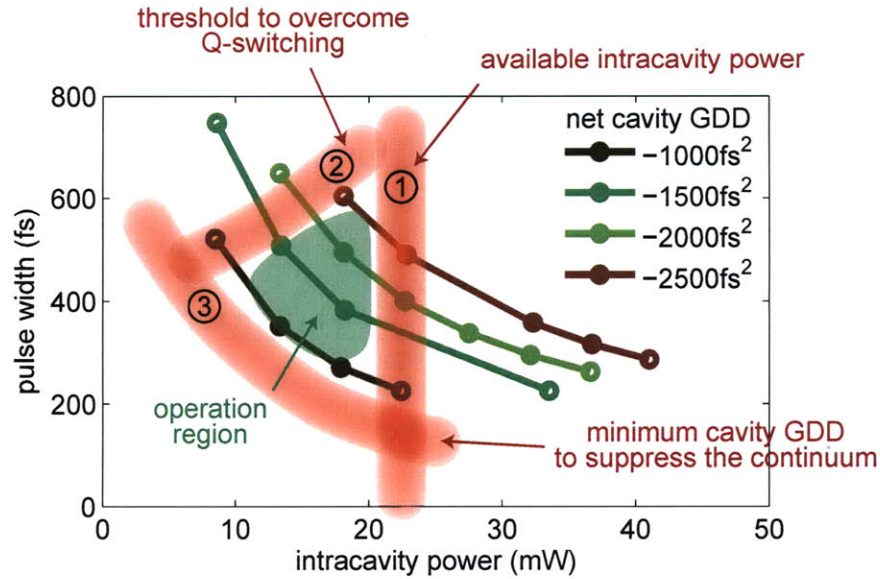
Figure 3-8: Soliton pulse width versus intracavity power for various cavity dispersions. Three boundaries are indicated that limit the operation range. The maximum dispersion boundary is not shown since it does not usually occur for the high-repetition-rate or short-cavity lasers.

fied that an intracavity power of 20~25 mW can be generated with 10% output couplings at both ends, which emulates a similar cavity loss of the mode-locking that uses a SBR.

2. Q-switching threshold

Soliton formation counteracts the Q-switching by reducing the cavity gain against the pulse energy increase by perturbation. The soliton pulse energy should be larger than a minimum to effectively suppress the Q-switching instability. The minimum pulse energy for stable soliton formation can be calculated as derived in Hönninger et al. [48] and depends on the cavity dispersion, among various parameters. With larger cavity dispersion, the soliton forms a broader pulse width and a smaller nonlinear phase shift, which leads to a weaker effect to suppress the Q-switching. Thus, larger cavity dispersion increases the threshold pulse energy. A few points outside the threshold boundary are also plotted because the simulation model assumes that the upper-state lifetime of the gain is zero and consequently, the modeled laser is always free of the Q-switching

instability.

3. Minimum dispersion

Minimum dispersion is required to suppress the continuum. Too small dispersion cannot suppress the continuum that may prevent the formation of stable solitons. The simulation shows that the cavity dispersion of -1000 fs^2 allows solitons, while -500 fs^2 does not. The minimum dispersion is affected by the recovery time of the SBR. The slower the SBR recovers, the larger dispersion is required to suppress the continuum since the noise on the pulse tail is more likely to survive. For example, a recovery time of 9 ps increases the minimum dispersion up to -2500 fs^2.

4. Maximum dispersion or nonlinearity (Not shown in Figure 3-8)

The maximum dispersion can be limited by the nonlinear phase shift, which is desired to be less than $\sim$1 radian. However, the maximum dispersion boundary is not addressed in Figure 3-8 since it does not usually occur for the high-repetition-rate or short-cavity lasers.

5. Multiple pulsing (Not shown in Figure 3-8)

Multiple pulse breakup sets the upper limit on the pulse energy that supports the single pulse operation, but is not drawn in Figure 3-8 because the pulse energy is already limited by the available intracavity power. The threshold pulse energy of multiple pulse breakup is a function of many variables of the SBR, such as the recovery time, or the two photon absorption. With a longer recovery time, the tail of net gain window becomes broader and allows an easier growth of the noise over the tail. The larger the two photon absorption is, the smaller pulse energy can lead to the multiple pulse breakup [49].

Output coupler coating

The simulation results in Figure 3-8 indicate that a dispersion of -1500 fs^2 is a reasonable target for the total cavity dispersion at 1560 nm. Assuming that the waveguide

69
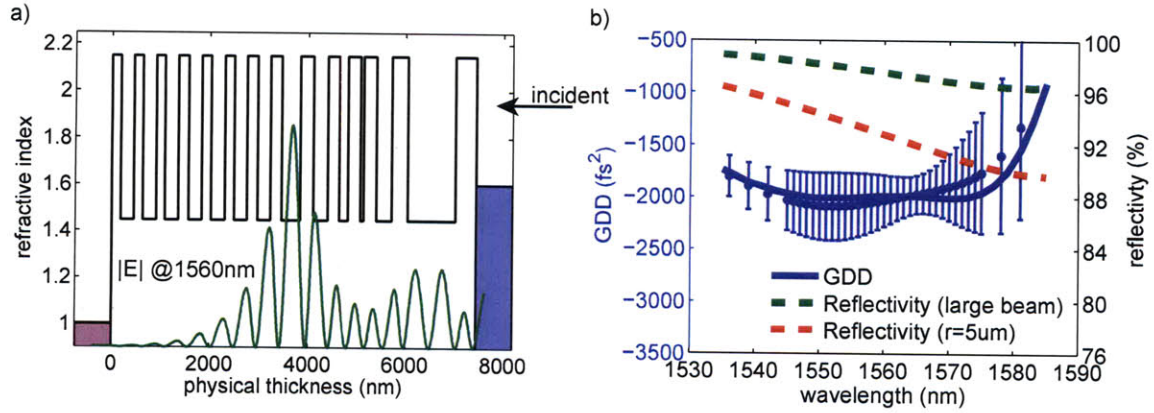
Figure 3-9: An example of output coupler coatings with anomalous dispersion. (a) Index profile with electric field overlaid at 1560 nm and (b) reflectivity and group delay dispersion (GDD) with a fabrication error of RMS 0.5%. The reflectivity is compared for a large beam and a smaller beam with a radius of 5 μm.

dispersion is +1500 fs^2 and the SBR dispersion is -1000 fs^2 at 1560 nm, the output coupler needs a dispersion of -2000 fs^2 at 1560 nm.

The output coupler coating is designed by using a commercial software, OptiLayer. SiO$_2$ and Nb$_2$O$_5$ are chosen as the dielectric materials because their thickness can be quite accurately controlled at Advanced Thin Films, Inc. with a RMS thickness error less than 0.5% [50] in ion beam sputtering (IBS) runs. The coating design starts with refining a 17-pair (34-layer) SiO$_2$/Nb$_2$O$_5$ Bragg stack with the six bottom layers fixed. The target is set to >90% R at 970-980 nm, 2.5$\pm$0.5% T at 1540-1580 nm, -2000$\pm$500 fs^2 at 1545-1575 nm. After the first refinement, an automatic needle optimization is performed, followed by the de-sensitization process to make the coating more robust against the fabrication error at the price of a larger deviation from the target.

Figure 3-9 shows the design results. The coating is composed of 27 layers of alternating SiO$_2$/Nb$_2$O$_5$ with a total physical thickness of 7.44 μm. The reflectivity at 1560 nm is 97% for a large beam, but it drops to about 92% for a 5-μm radius beam due to the divergence effect[1]. The dispersion curve is also overlaid with 1-σ deviation due to the 0.5%-thickness error. The deviation of $\pm$300~400 fs^2 is acceptable to our design.

---

[1]Details about the simulation of the divergence effect can be found in Appendix. B.
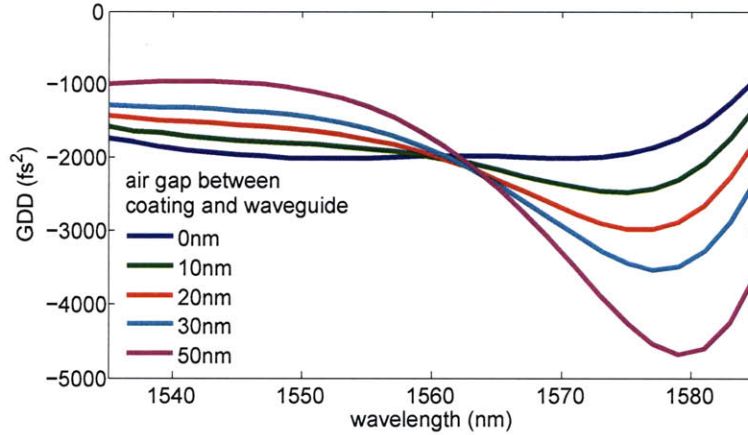
Figure 3-10: Effect of the airgap between the output coupler coating and the chip edge.

The coating is optimized for the incident medium of P-doped waveguides, so different incident medium will significantly affect the performance. For example, even tens of nanometers of airgap between the coating and the chip can dramatically change the dispersion response over the wavelength (Figure 3-10). Two solutions are possible; the coating is deposited directly on the waveguide chip, or the airgap can be filled with index-matching fluid of similar index as the P-doped waveguide to eliminate this effect.

3.2 External multiplication by resonators

3.2.1 Theory

The pulse repetition rate can be multiplied by using ring resonators or Fabry-Perot resonators. The resonator favors some frequencies that fit the resonator path length and functions as a filter in frequency domain. Figure 3-11 shows examples and frequency responses of Fabry-Perot resonators. The planar resonator with partial reflectors and the ring resonator function the same way in that the successive reflections are interfered with each other.

The phase difference between each succeeding reflection is given by δ, assuming
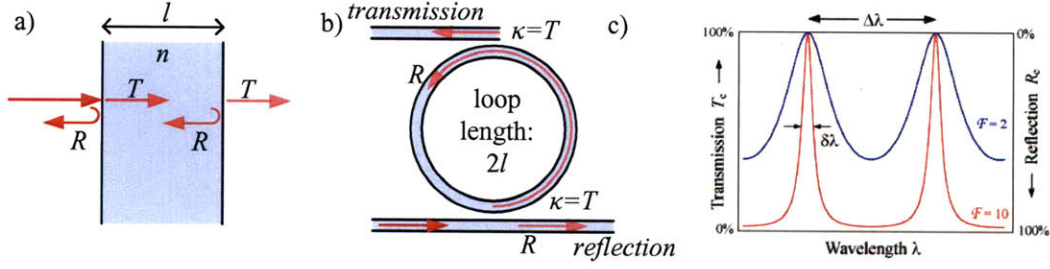
Figure 3-11: (a), (b) Exemplary schematics and (c) frequency response of Fabry-Perot resonators. (a) is a resonator sandwiched between two partial reflectors with reflectance R, and (b) is a ring resonator with coupling ratio $\kappa = T$. The reflection frequency response of (a) is the same as that of (b) and so does the transmission, assuming that the ring perimeter is $2l$ and refractive index is n.

perpendicular incidence [51],

$$\delta = \left(\frac{2\pi}{\lambda}\right) 2nl. \tag{3.2}$$

If both surfaces have a reflectance R, the transmittance function of the etalon is given by

$$T_e = \frac{(1-R)^2}{1+R^2-2R\cos\delta} = \frac{1}{1+F\sin^2(\delta/2)} \tag{3.3}$$

where $F = \frac{4R}{(1-R)^2}$ is the coefficient of finesse. Maximum transmittance ($T_e = 1$) occurs when the optical path length difference $2nl$ between each transmitted beam is an integer multiple of the wavelength, such that $\delta = 2m\pi$. In the absence of absorption, the maximum reflectivity is given by

$$R_{\max} = 1 - \frac{1}{1+F} = \frac{4R}{(1+R)^2} \tag{3.4}$$

and this occurs when the path difference is half an odd multiple of the wavelength, or $\delta = (2m+1)\pi$. The wavelength separation between adjacent transmission peaks is called the free spectral range (FSR) of the resonator, given by

$$\Delta\lambda = \frac{\lambda_0^2}{2nl+\lambda_0} \approx \frac{\lambda_0^2}{2nl} \tag{3.5}$$
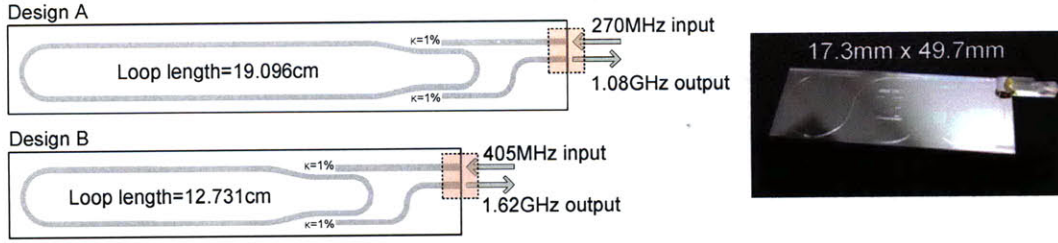
Figure 3-12: A schematic and photograph of the ring filter chip. Each design is fabricated in a separate chip, but each chip measures the same dimension.

where λ_0 is the central wavelength of the nearest transmission peak. The *finesse* is defined by the ratio of $\Delta\lambda$ to $\delta\lambda$, indicating how narrow the frequency selectivity is, relative to the FSR.

$$\mathcal{F} = \frac{\Delta\lambda}{\delta\lambda} = \frac{\pi}{2\arcsin(1/\sqrt{F})} \tag{3.6}$$

This is commonly approximated for $R > 0.5$ by

$$\mathcal{F} \approx \frac{\pi\sqrt{F}}{2} = \frac{\pi\sqrt{R}}{1-R}. \tag{3.7}$$

3.2.2 Ring filter waveguide chip

Ring filters can function as Fabry-Perot resonators to multiply the pulse repetition rate. Ring filters are fabricated by using a phosphor-doped (P-doped) silica waveguide on silicon-on-insulator (SOI). The P-doped waveguide has index contract of 0.75% and a cross-sectional dimension of 4 μm(width) by 7 μm(height). Figure 3-12 shows the schematic of the ring filters with two different loop lengths of 19.096 cm and 12.731 cm, which corresponds to FSRs of 1.08 GHz and 1.62 GHz respectively. The two different loop lengths are fabricated on separate chips. A photograph of the chip is also shown at the right side of Figure 3-12 with a pair of fiber attached for the input and the output. The chip measures a dimension of 17.3 mm by 49.7 mm.

The temperature-dependent frequency response of the ring filter chips is measured by using a setup illustrated in Figure 3-13. An electric heater with pressure-sensitive adhesive (Omega KHLV-0502/10-P) is attached on the surface of a ring filter chip. A
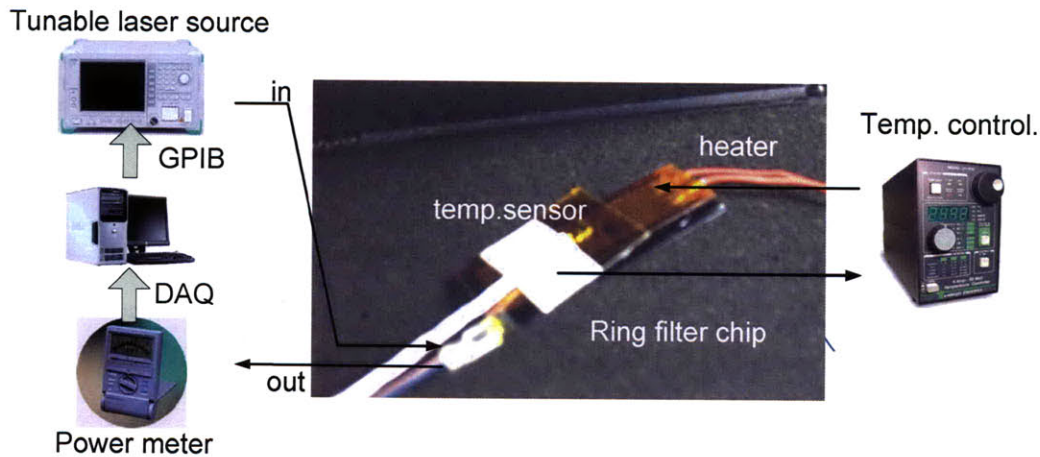
Figure 3-13: Experimental setup to measure the frequency response of the ring filter chips.

resistance temperature sensor (RTD, Omega SA1-RTD-MTP) is attached on top of the heater. The heater and RTD are connected to a temperature controller (Wavelength Electronics LFI-3751) to control the temperature on the chip surface, and consequently the loop length. The chip with the heater and RTD attached is enclosed in a plastic case with sponge inside to insulate the chip from the environment.

A tunable laser source (Anritsu MG-9638A) is injected into one port of the chip and the output power from the other port is measured by using a power meter. The resolution is 1 pm or 125 MHz at 1550 nm and the linewidth is 50 MHz. A computer sweeps the wavelength of the laser source through the GPIB interface and, at the same time, collects data from the power meter through a data-acquisition (DAQ) board (National Instrument PCI-6013e). The wavelength of the tunable laser source is swept from 1550.000 nm to 1550.200 nm with a resolution of 1 pm. The control software is written in Matlab®.

Output power along the wavelength are plotted in Figure 3-14 for both designs at the surface temperature of 53°C and 89°C respectively. Each output power curve is fit to the predicted spectral response of a Fabry-Perot resonator. Irregular peak heights originate from insufficient resolution of the tunable laser source. The transmission minima determine the coupling ratio κ and the FSR is determined such that the predicted transmission from Equation 3.3 overlaps with the measured spectral response
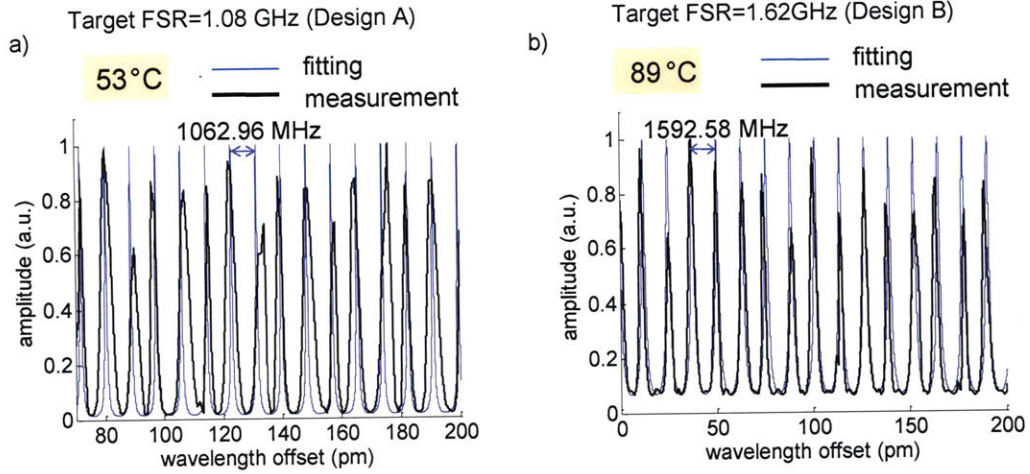
Figure 3-14: Wavelength-dependent response of the ring filter chips. (a) Design A with a target FSR of 1.08 GHz, and (b) Design B with a target FSR of 1.62 GHz. Horizontal axis is the offset wavelength from 1550.000 nm.

	Design A	Design B
Loop length	19.096 cm	12.731 cm
Measured FSR	1063.00 MHz at 32°C	1592.66 MHz at 26°C
	1062.96 MHz at 53°C	1592.58 MHz at 89°C
	1062.94 MHz at 80°C	
Tunability	1.20 kHz/°C	1.27 kHz/°C
Estimated κ	0.25	0.45
Transmission minima	2%	8%
Finesse	10.8	5.3

Table 3.2: Measured parameters of the ring filter chips.

with a minimum difference. The measured FSRs are smaller than the target values, which indicates that the effective index was over-estimated at the design stage.

FSRs from different chip temperatures are compiled in Table 3.2. The FSR decreased with a rate of 1.20 kHz/°C and 1.27 kHz/°C for design A and design B respectively. The rate corresponds to about 1 ppm that is one order of magnitude smaller than the temperature-induced index change of fused silica. The discrepancy may be attributed to the difference between the measured temperature and the actual waveguide temperature. The coupling ratios are estimated to be 0.25 and 0.45 from the transmission minima of 2% and 8% by using Equation 3.4, for design A and design B respectively. The variation indicates that the fabrication of ring resonators would need better control on the coupling ratio.

Although the ring filter chips are designed and fabricated to multiply the repetition rate of the mode-locked waveguide lasers in Figure 2-10, the FSR is too far from the multiplied repetition rate. The repetition rate of the laser is 394 MHz, so the multiplied repetition rate is 394×4=1576 MHz, which is 16 MHz away from the filter FSR and thus, out of the thermal tuning range. The repetition rate of the laser can be increased by dicing away 3032 μm from the SBR-side edge with the accuracy of ±2.5 μm. However, this accuracy is not trivial for conventional dicing and polishing process. The ring filter chip can be re-fabricated to fit the laser repetition rate. On the other hand, the ring filter chip can be applied in a reverse way: a laser with capability of tunable repetition rate can be locked to the stable integrated ring resonator by controlling the cavity length with a piezo-electric actuator.

Filtering broadband signals

The ring filter experiment above was performed over a sub-picometer range in the wavelength domain. However, since we consider applying the filter for multiplying the pulse repetition rate, broader bandwidth behavior also needs investigation. The dispersion of the waveguide makes the effective loop length look different for different wavelengths. The following calculation estimates how the second order dispersion of the ring filter changes the FSR.

76

The transmission maxima occur when the half phase shift per loop, $\delta/2$, is integer-multiple of π, that is, $\delta = 2m\pi$, where m is an integer (see Equation 3.3). The phase shift per loop is represented by the physical length of the loop multiplied by the frequency-dependent propagation constant:

$$\delta = \beta(\omega)L = 2m\pi, \tag{3.8}$$

where L is the physical length of the loop. Let ω_n and ω_{n+1} be two consecutive frequencies ($\omega_{n+1} > \omega_n$) that satisfy Equation 3.8.

$$\begin{aligned} \beta(\omega_n)L &= n\pi \\ \beta(\omega_{n+1})L &= (n+1)\pi \end{aligned} \tag{3.9}$$

The propagation constant can be expanded about ω_0.

$$\beta(\omega) = \beta_0 + \frac{\partial\beta}{\partial\omega}(\omega - \omega_0) + \frac{1}{2}\frac{\partial^2\beta}{\partial\omega^2}(\omega - \omega_0)^2 + \cdots \tag{3.10}$$

We consider the effect of only the second order dispersion. The propagation constants are given at ω_{n+1} and ω_n:

$$\beta_0 + \frac{\partial\beta}{\partial\omega}(\omega_{n+1} - \omega_0) + \frac{1}{2}\frac{\partial^2\beta}{\partial\omega^2}(\omega_{n+1} - \omega_0)^2 = \frac{2(n+1)\pi}{L} \tag{3.11}$$

$$\beta_0 + \frac{\partial\beta}{\partial\omega}(\omega_n - \omega_0) + \frac{1}{2}\frac{\partial^2\beta}{\partial\omega^2}(\omega_n - \omega_0)^2 = \frac{2n\pi}{L}. \tag{3.12}$$

Subtracting Equation 3.12 from Equation 3.11,

$$\frac{\partial\beta}{\partial\omega}(\omega_{n+1} - \omega_n) + \frac{1}{2}\frac{\partial^2\beta}{\partial\omega^2}\left[(\omega_{n+1} - \omega_m)2\omega_m - (\omega_{n+1} - \omega_n)2\omega_0\right] = \frac{2\pi}{L} \tag{3.13}$$

where approximation of $\omega_{n+1} + \omega_n \simeq 2\omega_n$ was used. The FSR is calculated:

$$FSR = \frac{\omega_{n+1} - \omega_n}{2\pi} = \frac{1}{\left[\frac{n_g}{c} + \beta_2(\omega_n - \omega_0)\right]L}, \tag{3.14}$$

77

where n_g/c is the group delay and β_2 is the second order dispersion in s^2/m. Note that now the denominator contains another term proportional to the second order dispersion and the distance from the center frequency.

For a numerical example, consider a pulse with an optical bandwidth of 20 nm centered at 1565 nm. The repetition rate is assumed to be matched to the loop length 12.731 cm at 1565 nm. The FSR at the center wavelength is 1593.167 MHz. If the ring filter is dispersion-free and lossless[2], the FSR in the frequency domain will be constant over the optical bandwidth. In order to see the effect of the dispersion, the second order dispersion is assumed to be -25 fs^2/mm. , the FSRs at 1555 nm and 1575 nm become 1593.104 MHz and 1593.228 MHz respectively, which corresponds to about 60 kHz change per 10 nm. The ratio of the FSR change to the original FSR is less than 10^{-4} and almost negligible since the finesse of the fabricated ring filter is less than several tens.

One practical issue is the wavelength-dependent coupling ratio of the ring filter. Different coupling ratios over the bandwidth will produce different suppression ratios of unwanted modes because the minimum transmission is a function of the coupling ratio.

3.3   External multiplication by pulse interleaving

Pulse interleaving is another way to multiply the repetition rate externally. A train of pulses with a period of T is split into two paths through a 50:50 splitter, where only one path is delayed by $T/2$ and then, the two paths are combined. Consequently, the output will have a pulse every $T/2$, or at a doubled repetition rate. By repeating the same process n times, we can multiply the repetition rate by a factor of 2^n at the price of a reduced output power. We begin this section with a principle of operation and continue with several experimental examples.

$$1 \xrightarrow{\quad} c_1 \quad\quad c_2 \xrightarrow{\quad} \sqrt{c_1 c_2} + \sqrt{(1-c_1)(1-c_2)}\exp(-j\omega d_1)$$

delay: d_1
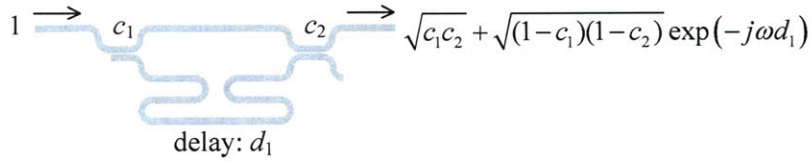
Figure 3-15: Schematic of a simplified pulse interleaver. Note that ω is a frequency in the RF domain.

3.3.1 Theory

A typical pulse interleaver is described in Figure 3-15. Input field $E_i = 1$ is injected into the coupler with coupling ratio c_1 and split to c_1 and $1 - c_1$, where the latter one experience the time delay of d_1. Then, the two paths are combined by another coupler with coupling ratio c_2. The output field E_o and intensity I_o are written as

$$E_0 = \sqrt{c_1 c_2} + \sqrt{(1-c_1)(1-c_2)}\exp(-j\omega d_1) \tag{3.15}$$

$$I_o = E_0 E_0^* \tag{3.16}$$

$$= c_1 c_2 + (1-c_1)(1-c_2) + 2\sqrt{c_1 c_2(1-c_1)(1-c_2)}\cos(\omega d_1), \tag{3.17}$$

where the frequency ω is in the RF domain.

Consequently, the output of the interleaver possesses a frequency-dependent response with a sinusoidal shape. $\omega d_1 = 2n\pi$ maximized the output, while $\omega d_1 = (2n + 1)\pi$ minimizes the output, where n is an integer. Assume that the incoming pulse train has a repetition rate of f_{rep}. Then, $d_1 = 1/2f_{rep}$ will maximize $2nf_{rep}$ components and minimize every $(2n+1)f_{rep}$, leaving only $2nf_{rep}$ components or multiplying the repetition rate by a factor of 2. The suppression ratio, S, is defined as how much the $(2n + 1)f_{rep}$ component is suppressed over $2nf_{rep}$ component. With ideal coupling ratios of $c_1 = c_2 = 0.5$ and an exact delay of $d_1 = 1/2f_{rep}$, S should be infinity, but practically it is not.

Figure 3-16 illustrates the frequency response of a single-stage pulse interleaver with f_{rep}=500 MHz, $d_1 = 1$ ns and both coupling ratios of 50.5%. Every GHz sits on extrema at 0 dBm, while every GHz plus/minus 500 MHz is suppressed down to

---

[2]The loss is known to be 0.2 dB/m for the P-doped waveguides.
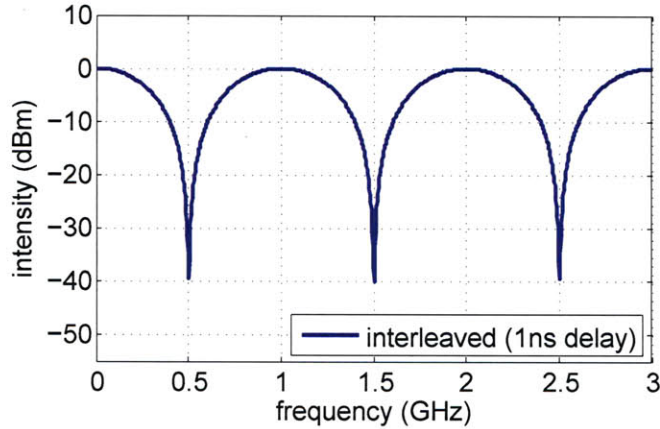
Figure 3-16: Radio frequency response of a single-stage pulse interleaver. The input repetition rate is f_{rep}=500 MHz and delay is $d_1 = 1$ ns. Both coupling ratios are assumed to be 50.5%.

-40 dB. Effectively, the input repetition rate of 500 MHz is multiplied to 1 GHz. The suppression is not infinity since the coupling ratios are not exactly 50.0%.

3.3.2 Free-space interleaving

For a fast prototype of repetition rate multiplication, we employ an intuitively simple method. Three stages of pulse interleaving are used to achieve a repetition rate multiplication by a factor of 8. In each stage of Figure 3-17(a), the pulse input is split into two paths, and a precisely controlled delay is imposed on one path, and those paths are combined into a collimator. A knife-edge on a linear stage, not shown in Figure 3-17, attenuates the beam power at the shorter path to compensate the beam divergence effect. Thus, the mode shapes from the two paths are different, and a pair of collimators are used to equalize the mode shapes for a next interleaver. The results are shown in Figure 3-17(b) and (c). Signal-to-background ratio of 30 dB is achieved in the frequency domain and stable pulse train is observed on the sampling scope trace.
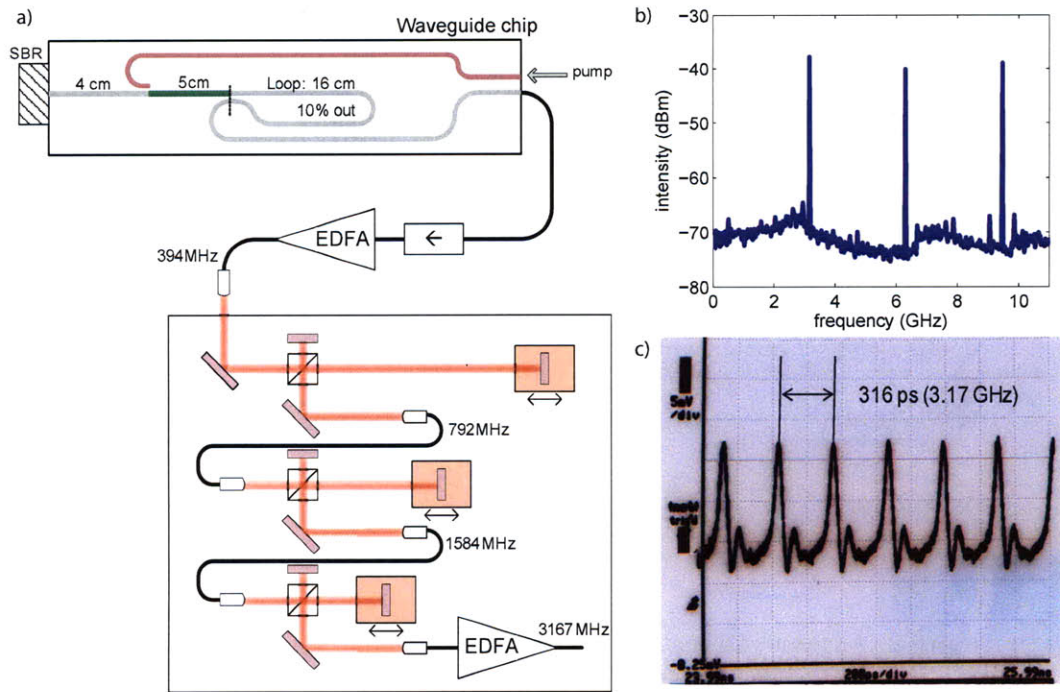
Figure 3-17: (a) Setup schematic for the repetition rate multiplication of the 400 MHz waveguide laser, (b) RF spectrum and (c) sampling scope trace.

3.3.3 Interleaver integrated with mode-locked waveguide laser

We demonstrated a 2-GHz optical pulse train from an integrated waveguide chip that consists of a mode-locked femtosecond waveguide laser and a repetition rate multiplication device. The laser generates 285-fs pulses at 500 MHz, with a cavity being composed of a 5.0-cm section of Er-doped aluminosilicate waveguide and a 14.8-cm section of P-doped silica waveguide for dispersion engineering. The repetition rate of 500 MHz is multiplied to 2 GHz with more than 15 dB suppression via integrated pulse interleavers.

The experimental setup is depicted in Figure 3-18. The waveguide chip contains three sub-components; a laser cavity to generate femtosecond pulses at a fundamental repetition rate of 500 MHz, a pulse interleaver to multiply the repetition rate to 2 GHz, and an amplifier. The laser cavity consists of a 5.0-cm-long erbium-doped (Er-doped) waveguide with a group-velocity dispersion of 60 fs^2/mm. A 14.8-cm section of phosphor-doped (P-doped) silica waveguide with a dispersion of -24 fs^2/mm is used

81
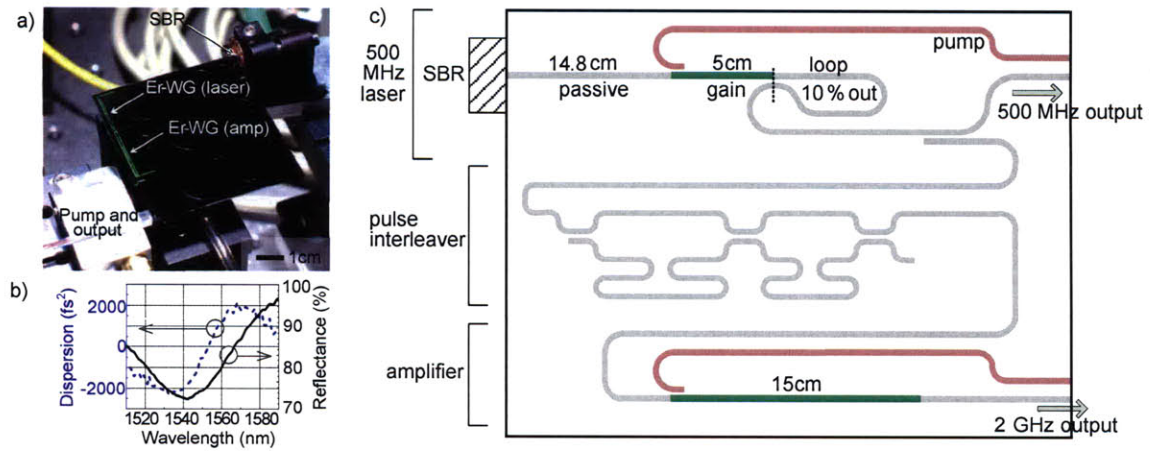
Figure 3-18: 500 MHz / 2 GHz waveguide laser: (a) experimental setup, (b) dispersion and reflectance data of the SBR and (c) chip schematic.

to obtain a net anomalous intracavity dispersion and enable soliton mode-locking [45]. A loop mirror is used at one end to provide a 10% output coupling, while the other end is butt-coupled to an external SBR. The SBR is a commercial unit (Batop) with a 14% modulation depth, a 2-ps recovery time, and a saturation fluence of 25 $\mu J/cm^2$. Pump power is provided by an external 980-nm laser diode. The laser operates with 175 mW of cavity-coupled pump power; the intracavity signal power is measured to be 4 mW, corresponding to a 10 pJ intracavity pulse energy. The laser output is split by a 3-dB coupler, in order to feed the interleaver and a separate output port.

Each stage of the interleaver splits the input beam into two paths, delays one of them by the corresponding half period of the input pulse train, and combines the original pulse train with its delayed version, such that the repetition rate is doubled. Two stages of the pulse interleaver convert the repetition rate from 500 MHz to 2 GHz. The amplifier recovers the optical power lost through the pulse interleaving and further increases the output power of the overall integrated system.

Figure 3-19 depicts the measurement results obtained so far. The 8.8-nm full-width half-maximum (FWHM) optical bandwidth enables 285-fs duration transform-limited pulses. The laser typically operates at 1560 nm as in Figure 2-11, but, at that wavelength, the SBR is positively dispersive with +1200 fs^2. This is sufficient positive dispersion to make the total cavity dispersion positive and disable soliton
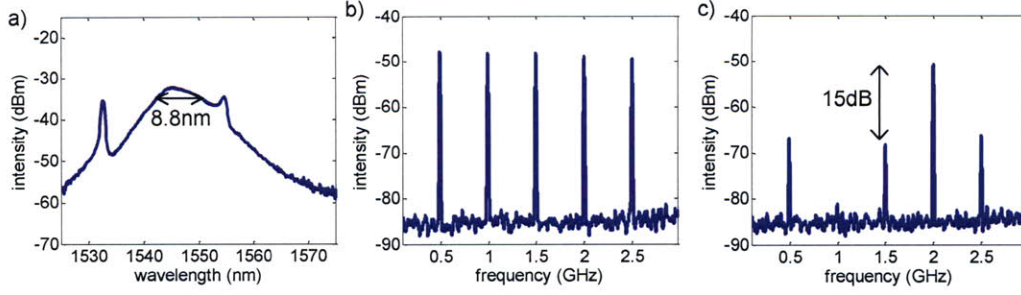
Figure 3-19: Measurement traces: (a) optical spectrum, (b) RF spectrum at the 500 MHz output port, and (c) RF spectrum at the 2 GHz output port. Both RF spectra are measured over 3 GHz span with 10 MHz resolution.

mode-locking, because the integrated laser cavity by itself is negatively dispersive with only -1100 fs^2 per round trip. In order to achieve net negative dispersion, we slightly adjusted the butt-coupling losses between the SBR and the waveguide chip, which shifted the operating wavelength to 1545 nm, where the SBR has negative dispersion of -1500 fs^2. As a consequence, stable soliton mode-locking is obtained although the increased cavity losses significantly reduces the output power. In the future, the positive dispersion of the Er-doped waveguide can be reduced by increasing its thickness (Section 3.1.3). Then, the negative dispersion of the laser cavity itself could be as large as -4000 fs^2 per round trip so that even the positive dispersion of +1200 fs^2 the SBR at 1560 nm would not interfere with soliton formation.

The laser is self-starting. As the pump power is increased, the laser first operates in a mode-locked Q-switching state before transitioning to a continuous-wave soliton mode-locked state at a pump power of 150 mW. The RF spectrum at the 500-MHz output port indicates a stable pulse train at a repetition rate of f_{rep}=500.5 MHz.

The first and second stages of the pulse interleaver suppress the sidebands at the 1 and 2 GHz harmonic by more than 30 dB and 15 dB respectively. The incomplete suppression can be attributed to mismatched delay lengths and/or deviation from ideal coupling ratios of 50:50. Further investigation of the interleaver is presented in Figure 3-20. (a) and (b) compares the input and the output of the interleaver, where the input is the pulse train from a 41-MHz mode-locked Er-fiber laser (Figure 5-3). The fiber laser source is injected through the 500 MHz laser output port. In (b),

83
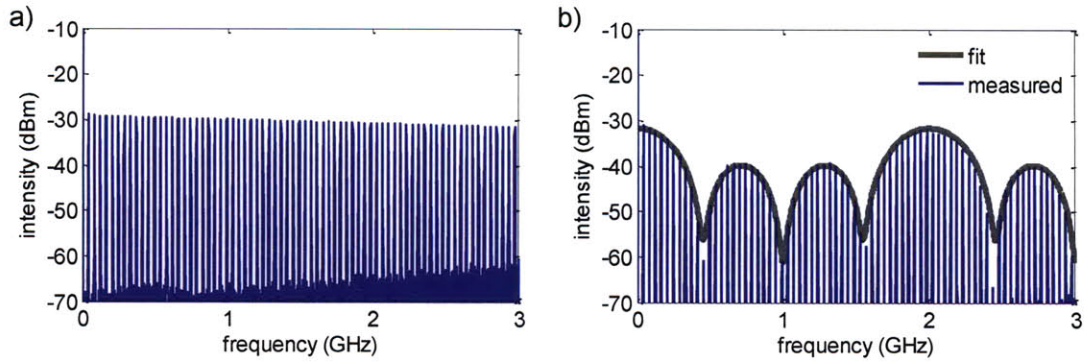
Figure 3-20: Investigation of the waveguide interleaver. (a) RF spectrum of a mode-locked laser with a repetition rate of 41 MHz that is injected through the 500 MHz output port, (b) RF spectrum at the 2GHz output port with the on-chip amplifier turned on and with an overlay of a calculated fit that uses coupling ratios of 41%, 67%, 55% respectively for the first, the second and the third coupler.

the frequency peaks around 500 MHz, 1 GHz, 1.5 GHz and 2.5 GHz are suppressed as much as 30-35 dB, whose envelops are fit to a simulation model with a thicker gray line. Note that the notches at 500 MHz, 1.5 GHz and 2.5 GHz are slightly off toward the 0, 2, 4, ... GHz combs by 40-50 MHz. The deviation is attributed to the imperfect coupling ratio, and this particular situation of sharing the second coupler between the two interleavers. The coupling ratios of 41%, 67%, and 55% respectively for the three couplers in the chip, are reasonable estimations that fit the measured interleaver response. This non-ideal coupling ratios limit further suppression of the sidebands, but the suppression can be easily enhanced by adding tuning capabilities for both the delay and the coupling ratio (see section 3.3.4).

Reproducibility and long-term stability

The 500-MHz waveguide laser shown above uses a small gap between the waveguide chip and the SBR. Due to the mechanical drift of the gap, the laser could not remain mode-locked more than 10 minutes. Different SBRs in the lab were tried, but none of them could satisfy the proper dispersion, recovery time, and saturable/nonsaturable loss at the same time. For example, an in-house SBR (VA89: 22-pair $Al_{0.95}Ga_{0.05}As$/GaAs mirror, 60 nm $In_{0.57}Ga_{0.43}As$ in quarter-wave GaAs cladding,

84
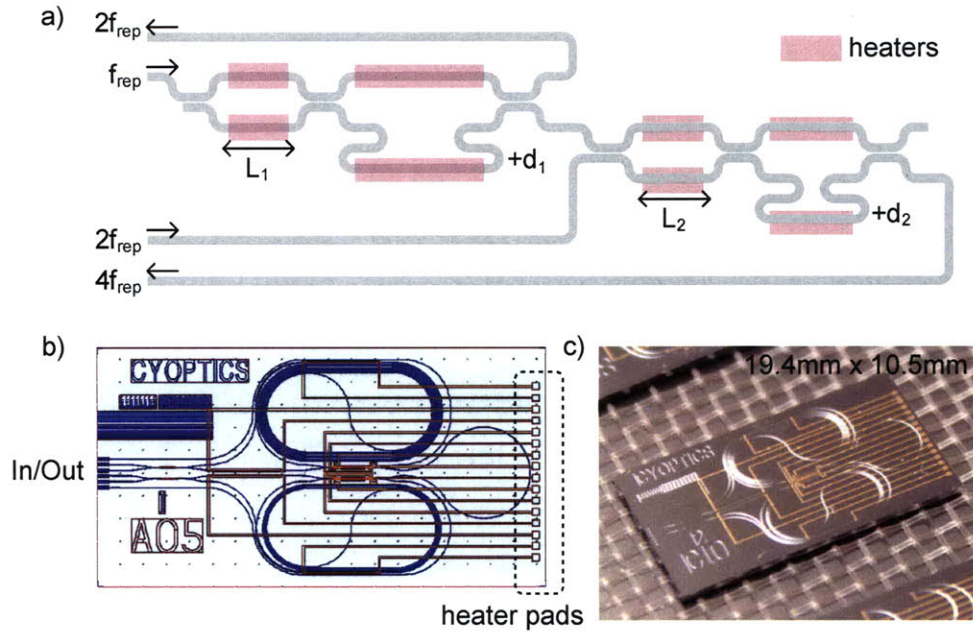
Figure 3-21: Tunable waveguide interleavers. (a) Schematic, (b) layout, and (c) a photograph of the chip. Chip layout courtesy of CyOptics.

$Al_{0.95}Ga_{0.05}As$/GaAs resonant coating) has enough modulation depth of 11%, but its dispersion is almost zero at 1560 nm. A VA89 coated with pump reflective coatings (PRC) has -1300 fs^2 at 1560 nm, but the PRC makes the SBR too lossy to enable enough intracavity power.

The gap can be removed if the normal dispersion of the Er-waveguide becomes smaller, which can be implemented by re-fabricating the waveguide chip with a thicker layer of Er-doped waveguide, as in the case of Section 3.1.3.

3.3.4 Tunable waveguide interleaver chips

As shown in the interleavers of above section (Figure 3-20), the suppression of sidebands in the frequency domain is limited by imperfect coupling ratios and/or delay lengths of the interleavers. If the coupling ratios and the delay lengths can be tuned, the sideband suppression will be enhanced.

Figure 3-21(a) illustrates the schematic of a tunable interleaver that can adjust the coupling ratio and the delay length. One interleaver chip contains two stages of

85

	f_{rep}	$4f_{rep}$
Design 1	500 MHz	2 GHz
Design 2	625 MHz	2.5 GHz
Design 3	2.5 GHz	10 GHz

Table 3.3: Tunable waveguide interleaver chips: designs for various repetition rates.

interleaver. Each interleaver splits the input into two paths by using a tunable coupler and impose a tunable delay on only one path before combining the two paths.

The tunable coupler is a Mach-Zehnder interferometer (MZI) with identical arm length of L_1 and L_2 respectively for the first stage and the second stage. $L_1 = L_2$ is about 2 mm. With thermo-optic coefficient of 8.5 ppm (Table 6 in Leviton *et al.* [52]), a temperature change of 30°C can change the optical length of one arm of the coupler by $\lambda/2$ at 1550 nm. In other words, 30°C can change the coupling ratio 0% to 100%. There are eight heaters on one chip in total. Four heaters are deposited on each interleaver, where two heaters are used for the MZI and the other two are used for the delay path.

The delay lengths d_1 and d_2 are determined by the initial repetition rate f_{rep} to start the multiplication from. Three different sets of d_1 and d_2 are fabricated for f_{rep} of 500 MHz (design 1), 625 MHz (design 2) and 2.5 GHz (design 3), producing three different tunable interleaver chips (Table 3.3). Each design multiplies the pulse repetition rate from 500 MHz to 2 GHz, from 625 MHz to 2.5 GHz, and from 2.5 GHz to 10 GHz. The design 2 and design 3 can be cascaded to generate a 10-GHz frequency comb from 625-MHz pulses for the OAWG application (Section 1.3.2).

The chip layout is shown in Figure 3-21(b). Inputs and outputs are accessed at the left edge of the chip, while the heater pads are grouped near the right edge of the chip. The edge of the chip with input/output is polished with 8-degree angle to avoid back-reflection[3]. The core waveguide is fabricated with a Ge-doped fused silica that provides index contrast of 1.5% and thus, allows more compact integration than the P-doped waveguide. The cross-sectional dimension of the core waveguide is 4 μm × 4 μm and the mode is tapered out at the chip edge such that an efficient coupling

---

[3]The index contrast of 1.5 % requires an angle higher than 11 degree, but a proprietary structure is used such that 8-degree is enough to reject the back-reflection.
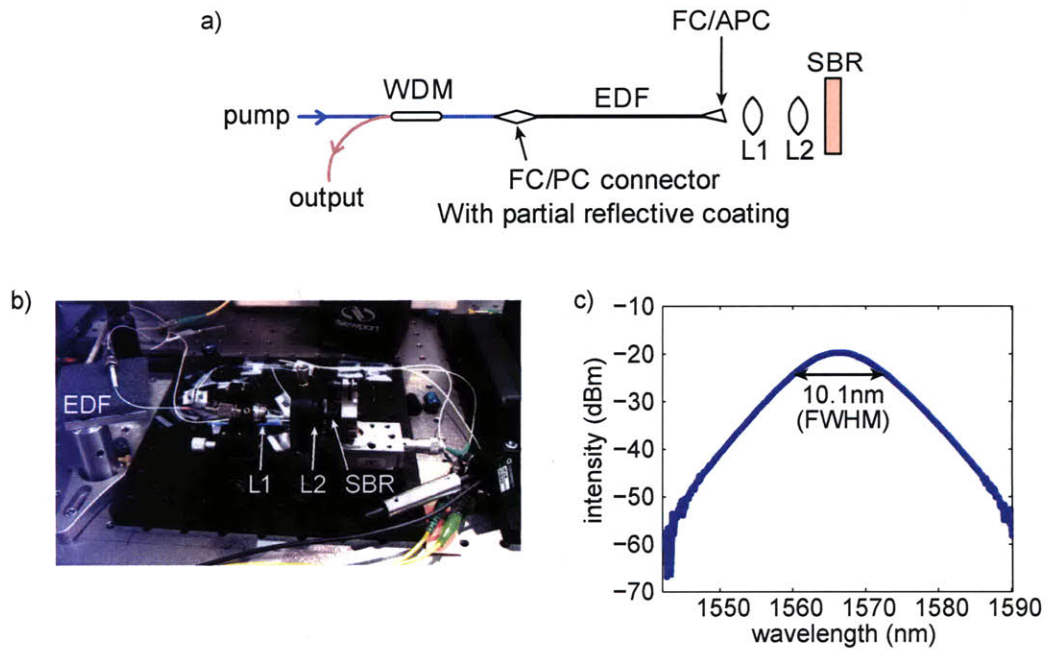
Figure 3-22: A 625-MHz mode-locked laser to test the tunable waveguide interlaver chips. (a) Schematic, (b) a photograph of the experimental setup, and (c) optical spectrum.

can be made with a SMF-28 fiber.

Mode-locked laser source

A mode-locked laser source at a tunable repetition rate around 625 MHz is constructed to test the tunable interleaver chips, especially design 2 and design 3.

The mode-locked laser consists of a 12.5-cm Er-doped fiber (Liekki Er80-8/125), a pair of aspheric lenses, and a custom-grown SBR (Figure 3-22). One end of the EDF is connectorized with a FC/PC connector and mated to another FC/PC connector with a 90% reflectivity coating. The other end of the EDF is connectorized with a FC/APC connector to minimize back-reflection because even a small back-reflection can counteract the mode-locking. The beam from the angled end of the EDF is collimated by using L1 (Thorlabs F240APC-1550) that accepts FC/APC connector and is focused on to the SBR by using L2 (Thorlabs A240TM-C). The spot diameter on the SBR should be very close to the mode field diameter ($\sim$9 μm) of the EDF since both L1 and L2 have the same focal length of 8 mm.

The SBR is used to start and stabilize the mode-locking. The Bragg mirror, designed for a center wavelength of 1550 nm, consists of a 22-pair quarter-wave stack of $Al_{0.95}Ga_{0.05}As$ and GaAs. On the surface of the high reflectivity mirror, a 60-nm thick $In_{0.53}Ga_{0.47}As$ absorber is embedded in a half-wave cladding layer of GaAs. Then, the SBR is proton-bombard to reduce the long recovery time from 9 ps to 3 ps. The recovery time needs to be shorter than the butt-coupled SBR cases in Chapter 4, because the cavity loss is larger due to the free-space section. As the cavity loss increases, the noise on the pulse tail experiences higher gain and the pulse tail needs to be suppressed stronger by using a faster SBR.

☐ Laser alignment procedure

1. Align the collimator L1 so that the beam is parallel to the breadboard thread arrays.

2. Place camera a few cm away from where the focusing lens L2 will be placed. The SBR assembly should be taken out from the rail for clearance.

3. Connect a light source around 1560 nm to the WDM and align the camera so that the beam is centered on the sensor. The input light may need to be amplified.

4. Place the focusing lens L2 into the mount. Then adjust XY translation so that the beam on the camera overlaps with the position without the focusing lens. The XY translation mount is mounted perpendicular to the beam path as much as possible.

5. Mount the SBR assembly back on the rail. Align the SBR assembly by adjusting translation and gimbal rotations to achieve maximum output power.

The repetition rate of the laser can be tuned by adjusting the distance between L1 and L2 such that the repetition rate is matched to the interleaver delay length.

Figure 3-22(c) shows the optical spectrum of the laser with a FWHM width of 10.1 nm. The output power is 7.3 mW with 200 mW of pump power (pump diode current of 570 mA) launched into the EDF. The optical spectrum and output power
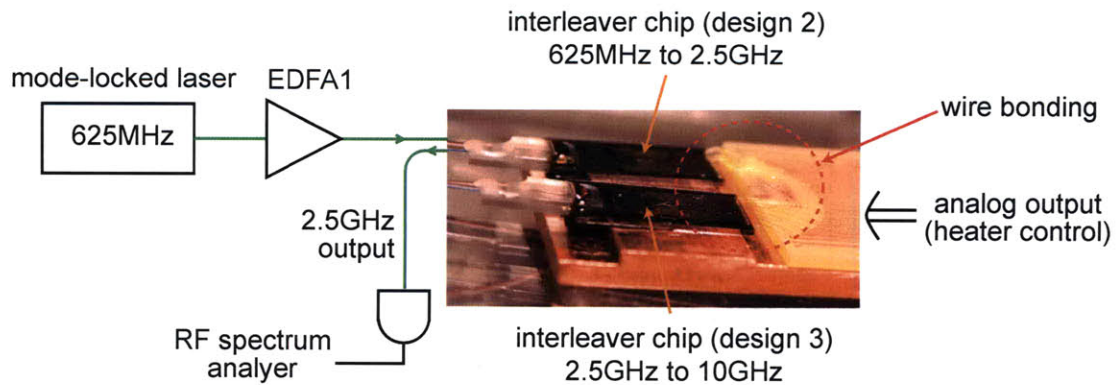
Figure 3-23: The schematic of the experimental setup to multiply the repetition rate from 625 MHz to 2.5 GHz. Interleaver chip of design 3 is also mounted for a future use.

is quite sensitive to the fiber twist/bent or the polarization status. The above results are obtained after trials and errors of twisting and bending fiber to achieve the widest optical spectrum. The repetition rate is tunable between 600 and 700 MHz.

Repetition rate multiplication from 625 MHz to 2.5 GHz

A tunable interleaver chip (design 2) is examined to demonstrate the repetition rate multiplication from 625 MHz to 2.5 GHz. The experimental work in this subsection was mostly done by Michelle Sander and Marcus Dahlem [53]. The experimental setup is sketched in Figure 3-23. The mode-locked laser output is amplified by an Er-doped fiber amplifier (EDFA) to about 30 mW and fed to the interleaver chip. The output is connected to a RF spectrum analyzer through a photodetector (EOTech ET-3500F).

The interleaver chip is fixed on a custom-machined copper mount by silver paste. The heater pads of the interleaver chip are wire-bonded to a PCB that connects to the analog output controlled by a computer[4]. The supplied power to each heater is limited to 30 mW to prevent any burning. The interleaver introduces loss of about 15 dB. The theoretical loss of the interleaver is 6 dB for the dual stages and the rest attributes to coupling or waveguide scattering losses.

---

[4]The heater pads are separated by 500-μm pitch, so conventional soldering is not possible.
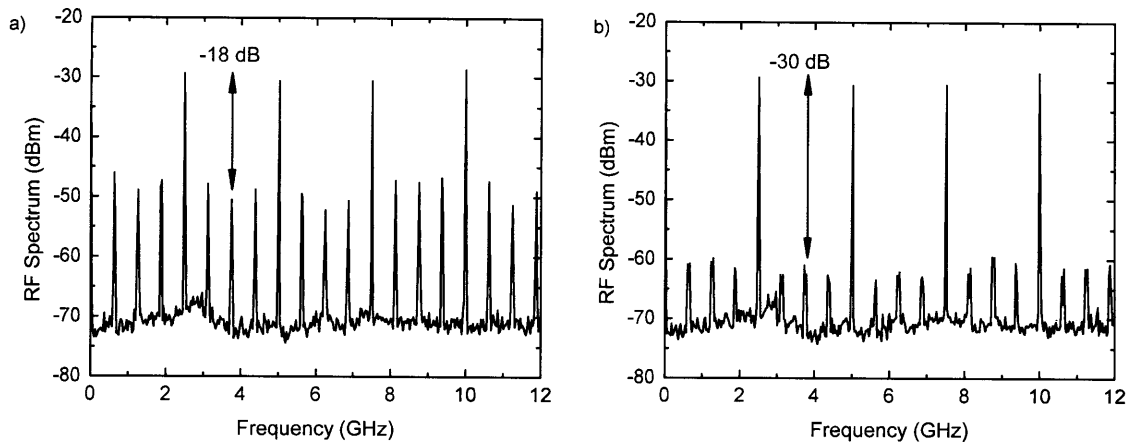
Figure 3-24: RF spectrum of the interleaver output (a) without thermal tuning and (b) with thermal tuning by using two heaters. Plots courtesy of Michelle Sander.

The RF spectra from the interleaver output are compared without and with thermal tuning, shown in Figure 3-24. Without thermal tuning, side-modes are suppressed by 18 dB from the 2.5-GHz peak and its harmonics. The suppression is enhanced to 30 dB with thermal tuning by using two heaters, one for each MZI coupler. What limits further suppression of the side-modes is considered to be that wavelength-dependent coupling ratio of the MZI couplers within the optical spectral range of the input pulses.

It also turns out that the heaters on the delay lines do not affect the suppression of RF side-modes noticeably. A heater on the MZI coupler can change the coupling ratio 0% to 100% with a temperature change of 30°C, while a heater on the delay line only changes the delay length at most by 0.02% with the same temperature change. The heaters on the delay lines are actually useful to fine-tune the pulse spacing to achieve the phase coherency between consecutive output pulses. Further optimization and analysis will be continued by Michelle Sander.

3.4   Summary

Several different approaches to increase the repetition rate of a femtosecond pulse train were discussed with experimental results.

The short Er-waveguide chip with the reduced cavity length can be applied to fundamentally mode-locked waveguide lasers with a repetition rate of 1.5-2 GHz. Compensatable normal dispersions were measured from the fabricated chips and an anomalously dispersive output-coupler coating was designed to compensate the normal dispersion of the waveguide cavity. Simulation results confirmed that the waveguide laser based on the fabricated chip can generate soliton pulses within the available intracavity power and dispersion.

Two methods to multiply the repetition rate externally were also discussed. The waveguide ring resonator chips demonstrated the possibility of repetition rate multiplication by frequency filtering based on a ring resonator. The pulse interleaving method was realized both on a free-space-based setup (from 394 MHz to 3.17 GHz, by factor of 8) and on a waveguide chip (from 500 MHz to 2 GHz, by factor 4). The sideband suppression of the waveguide chip interleaver was larger than 15 dB. The suppression enhancement up to 30 dB was demonstrated by using interleaver chips with tunable coupling ratios based on on-chip heaters.

3.5 Future work

3.5.1 1.5-2 GHz waveguide laser

The short waveguide chips in Section 3.1 require a coating run for the dispersion-compensating output coupler, in order to engineer the cavity dispersion and allow for the soliton formation. The coating is already designed in Section 3.1, but it has yet to be determined whether the coating is deposited on the waveguide chips or on fiber ferrules. The author recommends that the waveguide chips, instead of ferrules, are coated, because the coated ferrules would need index-matching fluid (Figure 3-10) that may degrade after long term operation and may also be difficult to clean. Additionally, the coating on the waveguide chips minimizes the intracavity loss by zero-gap between the coating and the waveguide. Since the coating run (IBS) is expensive, it is recommended that all waveguide chips are measured for their dispersion and as

many chips as possible are prepared for the coating run. However, the approach of depositing the coating directly on the chip needs confirmation on the possibility from the fabricator. If the fabricator, presumably Advanced Thin Films, cannot deposit the 7.44-μm thick coating on the narrow surface of the chip, the coating must be deposited on separate substrates, such as half-inch diameter fused silica cylinders. Then, the coated substrate is butt-coupled to the waveguide chip with index fluid applied, and the pump and the output are free-space coupled by using an aspheric lens.

3.5.2   Waveguide lasers with repetition rates >2 GHz

In order to increase the fundamental repetition rate above 2 GHz, the Er-doped waveguide needs to be shorter, in which case the laser may not produce enough intracavity power. Since the 5-cm Er-waveguide is already limiting the available intracavity power, higher gain per unit length should be implemented. Possible options include co-doping the waveguide with ytterbium or doping only with ytterbium for a higher absorption.

3.5.3   Repetition rate stabilization

The phase noise of the 400 MHz waveguide laser (Figure 2-11(f)), especially for offset frequencies smaller than several tens of kHz, can be further suppressed by using a feedback loop. The repetition rate of the waveguide can be locked to a stable quartz crystal oscillator in oven. A crystal in oven has superior noise characteristics to a free-running laser, especially for lower frequencies. There are some options to try to modulate the waveguide cavity length. First, we can try on-chip heaters that can have time constants of a few ms. Second, liquid crystal (LC) can be an alternative way to change the cavity length [54]. LC can change the refractive index three to four orders of magnitude more than any other methods. LC deposited on the core waveguide can adjust the effective index of a guided mode by controlling the voltage, with typical time constants of 10-100 μs.

Chapter 4

Er-doped fiber laser

Compact femtosecond Er-doped fiber lasers can enable a broad range of applications, not limited to the original motivation to prove the concept that the Er-doped waveguide laser can generate solitons through a anomalously dispersive cavity. Such fiber laser sources can be employed as a low-jitter light source for the extraction of high-quality microwave signal by using an integrated optical phase-locked loop (Chapter 6), for the characterization of low-noise superconducting photodetector (Section 1.3.4), and for optical arbitrary waveform generation (Section 1.3.2).

4.1   500 MHz Er-doped fiber laser

In this section, we demonstrate a simple, inexpensive and low-jitter passively mode-locked femtosecond erbium-doped fiber (EDF) laser by using a commercial SBR. Self-starting, it generates a pulse train at 491 MHz with a measured full-width half maximum (FWHM) pulse duration of 180 fs and an average output power of 12 mW. The integrated timing jitter from 1 kHz to 10 MHz is measured to be 20 fs, and the measured optical spectrum FWHM of 15.4 nm is in good agreement with the Fourier prediction of 15.2 nm for 180-fs pulses.

The experimental setup is depicted in Figure 4-1(a). The laser cavity consists of a 20.7-cm section of EDF (Liekki Er80-8/125) with group-velocity dispersion (GVD) of -20 fs^2/mm, small-signal gain of 0.4 dB/cm at 1570 nm for a pump power of 260 mW
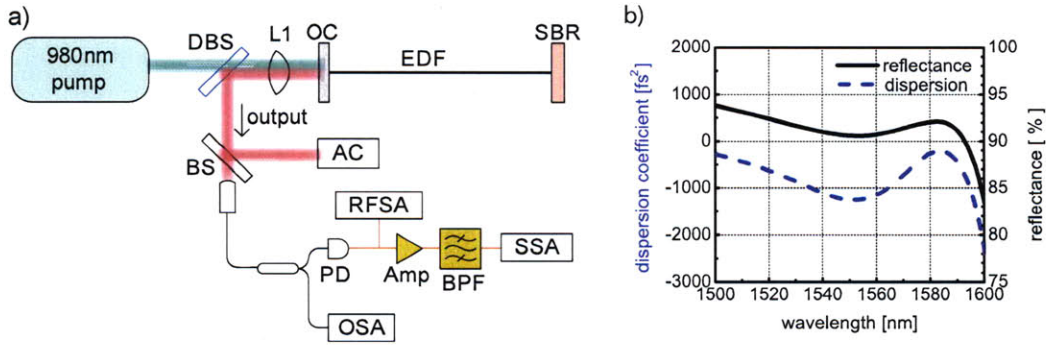
Figure 4-1: (a) An experimental setup for the linear soliton laser and (b) reflectance and dispersion of the SBR. DBS: dichroic beam splitter, OC: output coupler, PD: photodetector, BPF: band-pass filter.

and doping concentration of 4.8×10^{19} cm^{-3}. Using an anomalously-dispersive gain fiber eliminates the need for an additional fiber section for dispersion compensation, which would reduce the repetition rate. One end of the cavity is butt-coupled to an SBR, and the other to a dielectric mirror, which acts as the output coupler. The SBR is a commercial unit (BATOP GmbH) with 6% modulation depth, a 2-ps recovery time, and a saturation fluence of 50 μJ/cm^2. Its dispersion and reflectance are depicted in Figure 4-1(b). Pump light is provided by a 980 nm laser diode, free-space coupled through a dichroic beam splitter and focused by an aspheric lens through the output coupler and into the EDF. The output coupler transmits 10% of intracavity power over the wavelength range from 1520 nm to 1640 nm with negligible dispersion. The output signal follows the same path in reverse and is separated from the pump by the dichroic beam splitter. The output pulses are split into three branches by using a beam splitter and fiber couplers. The first branch is used to measure the auto-correlation, the second to monitor the microwave spectrum and phase noise with a 10 GHz photodiode, RF spectrum analyzer and signal source analyzer (Agilent E5052), and the third to monitor the optical spectrum.

Figure 4-2(a)-(b) depict the measured optical spectrum and interferometric non-linear autocorrelation trace (IAC). The optical spectrum analyzer measurement shows a 15.4 nm FWHM optical bandwidth, implying 168 fs transform-limited FWHM pulse duration, while the autocorrelation measurement results in a 180 fs FWHM duration.

94
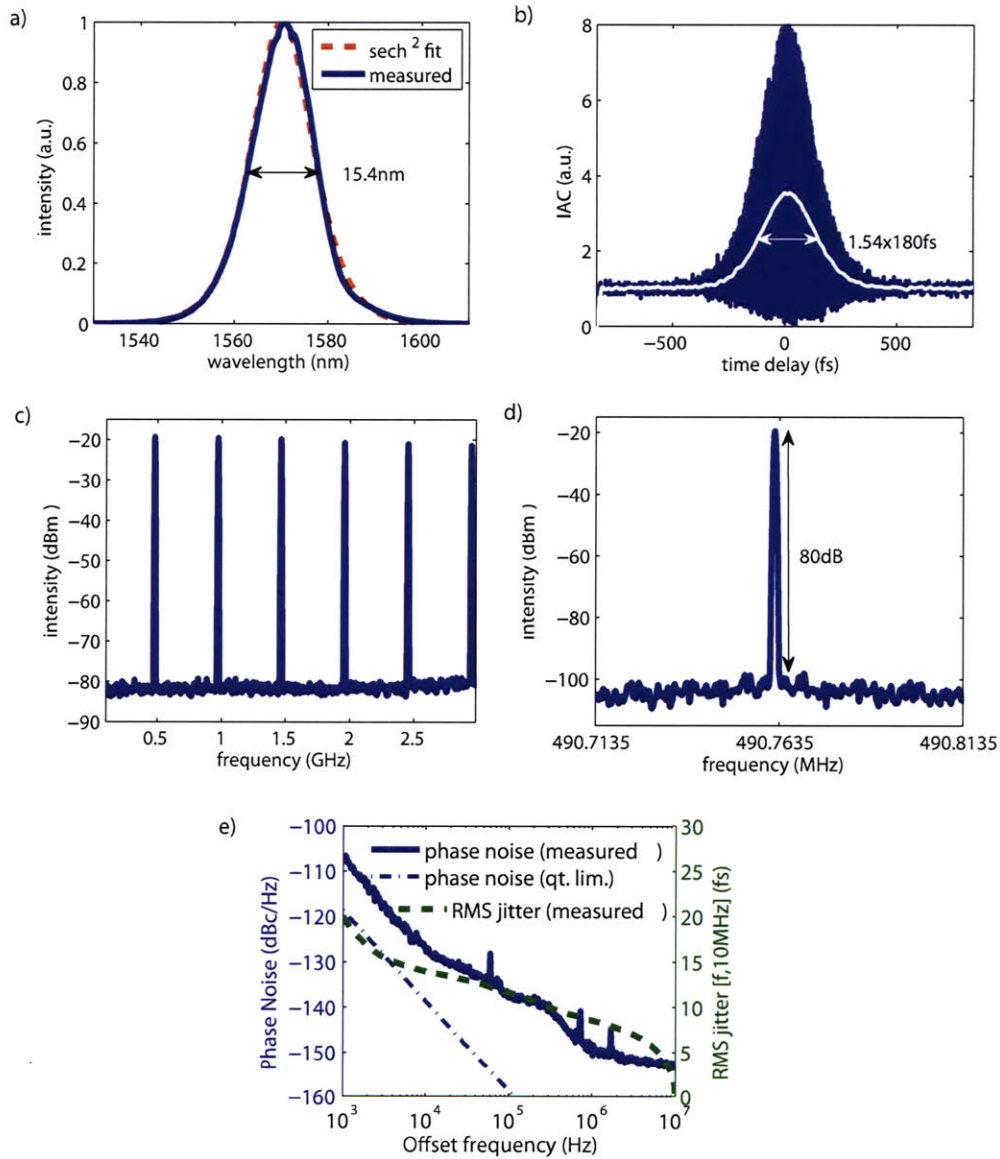
Figure 4-2: Experimental results at a repetition rate of 491 MHz. (a) Optical spectrum (b) Interferometric auto-correlation with inferred intensity autocorrelation (white) (c) RF spectrum spanning from 0 to 3 GHz with resolution bandwidth of 10 MHz (d) RF spectrum zoomed around the first harmonic with resolution bandwidth of 500 Hz) (e) Single-side-band (SSB) phase noise (solid) and integrated RMS jitter (dotted) , compared with calculated quantum limit of phase noise (dash-dotted).

The difference is attributed to the non-uniform gain profile of the EDF and the non-uniform dispersion profile of the SBR, causing a slight deviation of the measured optical spectrum from a sech^2 spectrum, as shown in Figure 4-2(a). The dispersion of free-space optical components, such as the output coupler substrate, focusing lens and mode-matching optics in the IAC setup, also contribute up to 6 fs of pulse broadening. The optical spectrum is centered around 1570 nm which is determined by the wavelength-dependent reflectivity of SBR and the gain spectrum at the operating power level. The above values were obtained with 260 mW of coupled pump power; the intracavity signal power was measured to be 121 mW, which corresponds to 251-pJ intracavity pulse energy. The laser self-starts; as the pump power increases, the laser first operates in an unstable Q-switched mode-locking state and then, changes to a continuous-wave soliton mode-locked state at a pump power of 95 mW. For pump powers greater than 300 mW, multiple pulsing occurs. As the pump power increases above 260 mW the optical spectrum became broader, but the pulse duration does not decrease correspondingly and the optical spectrum deviated further from a sech^2 fit.

Figure 4-2(c)-(e) show the radio-frequency (RF) spectrum and single side band (SSB) phase noise. The 80 dB RF signal-to-background ratio, see Figure 4-2(d), indicates excellent energy stability. Figure 4-2(e) shows the SSB phase noise of the fourth harmonic (1.963 GHz) of the laser. The timing jitter that is integrated from 10 MHz progressively down to 1 kHz is also shown. Over that full interval the net jitter is 20 fs. The phase noise below 1 kHz that follows a slope of -20 dBc/dec can be suppressed by controlling the fiber length with a piezo-based stretcher and locking the repetition rate to an electronic oscillator with better long-term stability. The bandwidth limitations of this approach will likely limit such suppression of phase noise to frequencies below 10 kHz. The measured phase noise is also compared to the quantum limit set by amplified spontaneous emission in the laser. The dashed-dotted line in Figure 4-2(e) shows the calculated quantum limit of the above laser [55]. The quantum-limited timing jitter in the frequency range [1 kHz, 10 MHz] is estimated to be 4 fs. The discrepancy by a factor of 5 may be easily explained by the uncertainty in the exact excess noise factor of the EDFA under saturated conditions, which we

n	1.475
$n_2 (\text{m}^2/\text{W})$	$3 \cdot 10^{-20}$
$A_{eff} (\mu\text{m}^2)$	70.9
$\beta_{2,EDF} (\text{fs}^2/\text{mm})$	-20
$\beta_{2,SBR} (\text{fs}^2)$	-735

Table 4.1: Laser parameters

Repetition rate (MHz)	491	
Intracavity pulse energy (pJ)	251	
Cavity losses (%)	20	
Pulse width (fs)	Measured	Simulated
	180	175
Optical spectrum FWHM (nm)	Measured	Simulated
	15.4	15.2

Table 4.2: Experimental and simulated results

estimated to be 10 and additional noise due to the intensity noise of the pump diode, which will need further investigations.

The experimentally observed pulse characteristics can be compared with theoretical predictions based on the area theorem by using our erbium doped fiber and SBR parameters. Table 4.1 summarizes the values used, while Table 4.2 compares the predicted and experimental laser characteristics.

Good agreement between the experimental and predicted values is obtained. Some discrepancy may be attributed to the non-uniform dispersion profile of the SBR, as its dispersion can change as much as 1000 fs^2 within the optical bandwidth of the laser output (Figure 4-1(b)).

The pulse duration of a soliton decreases with an increased pulse energy or a smaller ratio of dispersion to self phase modulation (SPM). For example, using an SBR with normal dispersion can decrease the total cavity dispersion without affecting the SPM coefficient and yield shorter pulses. The lower limit for the soliton pulse duration is set by available pump power, recovery time of SBR, gain bandwidth, and/or uniformity of gain spectrum over the signal wavelength.

The above results also testify to the scaling potential of such designs, provided that pumping is sufficient to ensure operation above the mode-locked Q-switching regime.

The scalability of this laser is further enhanced by using an anomalously dispersive gain medium, which eliminates the need for a passive, dispersion-compensating fiber section and allows maximizing the amount of gain with respect to the cavity length. For lower repetition rates, we demonstrated a 200 MHz laser based on the same configuration in [56]. At higher repetition rates, the dispersion of the SBR may eventually dominate over the dispersion of the gain fiber. In order to ensure soliton operation, one will have to either tailor the response of the SBR or force the lasing wavelength to coincide with the anomalously dispersive regime of the SBR.

4.2 Butt-coupling mechanism

For fundamentally mode-locked high-repetition-rate lasers, the cavity length needs to be as short as possible since the repetition rate is inversely proportional to the cavity length. As the cavity shrinks, the gain length also usually decreases and the threshold pump power for mode-locking increases. Because the available pump power is generally limited, the threshold pump power should be minimized to allow for a higher repetition rate. In order to minimize the threshold pump power, we can reduce the cavity loss such that the laser produces more signal power at a given pump power level. *Butt-coupling* of a fiber ferrule to a SBR or an output coupler would be one of the most effective ways to lower cavity loss, although the direct touching of SBR surface often leaves irreversible marks or scratches. In this section, the butt-coupling between a fiber ferrule and a flat optical sample is characterized: three different butt-coupling methods are discussed and the butt-coupling losses are measured. The force at the butt-coupling interface is also measured.

4.2.1 Mechanical setups - improving repeatability

Version 1

The first version of the butt-coupling device is shown in Figure 4-3. The mounts for the SBR (or output coupler) and the FC/PC fiber connector, Thorlabs HCS030 and
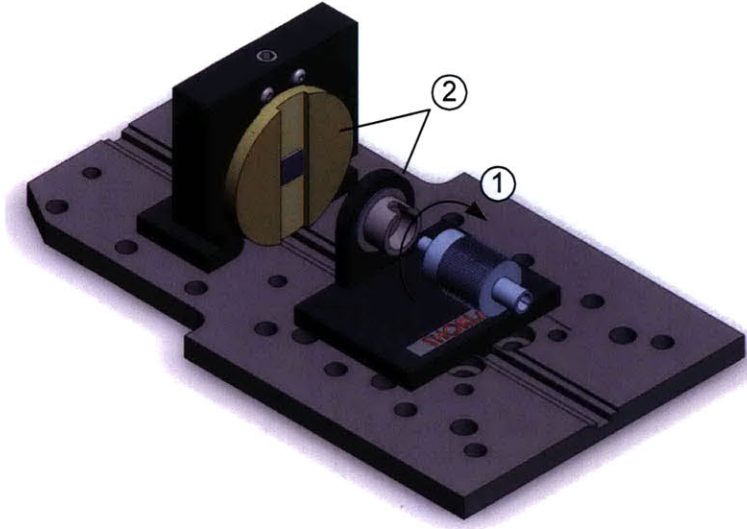
Figure 4-3: Butt-coupling scheme between FC/PC fiber connector and SBR (version 1). Numbers indicate the sequence of assembling.

HFB004 respectively, are placed on a Thorlabs AMA005 base plate. Both the SBR mount and the connector mount have alignment keys that fit into the slot of the base plate to assist alignment. Since the original connector mount does not allow the fiber ferrule tip to pass beyond the end surface at the SBR side, an additional machining is required.

There are two possible orders of the butt-coupling alignment.

1. The fiber connector is first screwed into the connector mount. The mounted SBR is fixed to the base plate with lock-down clamps. Then, the mount with the connector is brought to the SBR until they touch each other softly. After the butt-coupling is settled, the fiber connector mount is also fixed with the clamps, but very softly because the clamping action may change the butt-coupling loss.

2. The mounted SBR and the connector mount are clamped to the base plate with a appropriate distance, roughly less than 1 mm. Then, the fiber connector is softly screwed into the connector mount until the fiber ferrule touches the SBR surface. In the lab experiments, this order is preferred since no further clamping action is necessary and the butt-coupling quality can be maintained.
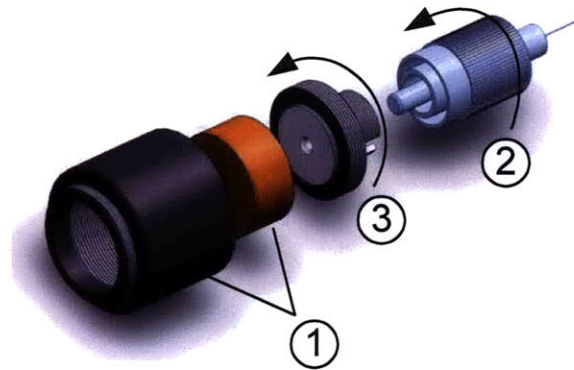
Figure 4-4: Butt-coupling scheme between FC/PC fiber connector and SBR (version 2). Numbers indicate the sequence of assembling.

Although this version that uses a AMA005 base plate version allows compatibility to other NanoMax® series, this butt-coupling mechanism is quite bulky and exposes the contact point to the air or dust collection. In addition, the butt-coupling loss is not very repeatable when the SBR is changed with a different one and re-mounted: sometimes only 60-70% of the best output power is obtained when used in a laser cavity.

The repeatability can be related to the number of elements between the fiber ferrule (or connector) and the SBR block. In this version, there are three elements - SBR block holder (HCS030), base plate (AMA050), and fiber connector mount (HFB004) with one-inch diameter SBR blocks. One more element, 1"-to-0.5" adaptor, should be added to hold half-inch-diameter SBR blocks, which results in four elements between the SBR mount and the fiber ferrule. In the next version, the number of elements are reduced to improve the repeatability of the butt-coupling action.

Version 2

Figure 4-4 illustrates a butt-coupling mechanism that uses fewer number of parts than in version 1. A ∅0.5" lens tube (Thorlabs SM05L05) with a length of 0.5" holds the reflector (SBR or output coupler) and the fiber connector adaptor (Thorlabs SM05FC) together. Thus, two elements, the lens tube and the fiber connector adaptor, guide a perpendicular contact between the SBR and the fiber ferrule.

100

The butt-coupling process starts with inserting the SBR mount block into the lens tube. The SBR mount block stops at the end of the tube before the external thread, precisely aligned with the optical axis. The fiber connector is screwed into the connector adaptor tightly. Then the connector adaptor assembled with the fiber connector is screwed into the lens tube until the fiber ferrule touches the SBR. The fiber adaptor should never be over-tightened to prevent any damage on the SBR.

During the action of screwing the fiber adaptor, there are two techniques to create the optimal butt-coupling. First, it is recommended that the lens tube is rotated with the fiber adaptor fixed, because rotating the connector adaptor or the fiber connector can twist the fiber itself, especially when the other end of fiber is already fixed for a butt-coupling to the output coupler. Second, the fiber adaptor is pulled away or pushed toward the SBR while rotating the lens tube, such that the thread of the connector adaptor evenly contacts with the thread of the lens tube. A full contact between those two threads will ensure that the fiber is parallel to the beam axis of the lens tube.

This version improved the repeatability such that the output power varied within 10% from the highest one for most of the butt-coupling attempts in a laser cavity. In addition, the SBR surface and the contact point are protected from the dust collection and the required setup is much more compact, rather like a little larger fiber connector.

Version 3

The version 3 mechanism, further improved from the version 2, is described in Figure 4-5. The butt-coupling process starts with inserting the SBR mount block into the lens tube, same as in version 2. Next, a $\varnothing0.5"$ retaining is tightly screwed in such that it secures the SBR mount block inside the lens tube. A customized ferrule holder for 2.5-mm ferrules is inserted, followed by another retaining ring. As the last step, the fiber ferrule only, without connector assembly, is inserted through the ferrule holder until the butt-coupling is made.

The customized ferrule holder is a $\varnothing0.5"$ aluminum cylinder with a 0.2" thickness
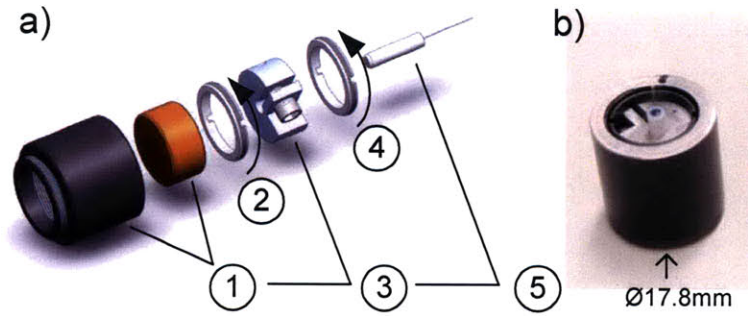
Figure 4-5: Butt-coupling scheme between FC/PC fiber connector and SBR (version 3). (a) model and (b) photo of the assembly. Numbers indicate the sequence of assembling.
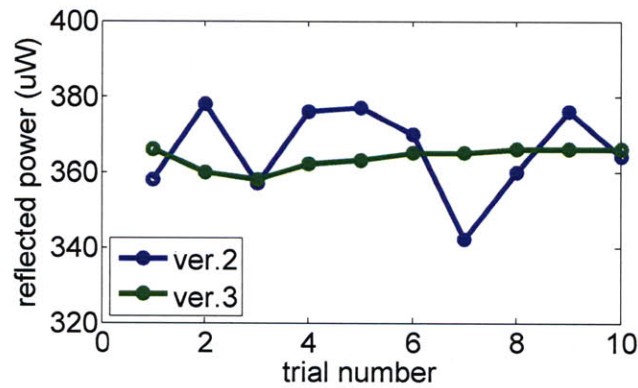
Figure 4-6: A comparison of repeatability between ver. 2 and ver. 3 butt-coupling.

and with a hole by a #40 drill bit. The original hole made with a #40 drill bit is slightly larger than 2.5-mm ceramic ferrules. One radius of the cylinder is cut by the bandsaw and clamped with a #2-56 screw to tighten the through-hole. With the screw adjustment, the through-hole is set for a snug fit to the ferrule. The hole is created at the center, but basically it can be anywhere inside the perimeter as long as the ferrule can touch the active area of a SBR.

Further improved repeatability of version 3 setup is presented in Figure 4-6. A light source at 1560 nm from a tunable laser source is injected into a circulator and propagated toward the contact between the fiber ferrule and a silver mirror (the same setup as in Figure 4-7(a)). Reflected powers are measured for several trials of the butt-coupling and plotted with horizontal axis of the trial number. The butt-coupling action is repeated 10 times over the same spot on the silver mirror for each version.

102
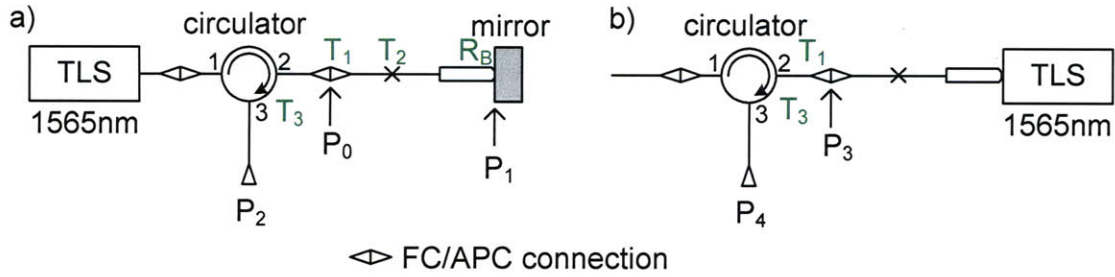
Figure 4-7: An experimental setup (a) to measure the loss of a butt-coupling between a PC-type ferrule and a flat mirror and (b) to measure the insertion loss of the circulator. TLS: tunable laser source.

The standard deviations of the output power are 11.7 μW and 2.9 μW respectively for version 2 and version 3, which corresponds to variation of 3.2% and 0.8% relative to the average. This result clearly indicates that the version 3 possesses much higher repeatability.

The version 3 mechanism provides the following advantages over the version 2:

1. Butt-coupling efficiency is more repeatable, as shown in Figure 4-6.

2. Softer touch is possible to the SBR or the output coupler because the ferrule is brought to the surface straight along the beam axis, rather than by twisting. This reduces the chances of damage by pressure. The butt-coupling speed is also enhanced.

3. A broader area of sample can be used for the butt-coupling. In version 2, the fiber ferrule contacts to a very limited area of the sample around the center. However, in version 3, the fiber ferrule can touch an arbitrary area of the SBR by appropriately placing the hole of the ferrule holder.

However, currently, a way to secure the ferrule to the ferrule holder needs to be devised and implemented. A stronger holding force than the friction between the ferrule and the custom ferrule holder is necessary for a stable butt-coupling.

103

4.2.2 Butt-coupling loss estimation

The butt-coupling loss or efficiency can be measured by using a setup shown in Figure 4-7. A light source is injected through port 1 of the circulator and the reflected power is measured through port 3. More power levels are also measured at various points from two different configurations to exclude the connector loss and the circulator insertion loss. The step-by-step measurement procedure follows below.

1. Configure the setup in Figure 4-7(a). The tunable laser source is connected to the circulator port 1 and the power level, P_0, is measured right after the circulator port 2.

2. A FC/PC fiber ferrule spliced to FC/APC connector is connected to the circulator port 2. The power level, P_1, is measured right after the FC/PC ferrule. Then we have

$$P_1 = P_0 T_1 T_2, \tag{4.1}$$

where T_1 is the transmission through the FC/APC connection and T_2 is the transmission through the splice between two SMF-28 fibers.

3. A silver mirror is butt-coupled by using one of the butt-coupling devices in section 4.2.1 and the power lever, P_2, is measured right after the circulator port 3.

$$P_2 = P_1 R_B T_2 T_1 T_3, \tag{4.2}$$

where R_B and T_3 are the butt-coupling efficiency and the transmission of the circulator from port 2 to port 3 respectively.

4. Configure the setup in Figure 4-7(b) to estimate T_3. Instead of the silver mirror, the tunable laser source is connected to the FC/PC ferrule. Note that the FC/PC ferrule in Figure 4-7(a) is identical to that in Figure 4-7(b). The power level, P_3, is measured after disconnecting the FC/APC connector from

104

the circulator. After re-connecting the FC/APC connector, the power level, P_4, is measured right after the circulator port 3.

$$P_4 = P_3 T_1 T_3, \tag{4.3}$$

5. From Equation 4.1,

$$T_1 = \frac{P_1}{P_0}\frac{1}{T_2} \simeq \frac{P_1}{P_0}, \tag{4.4}$$

since the splice loss is almost zero ($\sim$0.02 dB) and $T_2 \simeq 1$.

Using Equations 4.2 through 4.4,

$$
\begin{aligned}
R_B &= \frac{P_2}{P_1}\frac{1}{T_2 T_1}\frac{1}{T_3} \\
&= \frac{P_2}{P_1}\frac{\cancel{P_0}}{\cancel{P_1}}\frac{P_3}{P_4}\cancel{T_1} \\
&= \frac{P_2 P_3}{P_1 P_4}.
\end{aligned}
\tag{4.5}
$$

Note that P_0 is not necessary.

In the experiment, the tunable laser source emits 1565.000-nm light with a power level of $\sim$0.5 mW. Measured powers are P_0=427 μW, P_1=408 μW, P_2=345 μW, P_3=580 μW, and P_4=508 μW. Thus, $R_B = P_2 P_3/(P_1 P_4) = 0.965$ and we estimate that the butt-coupling loss is $\sim$3.5%. We note that this loss is much smaller when compared to using a pair of collimator and focusing lens to image the fiber core onto the SBR, which is usually at least 20%-30%.

The butt-coupling loss originates from the round shape of the end tip of the PC ferrule with a curvature radius of several tens of mm. The PC ferrule is intended for being mated with another PC ferrule, where two ferrule ends are deformed to be flat around the fiber by compressive force about a few N [57, 58]. Such strong compressive force is not expected in the butt-coupling in this thesis. More analysis of the compressive force under the soft touch follows in section 4.2.3.
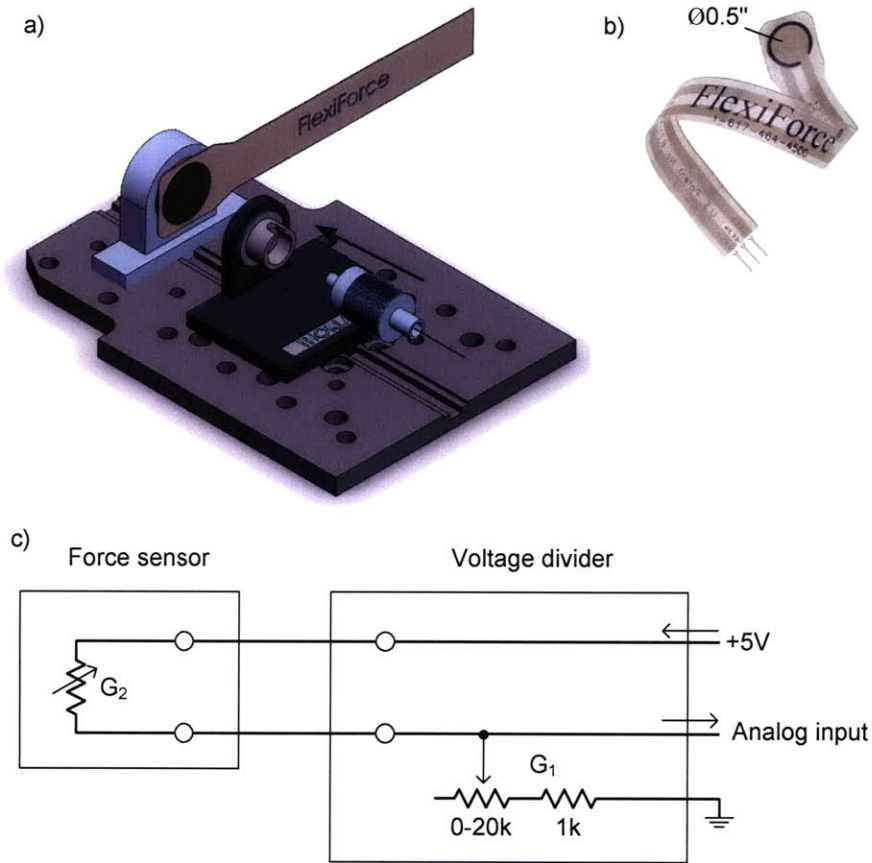
Figure 4-8: An experimental setup to measure the compressive force of a fiber ferrule. (a) Mechanical setup, (b) picture of a force sensor, and c) electric circuit diagram.

4.2.3 Butt-coupling force

Throughout the previous sections, we mention that the fiber ferrule should 'softly' touch the SBR not to damage it. The experiment in this section quantifies the relative compressive force of a soft touch, compared to the regular compressive force of FC connectors.

An experiment setup to measure the compressive force is described in Figure 4-8. The force is measured by using a flexible force sensor (FlexiForce A201 with 0-1 lb. range) that is attached with double-sided tape on a half-inch metal block. The metal block is held in a custom half-inch optics mount, which is secured on a base plate (Thorlabs AMA001). The fiber connector is mounted by using a commercial mount (Thorlabs HFB004), which is secured on the same base plate.

The conductance of the force sensor, G_2, is roughly proportional to the applied compressive force and we assume that the relationship between the conductance and the force is linear. The force sensor is connected to a voltage divider with +5V supply to convert the conductance change to a voltage change. The conductance in the voltage divider, G_1, can vary from 0.05 to 1 m℧(mili-mho).

The output voltage of the voltage divider is measured by using a digital multi-meter. Let V_r be the output voltage from the regular compressive force and G_{2r} be the corresponding conductance of the sensor. Similarly, let V_s and G_{2s} be the same quantities from the soft butt-coupling that was used in this thesis. The conductance of the voltage divider, G_1, is adjusted such that the output voltage stays near the half maximum or 2.5 V for a maximum sensitivity.

The measured V_r and V_s averaged out to 2.9 V and 1.1 V respectively, after several repetitions.

$$V_r = 5.0V \frac{G_{2r}}{G_1 + G_{2r}} = 2.9V \tag{4.6}$$

$$V_s = 5.0V \frac{G_{2s}}{G_1 + G_{2s}} = 1.1V \tag{4.7}$$

The ratio of G_{2s} to G_{2r} is calculated to be 0.2 by using Equations 4.6 and 4.7. The result indicates that the soft touch of the ferrule toward the SBR is about 20% of the full compressive force of regular FC-to-FC mating. The compressive force is measured only for the version 1 setup, since it is not straightforward to insert the force sensor into the lens tube in the version 2 or 3 setup.

The compressive force from a soft touch didn't present a problem for the long-term operation, although it usually left some marks on the samples. Further study is needed to lower the compressive force while maintaining a stable contact and to predict how the compressive force from the fiber ferrule affects the optical sample in physical contact.

4.3   1 GHz Er-doped fiber laser

This section demonstrates a compact, low jitter, femtosecond laser source at GHz-repetition rates. Fiber lasers with repetition rates up to 2 GHz were reported by McFerran *et al.* [59]. However, these lasers operated in a picosecond pulse regime and with an average output power of 1.3 mW. Recent experimental demonstrations of fiber lasers mode-locked with SBRs achieved repetition rates as high as 3 GHz [60], but with similarly low efficiency. With 700 mW of pump power only 2 mW of output power was measured. Additionally, thermal damage to the SBR was found to limit the long-term stability of the mode-locked laser output. When the gain fiber is butt-coupled to the SBR, the hot fiber core is in direct contact with the SBR and the SBR's surface experiences intense thermal heating. This can eventually result in failure of the laser after a short period of operation. Minimizing the thermal damage is therefore particularly important for high-repetition-rate fiber lasers to operate stably in long term.

As an extension of earlier work [24], we scale fundamentally mode-locked fiber lasers to GHz repetition rates [61]. The challenge of thermal damage is addressed and a stable, efficient, low-jitter fiber laser with a repetition rate of 1 GHz is demonstrated. With a natural recovery time of an InGaAs-based absorber in the SBR, a soliton laser source with sub-200 fs pulses is constructed. The laser is thermally stable and has a very compact packaged footprint of $121{\times}94{\times}33$ mm^3.

4.3.1   Experimental setup

The experimental laser setup of the erbium-doped fiber (EDF) laser is shown in Figure 4-9. Figure 4-9(a) outlines the laser schematic and illustrates the fiber assembly that separates the gain fiber from the SBR. The fiber section of the laser cavity consists of a 92-mm long Liekki Er80-8/125 erbium-doped gain fiber with anomalous dispersion of -20 fs^2/mm that was fusion spliced to an 11-mm long piece of standard single-mode fiber (SMF-28e). Both ends of the fiber assembly are polished flat and the gain fiber is secured with epoxy in a 126-μm ID zirconia ferrule. Since the splice joint between
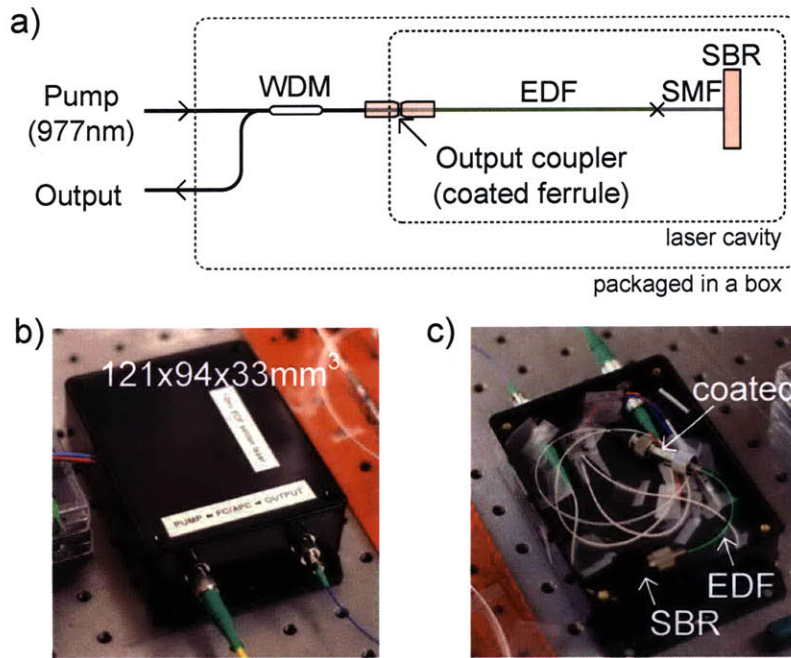
Figure 4-9: (a) Laser schematic, (b) photograph of the packaged laser and (c) photograph of the uncovered package. In (b), the blue and red wires on the left side of the box are used to measure the temperature inside the package.
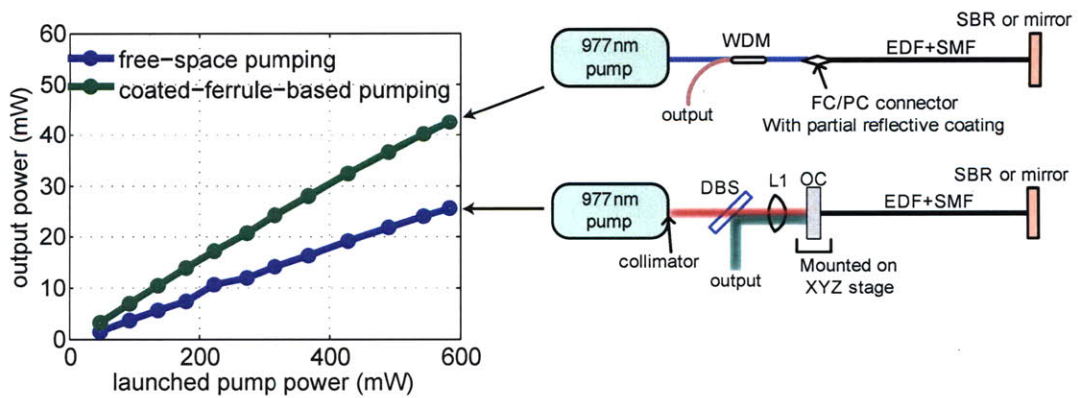
Figure 4-10: A comparison of CW-mode output power from laser cavities with different pumping scheme; free-space-based pumping and fiber-based pumping through a coated ferrule.

the gain fiber and the SMF is slightly thicker than the bare gain fiber end, the SMF is secured with epoxy in a 127-μm ID zirconia ferrule. The SMF section is shorter than the ferrule and hence the spliced section resides within the ferrule. A coated ferrule that is spliced to the wavelength division multiplexer (WDM), functions as output coupler with a ratio of 10% and is connected to the gain fiber ferrule in a mating sleeve. With such a design, a very robust and relatively low-loss connection is obtained compared to free space coupling of the pump into the gain fiber. A comparison of output power is shown in Figure 4-10 between the coupling through free space and fiber. In both cases, the same fiber cavity, 96-mm EDF spliced to 6-mm SMF, is butt-coupled to a silver mirror to operate the laser in CW mode. The output power from the laser that uses a fiber-based pumping is about 70% higher than that from the laser that is free-space pumped.

Figure 4-9(b) and (c) shows a photograph of the compact fiber laser system package with and without the cover respectively. The SBR is butt-coupled to the fiber ferrule by using version 2 assembly (section 4.2.1).

The SMF end of the fiber is butt-coupled to a III-V compound semiconductor SBR. The SBR is used to facilitate the mode-locking and self-starting of the laser: a schematic of the SBR is illustrated in Figure 4-11(a). The Bragg mirror, designed for a center wavelength of 1550 nm, consists of a 22-pair quarter-wave stack of $Al_{0.95}Ga_{0.05}As$ and GaAs. On the surface of the high reflectivity mirror, the $In_{0.53}Ga_{0.47}As$ absorber is embedded in a half-wave cladding layer of GaAs. To reduce absorption of the residual pump power and to further minimize localized heating effects, a pump-reflective coating (PRC), consisting of Ti_3O_5 and SiO_2 with quarter-wave layer thicknesses centered at the pump wavelength, was deposited on the surface of the SBR. With this added dielectric coating, any unabsorbed pump power is reflected back into the gain fiber and is efficiently reused.

As seen in Figure 4-11(b), the SBR exhibits a reflectivity of 95% at 1560 nm. The reflectivity is reduced to 88% after the deposition of the pump-reflective coating. Additionally, the added dielectric coating enhances the standing electric field at least by a factor of two, resulting in higher absorption losses and in a reduced saturation
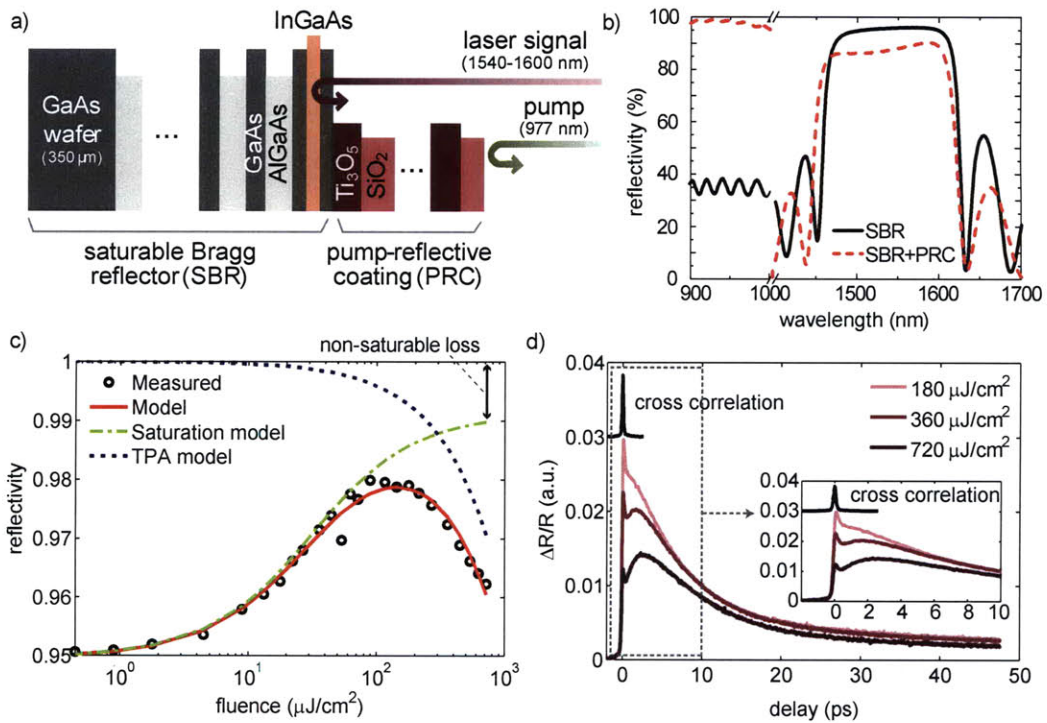
Figure 4-11: (a) Schematic diagram of the SBR, (b) measured low-fluence reflectivity of the SBR over 900 nm to 1700 nm with and without the additional pump-reflective coating (PRC), (c) measured reflectivity of the SBR for various fluences at 1560 nm and (d) pump-probe traces for three different fluences. TPA: two photon absorption, $\Delta R/R$: relative reflectivity change.

fluence. Figure 4-11(c) shows the measured reflectivity of the saturable absorber without the pump-reflective coating as a function of the pump fluence at 1560 nm. The solid line is the result of the fit of a slow saturable-absorber model plus two-photon-absorption model to the measured data. The data indicate that the SBR has a 4% saturable absorption, a 1% non-saturable loss and a saturation fluence of 11 μJ/cm^2. The pump-probe measurements for delays of up to 50 ps show that the overall recovery time of the SBR is 9 ps. The group delay dispersion of the SBR with the PRC at a wavelength of 1568 nm is approximately -1300 fs^2 when with the anomalous dispersive gain of the fiber permits operation in a net negative dispersion regime that allows soliton formation.

4.3.2 Mode-locking results

Figure 4-12 depicts the measured optical spectrum and interferometric autocorrelation trace (IAC) of the laser. The optical spectrum analyzer measurement shows a 17.5-nm FWHM optical bandwidth, implying a 150-fs transform-limited FWHM pulse duration, while the autocorrelation measurement yields a 187-fs FWHM pulse duration. The difference can be attributed to incomplete compensation of the chirp added by the Er-doped fiber amplifier that was connected to the laser output for amplification. The difference may also be caused by the non-uniform gain profile of the EDF and the non-uniform reflectivity profile of the SBR, causing a slight deviation of the measured optical spectrum from a sech^2 spectrum, as shown in Figure 4-12(a).

The optical spectrum is centered around 1573 nm, determined by the wavelength-dependent reflectivity of the SBR and the gain spectrum at the operating power level. The above values were obtained with 380 mW of pump power that was launched into the Er-fiber; the output signal power was measured to be 27.4 mW, which corresponds to 283-pJ of intracavity pulse energy. An estimated 185 mW of the launched pump power is absorbed in the EDF core. Separate experiments show that 30% of the launched pump power is absorbed in a single pass through the gain fiber and 90% of the remaining pump is reflected by the butt-coupled SBR. The GHz laser was self-starting; with increasing pump power, the laser first operated in a Q-switched
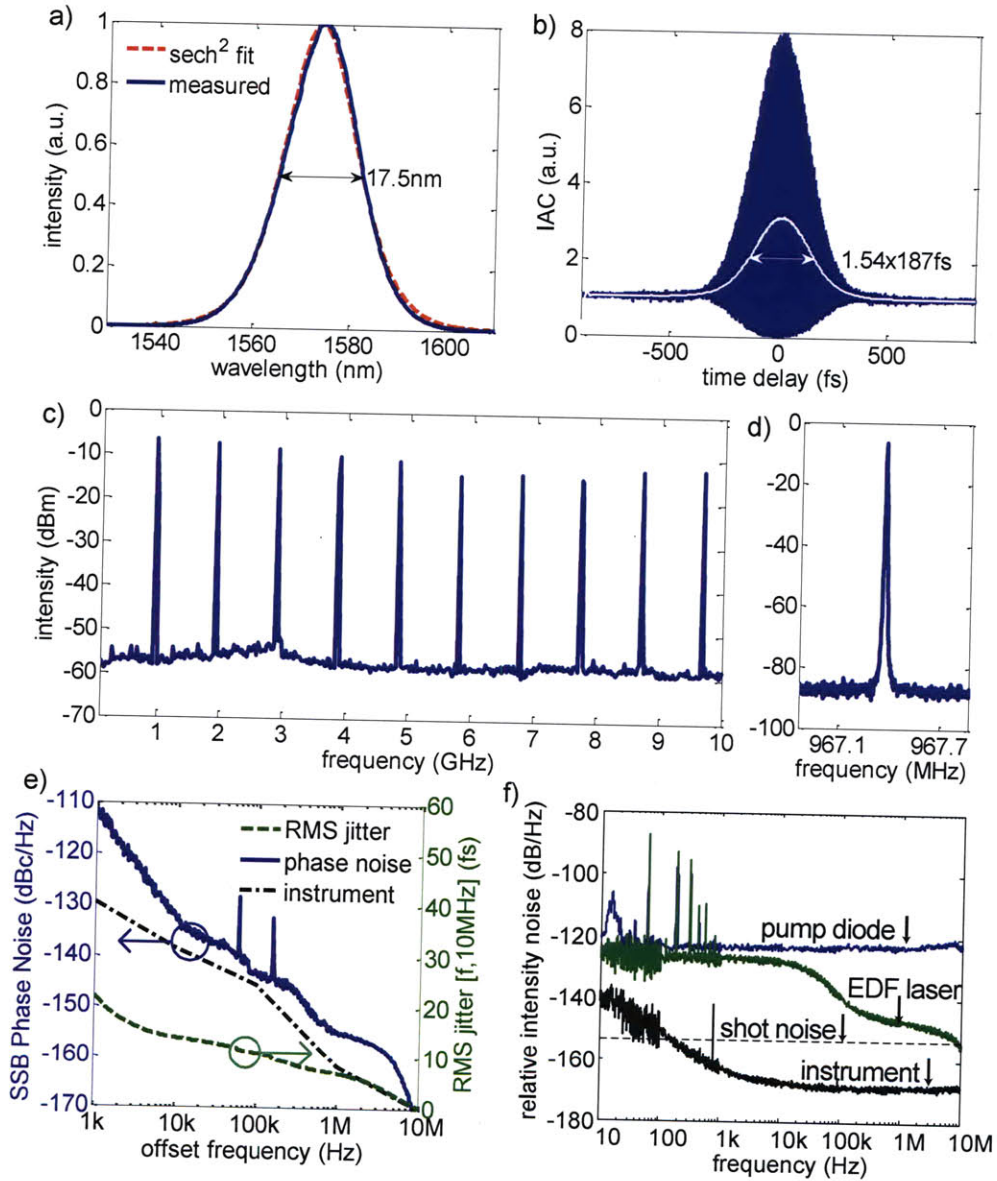
Figure 4-12: (a) Optical spectrum, (b) interferometric auto-correlation with inferred intensity autocorrelation (white), (c) RF spectrum span of 10 GHz with resolution of 3 MHz, (d) RF spectrum zoomed around the first harmonic with a resolution bandwidth of 300 Hz, (e) single side band (SSB) phase noise and instrument noise floor with integrated timing jitter, and (f) relative intensity noise (RIN) of mode-locked EDF laser, pump diode and instrument noise floor.

mode-locked state and then changed to a continuous-wave soliton mode-locked state at a pump power of 200 mW with a FWHM optical bandwidth of 9.0 nm. For a pump power greater than 382 mW, multiple pulsing occurred. The 80 dB RF signal-to-background ratio, as seen in Figure 4-12(d), indicates excellent energy stability. Figure 4-12(e) shows the single side band (SSB) phase noise of the first harmonic (967.3 MHz) of the laser. The laser output power is focused on a photodetector (EOTech ET-3500), filtered by a bandpass filter, and amplified to +16 dBm before being measured with the signal source analyzer (Agilent E5052). The timing jitter integrated from 10 MHz progressively down to 1 kHz is shown as a green dotted line, resulting in an integrated jitter of 22 fs over the entire interval. The phase noise below 10 kHz follows a slope of -20 dBc/dec and can be suppressed by controlling the fiber length with a piezo-based stretcher and locking the repetition rate to an electronic oscillator with better long-term stability. The bandwidth limitations of this approach will likely limit suppression of the phase noise to frequencies below ~10 kHz. The relative intensity noise (RIN) is measured to demonstrate the stability of the output intensity. The laser output is converted to an electrical signal by an amplified InGaAs photodetector (Thorlabs PDA400) with a trans-impedance gain of 7500 V/A. The split output power level of 0.53 mW generated a voltage of 3.54 V at the detector output with a 50 termination. The corresponding RIN of shot noise level, -153 dBc/Hz, exceeds the noise floor of the vector signal analyzer (HP 89410A) so that the measured noise is purely contributed by the laser output noise and not limited by the vector signal analyzer. The integrated relative intensity noise of 0.014 % from 10 Hz to 10 MHz mostly originates from the pump diode noise that is shown as the black curve in Figure 4-12(f). Note that the RIN of the laser is lower than that of the pump diode because the slope efficiency is reduced enough at the operation point due to gain saturation. A rapid drop of the laser RIN above 1 kHz is attributed to the long upper state lifetime of Er-ions. Both RINs of the pump diode and the laser show downward slopes near 7-8 MHz, which is consistent with detector 3-dB bandwidth of 10 MHz.
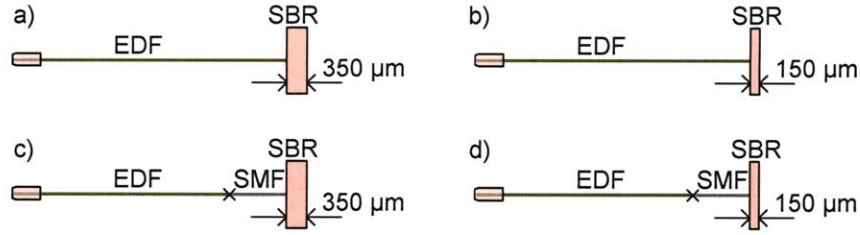
Figure 4-13: Four different configurations to study the thermal damage issue. EDF: Er-doped fiber, SBR: saturable Bragg reflector, and SMF: single mode fiber. All SBRs include the pump-reflective dielectric coatings deposited on the surface.

4.3.3 Thermal damage issue of SBR and long-term stability of laser

Increasing the pulse repetition rate of a soliton laser requires increasing pump so that the same pulse energy can be maintained for soliton formation [62]. Higher pump power leads to correspondingly more residual pump power at the other end of the fiber cavity and increased fiber core temperature. With the EDF in contact with the SBR, thermal damage was observed.

Four different configurations for the fiber cavity were evaluated to study the thermal damage issue (Figure 4-13) related to the SBR. The EDF and the SBR are in direct contact with each other in configurations (a) and (b), while single-mode passive fiber (SMF-28) is spliced to the EDF in configurations (c) and (d). The GaAs substrate of the SBR is 350-μmthick in configurations (a) and (c), while the substrate was lapped down to a final thickness of 150 μmin configurations (b) and (d) to improve heat sinking of the absorber layer. In all configurations, the total cavity length ranges from 100 mm to 105 mm, with a 5-6 mm long SMF section incorporated only for configurations (c) and (d). The mode-locking results described in section 4.3.2 were obtained by using the configuration shown in Figure 4-13(c) with a slightly longer length for the SMF section. Configuration (a) was tested first. For a launched pump power of 180 mW, soliton pulses were generated with an optical spectrum FWHM width of 5.4 nm and an average output power of 5.0 mW at a repetition rate of 975 MHz. However, after tens of seconds, the output power dropped to a few nW, with permanently damage observed to the SBR and fiber ferrule. We

115

assume that the hot fiber core may cause local deformation of the pump-reflective coating due to the different coefficients of thermal expansion between the dielectric coating and the underlying III-V compound semiconductor-based SBR. Following deformation of the coating the pump may no longer be fully reflected and subsequently results in damage to the SBR by the heat generated from the absorbed pump. Using an approach similar to the report by Li [63], the core temperature can be estimated. According to our estimates, 185 mW of pump light is absorbed from the launched pump power of 380 mW. Assuming that the pump is highly multi-mode and absorbed uniformly over the core, the equivalent absorbed pump power with a prorated core diameter is 185 mW $\times$ (20 μm/ 8 μm)^2 = 1.16 W. The equivalent launched pump power is thus about two times the absorbed pump power, or 2.32 W, which raises the temperature of the core 55°C above the ambient temperature. To prevent thermal damage, two protective mechanisms were implemented in configuration (d): (1) the SBR substrate was thinned down and (2) the passive single mode fiber was inserted between the EDF and the SBR. The SMF lowers the heat transfer from the EDF core to the SBR and the thinned-down substrate facilitates heat transfer from the surface of the SBR to the copper mount. Employing both protective mechanisms, the laser demonstrated stable generation of soliton-like pulses for a period of time exceeding three weeks. Comparison of configurations (b) and (c), indicates that incorporating additional SMF is more important than thinning the substrate of the SBR to prevent thermal damage as shown in Figure 4-14. Without adding the SMF, the output power continually drops to 70% of the starting power after 20 hours. In contrast, the SMF-buffered cavity maintains a constant output power with fluctuations of only a few percent, subsequently confirmed to be due to pump power fluctuations. The length of SMF used in configuration (c) was 6 mm.

The laser in section 4.3.2, base on configuration (c), was further investigated by using active feedback control of the output power to negate pump power fluctuations. Figure 4-15 shows the output power, the optical spectrum FWHM, the temperature inside the fiber package, and the repetition rate drift for 63 hours of operation. For a launched pump power of 270 mW, the output power is measured by using a power
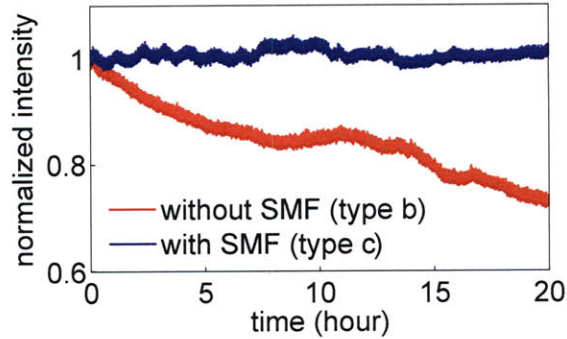
Figure 4-14: 20-hour measurement of the output power for two different fiber cavity configurations.

meter with analog output, which records at a sampling rate of 1 sample per second through a data acquisition card (National Instrument PCI-6013). The optical spectral width and the repetition rate are transferred from the instruments (ANDO AQ6317 and HP 8568B respectively) through GPIB interface every five seconds. For the active feedback, the analog output of the power meter is fed into the negative input of a loop filter box (New Focus LB1005) and the loop filter output modulates the current source of the pump diode.

Figure 4-15(a) shows the output power over a period longer than two days with fluctuations of only 0.5%. The temperature in the laser package is also logged and shows a temperature cycle of 1.5°C each day. The measurement started at 10 am, and the temperature rise and fall occurred during daytime, while the temperature remained constant overnight. The optical spectral width and the repetition rate indicate good laser stability, with variations only slightly affected by the ambient temperature change. These temperature-dependent variations can be further reduced by better temperature control of the package.

The temperature-dependent optical spectrum can be explained by the fiber birefringence that varies with the ambient temperature. A single mode fiber supports two orthogonal polarization modes. In a perfectly circular fiber, the two polarization modes are degenerate, but generally fibers have slightly elliptical cross-section and possess birefringence, allowing different polarization components to interact with each other through nonlinear polarization coupling [64]. Depending on the cavity parame-
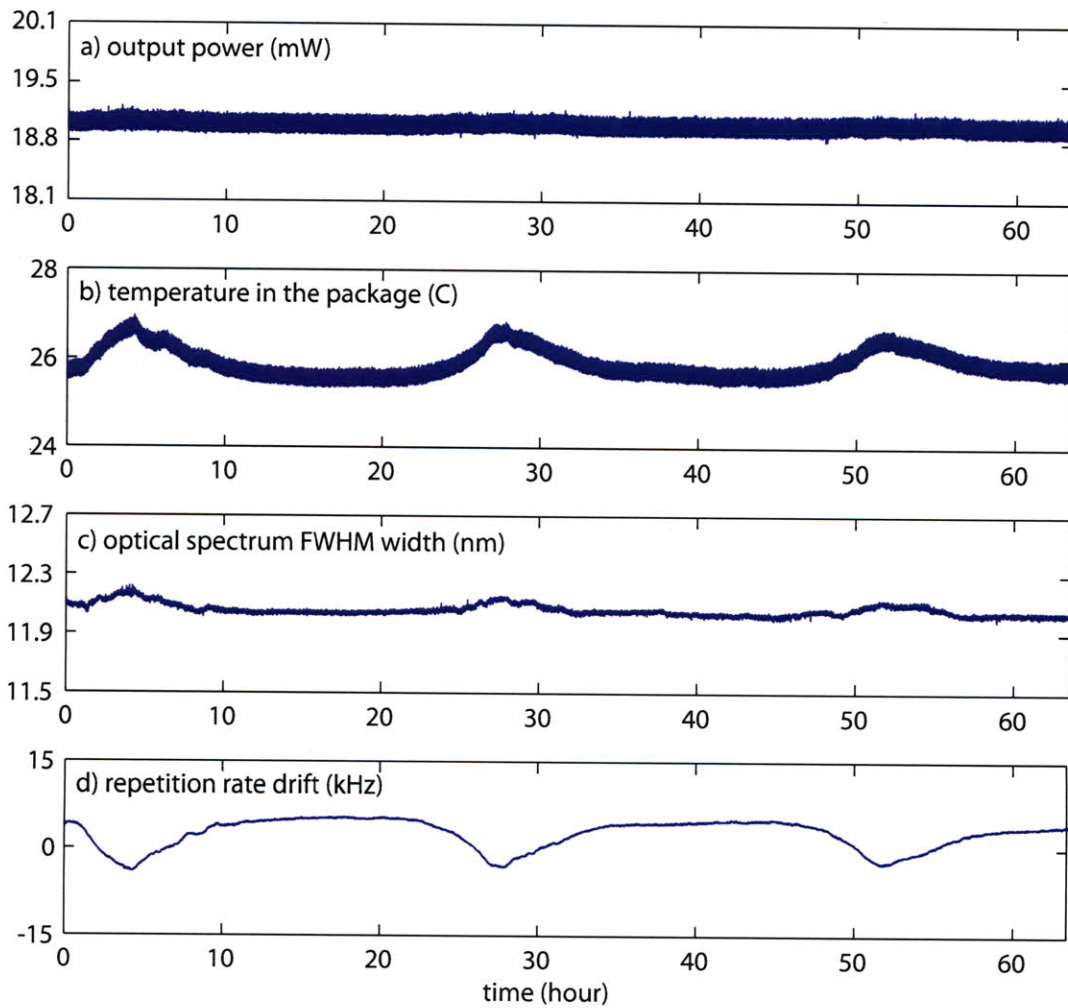
Figure 4-15: Long-term measurement of (a) output power, (b) temperature inside the package, (c) optical spectrum FWHM width, and (d) repetition rate drift from 967.398 MHz.
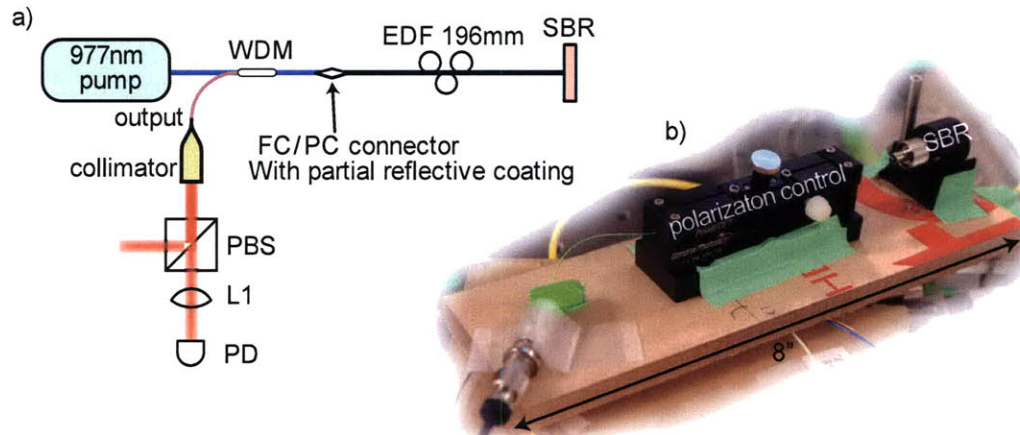
Figure 4-16: (a) Schematic and (b) photograph of the experimental setup for the polarization locking a 500 MHz Er-fiber laser.

ters including the fiber birefringence, the laser output polarization either evolves periodically or two polarization components are locked in phase to emit stable elliptically-polarized-solitons, called polarization-locked vector solitons (PLVS's) [8]. The polarization rotation can be eliminated by carefully aligning the fiber and operating the laser in the PLVS regime [65]. Whether the soliton is polarization-locked or not, the pulse energy changes with the fiber birefringence (Figure 2 in Akhmediev *et al.* [8]). The change of ambient temperature alters the birefringence of bent or twisted fibers [66] as noticed in our laser, and thus the pulse energy or the optical spectral width of the solitons.

The repetition rate drift of -7 ppm/°C, as shown above, originates mostly from the temperature-dependent refractive index of the fiber. A higher temperature increases the optical path length of the laser cavity and reduces the repetition rate accordingly. The corresponding change of the optical path length, here +7 ppm/°C, agrees well with the measured thermo-optic coefficients, dn/dT, of +8.5 ppm/°C for fused silica fiber (Table 6 in Leviton *et al.* [52]).

4.3.4 Polarization locking and vector solitons

The polarization rotation of the laser output can sometimes limit the system performance, especially when the system includes planar waveguide devices that are

119

sensitive to the polarization. The polarization locking is demonstrated in a 500-MHz Er-doped fiber laser with a setup described in Figure 4-16. Since the available polarization controller (Newport F-POL-IL) is not compact enough to fit in the 1-GHz laser cavity, a longer cavity is used. The laser configuration is similar to the 1-GHz laser except that the cavity is monolithically composed of an Er-doped fiber only. The laser output is connected to a RF spectrum analyzer through a polarizing beam splitter (PBS) to monitor the polarization rotation. An inline polarization controller is inserted into the cavity and adjusts the fiber polarization by twist and clamp.

The pump diode is driven with a current of 200 mA or a launched power of 75 mW. While adjusting the polarization controller, the RF spectrum and the optical spectrum are recorded, shown through (a) to (d) in Figure 4-17. From (a) to (b), the polarization evolution frequency (PEF), or how fast the polarization rotates, decreased from 70 MHz to 20 MHz. As the PEF approaches to zero, Q-switching instability appeared shortly in (c) before the polarization is locked in (d). Cundiff *et al.* [65] suggests that the Q-switching behavior can be due to the polarization hole burning, but it may need further investigation.

The sech^2-shape optical spectrum is imposed with some peaks on one of the wings due to the soliton perturbation from the polarization rotation in (a) and (b). Once the polarization is locked, the peaks are removed and the optical spectrum become broader, as shown in (d). These changes of the optical spectral width agree well with the theoretical study of Akhmediev *et al.* [8].

The polarization locking is quite sensitive to the fiber birefringence. Due to the air fluctuation and temperature change, the polarization locking lasted about three hours. Although a temperature-stabilized enclosure will extend the locked state, the fiber polarization needs to be dynamically controlled for continuous locking of the polarization rotation. The dynamic polarization control can be implemented by clamping action from piezo actuators and benefit shorter cavities since it can be constructed very compact.
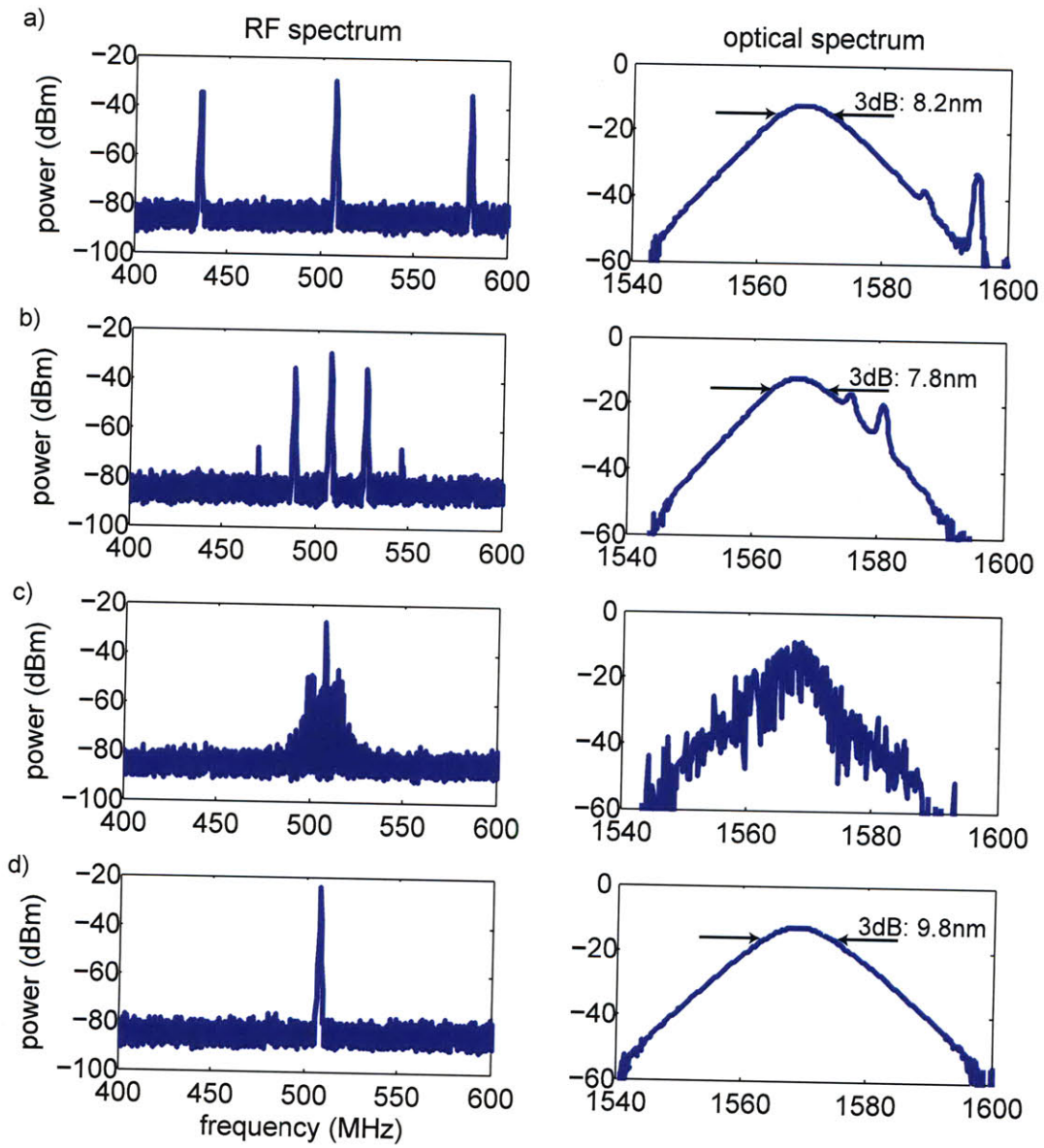
Figure 4-17: RF spectrum and optical spectrum for various positions of the polarization controller.
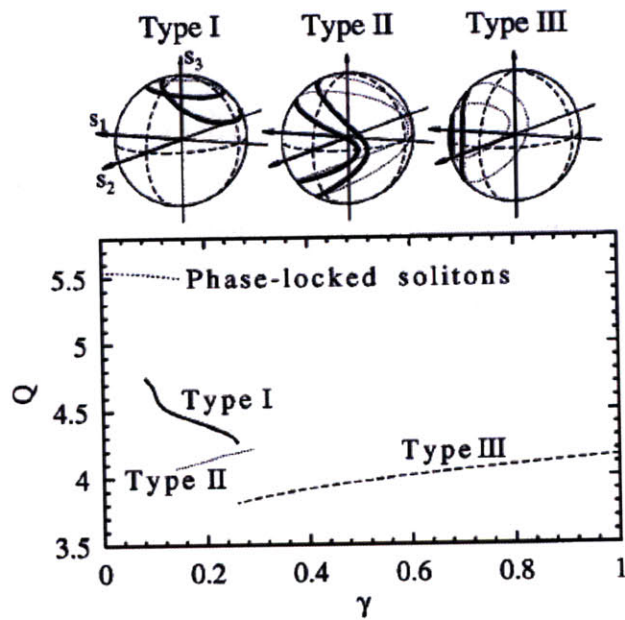
Figure 4-18: Pulse energy Q versus γ for four qualitatively different types of soliton. The two polarization components are phase locked in the interval $0 < \gamma < 0.16$ (upper dotted curve). The state of polarization is elliptical and can be represented by a dot on the Poincaré sphere that is close to the north or south pole. The periodic evolution of the state of polarization on the Poincaré sphere for other solutions is shown above each curve. In the case of the other three kinds of solution with lower values of Q, the state of polarization evolves periodically [8].
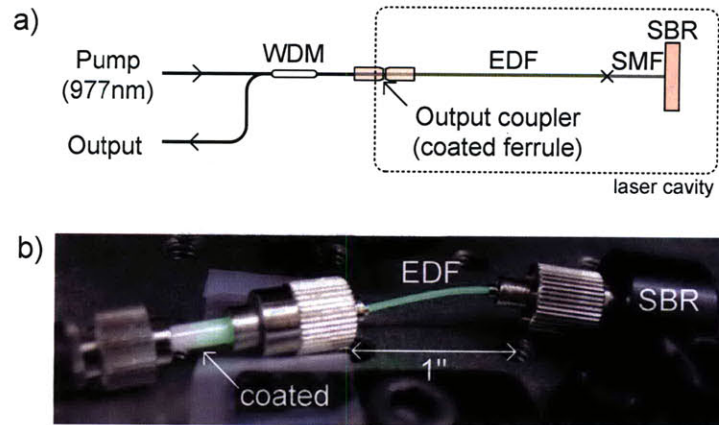
Figure 4-19: (a) Schematic and (b) photograph of the experimental setup for a 1.5-GHz Er-doped fiber laser.

4.4 Greather-than-1-GHz Er-doped fiber lasers

Once the 1-GHz Er-doped fiber laser produced stable solitons, higher repetition rates, 1.5 GHz and 2.0 GHz, were examined. Figure 4-19 shows the schematic and the photograph of the experimental setup for a 1.5-GHz Er-doped fiber laser. The laser setup contains the same configuration as in Section 4.3 except for a different fiber length. The total length of the fiber cavity is 67 mm including 6-mm SMF section on the SBR side. The SBR is the same SBR as in Section 4.3, but with the substrate thinned to 150 μm. The mode-locking results are shown in Figure 4-20. The FWHM optical spectral width is 8.2 nm and the repetition rate is 1.522 GHz. The laser operated longer than 60 hours without any power drop. The output power averaged 12.2 mW with pump current of 1400 mA and 600 mA from two polarization-combined pump diodes respectively.

A 2-GHz EDF laser was also attempted with 50-mm long fiber cavity including a 6-mm SMF section, but the SBR was damaged before starting any mode-locking. The exact reason for the failure is not fully understood yet and more trial may be necessary.

123
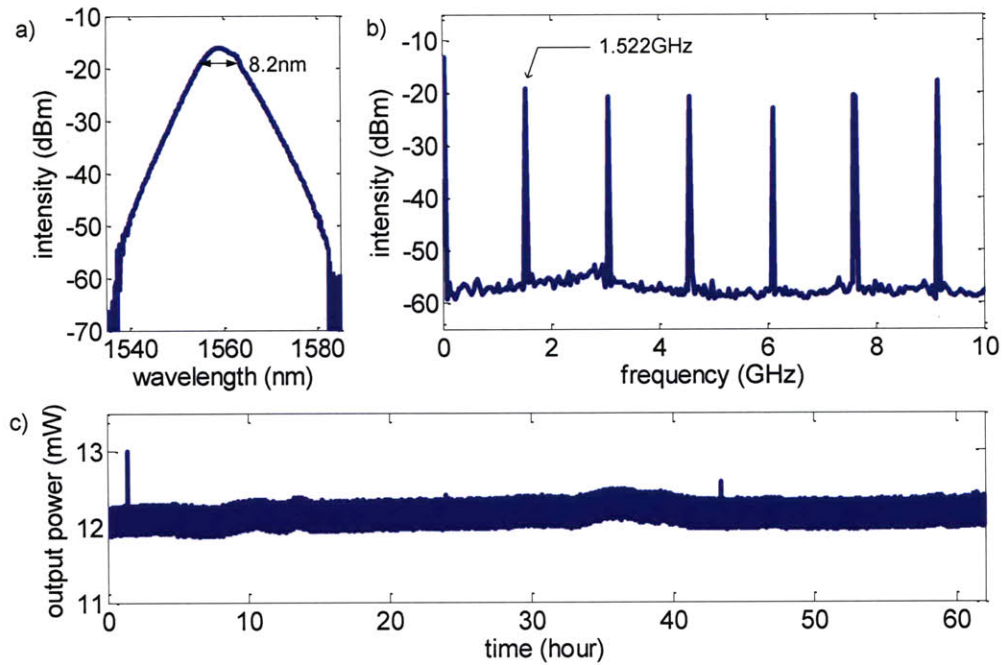
Figure 4-20: (a) Optical spectrum, (b) RF spectrum, and (c) long-term output power measurement from the 1.5-GHz Er-doped fiber laser.

4.5 Summary

This section summarized the research on compact femtosecond EDF lasers comprising anomalously dispersive EDF butt-coupled to an output coupler and a SBR respectively on each end.

The femtosecond EDF lasers were demonstrated with repetition rates from 500 MHz up to 1.5 GHz and with pulse durations as short as 180 fs. As the repetition rate reaches 1 GHz, the fiber cavity with homogeneous EDF suffered from the thermal damage on the butt-coupled SBR due to the hot EDF core. A passive fiber inserted between the SBR and the EDF solved the thermal damage issue, combined with pump-reflective coatings deposited on the SBR surface. Stable operation was demonstrated for the 1-GHz and 1.5-GHz EDF lasers for more than 60 hours.

The improvement of butt-coupling devices was described and the loss and the compressive force of the butt-coupling mechanism were also characterized. The butt-coupling loss was measured 3.5% between a FC/PC ferrule and a flat optical sample,

124

which is very low when compared to the typical round-trip loss of 20-30% from a pair of a collimator and a focusing lens.

The polarization rotation issue was raised in the later part of this chapter. A single mode fiber supports two orthogonal polarizations and the nonlinear interaction between the two polarization induces the polarization rotation. However, by controlling the birefringence of the fiber, the locking of the output polarization is possible and was demonstrated in a 500-MHz EDF laser.

4.6 Future work

4.6.1 Stabilization of the output polarization

The polarization locked vector solitons were demonstrated in the 500-MHz EDF laser. In order to obtain a locked polarization from the compact femtosecond fiber laser with a repetition rate > 1 GHz, a more compact polarization controller is required. The polarization controller in Figure 4-16 is considered to be the smallest one commercially available, but it is 78-mm long and cannot fit into current 1-GHz fiber lasers. A piezo actuator is a good candidate to implement such polarization controller and further to dynamically control the polarization against environmental perturbation. A systematic research is required to study how much a piezo actuator can change the polarization without breaking the fiber.

A different approach makes the fiber cavity highly birefringent by clamping most of the fiber section as hard as possible, such that only one polarization is supported [67].

4.6.2 Toward higher repetition rates

For higher repetition rates > 2 GHz, ErYb-codoped fiber is already under research [60]. The multi-GHz cavity, however, needs more study to solve the thermal damage issue. The dispersion of the fiber may need to be measured again with the updated dispersion measurement setup. The short fiber cavity also needs simulation consider-

125

ing the cavity dispersion and the SBR parameters, such as recovery time, saturation fluence, and modulation depth.

4.6.3 Toward lower timing jitter

The phase noise of the compact femtosecond fiber lasers (Figure 4-2 and 4-12), especially for offset frequencies smaller than several tens of kHz, could be further suppressed by using a feedback loop. The laser cavity length can be modulated by using a piezo actuator with both ends attached to the fiber. Further study is needed on how fast the fiber length can change by a piezo actuator. Additionally, we should consider how the piezo-based stretching can be combined with the polarization control.

In order to demonstrate the reduced phase noise of lower frequencies in short term, an external-cavity 400-MHz fiber laser can be built. The laser will incorporate the same schematic as in Figure 3-22 for capability of the repetition rate tuning, but a longer Er-fiber section is used. The fourth harmonic of the fundamental repetition rate can be locked to the FSR of the temperature-stabilized waveguide ring filter shown in Section 3.2.

Chapter 5

Dispersion measurement

In order to achieve soliton formation, appropriate amount of dispersion is required along the cavity. Thus, it is important to know the dispersion of each component in the laser cavity and to keep the cavity dispersion under control.

Among many ways to measure the dispersion, white-light interferometry is widely used for measuring the dispersion of optical materials. The interferometry method can provide high accuracy of measurement over relatively shorter samples. The interferometry uses a standard interferometer, such as a Mach-Zehnder or a Michelson interferometer. The Michelson one is chosen for a simpler setup.

In the white-light interferometry setup, a broad-band light source is split into two paths. One path is reflected by device under test (DUT) and the other path by a reference mirror. Then, the interference pattern generated from the two paths is monitored by a photodiode (spectrally integrated [1]) or an optical spectral analyzer (spectrally resolved [68]).

Both methods retrieve the phase response of the DUT to extract the dispersion coefficients. The spectrally integrated method calculates the phase response by performing a Fourier transform of the measured autocorrelation fringes in time domain, while the spectrally resolved method obtains the cosine of the phase response directly in the frequency domain.

The spectrally resolved approach can measure a larger range of dispersion than the spectrally integrated one, although the interference spectrum has to be separately
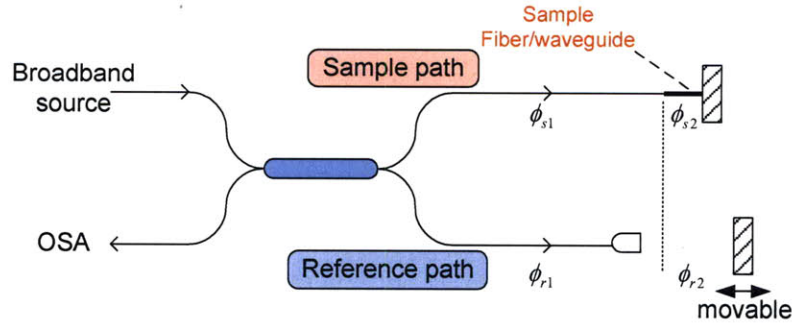
Figure 5-1: Schematic of the interferometric method to measure the dispersion

measured for every wavelength of interest. Wu *et al.* [68] deals with the spectrally resolved method with a broader view. This approach is applied to the dispersion measurement of waveguide-based samples, such as fibers or planar waveguides, with a dispersion larger than $\sim$1000 fs^2.

One advantage of the spectrally integrated interferometry is that the phase is evaluated for all frequency components simultaneously, which allows a faster measurement. In contrast to the spectrally resolved detection, the spectrally integrated method does not require a monochromator, thus, enabling a lower cost to build a setup. However, the measurable range of dispersion is limited by available scan length of either the reference mirror or the DUT and the range is generally much smaller than the spectrally resolved method. In addition, another interferometry may need to be added in order to compensate the nonlinear translation of one of the mirrors. This approach is applied to the dispersion measurement of thin-film-based samples or short waveguide-based samples with a dispersion less than $\sim$1000 fs^2.

5.1 Spectrally resolved interferometry

5.1.1 Theory

Figure 5-1 presents a simplified white-light interferometry setup. A broadband light source is divided into two paths, the sample path and the reference path respectively. Then, the reflected light from each path is combined into the other port of the 50:50

128

splitter. The reflected electric field from each path can be written as

$$E_s = e^{-j2(\phi_{s1}+\phi_{s2})}e^{j\omega t} \tag{5.1}$$

$$E_r = e^{-j2(\phi_{r1}+\phi_{r2})}e^{j\omega t}. \tag{5.2}$$

The measured spectral density at the optical spectrum analyzer (OSA) is

$$
\begin{aligned}
I &= |E_s + E_r|^2 \\
&= |E_s|^2 + |E_r|^2 + 2|E_s||E_r|\cos\phi(\omega) \\
&= I_r + I_s + 2\sqrt{I_r I_s}\cos\phi(\omega),
\end{aligned} \tag{5.3}
$$

where

$$\phi(\omega) = 2\left\{(\phi_{s1} - \phi_{r1}) + (\phi_{s2} - \phi_{r2})\right\}. \tag{5.4}$$

ϕ_{s1} is the phase change through the sample path without a DUT and ϕ_{r1} is the phase change in the reference path corresponding to the optical length of the sample path without a DUT. ϕ_{s2} is the phase change through a DUT and ϕ_{r2} is the phase change over the same optical length in the reference path. ϕ_{r2} changes along only free space. Each phase change can be expanded about a center frequency ω_0.

$$\phi_{s1} = \phi_{0,s1} + \frac{\partial\phi_{s1}}{\partial\omega}|_{\omega_0}(\omega - \omega_0) + \frac{1}{2}\frac{\partial^2\phi_{s1}}{\partial\omega^2}|_{\omega_0}(\omega - \omega_0)^2 + \cdots \tag{5.5}$$

$$\phi_{r1} = \phi_{0,r1} + \frac{\partial\phi_{r1}}{\partial\omega}|_{\omega_0}(\omega - \omega_0) + \frac{1}{2}\frac{\partial^2\phi_{r1}}{\partial\omega^2}|_{\omega_0}(\omega - \omega_0)^2 + \cdots \tag{5.6}$$

$$\phi_{s2} = \phi_{0,s2} + \frac{\partial\phi_{s2}}{\partial\omega}|_{\omega_0}(\omega - \omega_0) + \frac{1}{2}\frac{\partial^2\phi_{s2}}{\partial\omega^2}|_{\omega_0}(\omega - \omega_0)^2 + \cdots \tag{5.7}$$

$$\phi_{r2} = \frac{\omega}{c}d = \frac{\omega_0}{c}d + \frac{d}{c}(\omega - \omega_0) \tag{5.8}$$

Plugging Equations 5.5-5.8 into Equation 5.4, we obtain

129

$$\phi(\omega) = 2\left\{(\phi_{0,s1} - \phi_{0,r1}) + (T_{g,s1} - T_{g,r1})(\omega - \omega_0) + (\beta_{2,s1} - \beta_{2,r1})(\omega - \omega_0)^2 + \cdots\right\}$$
$$+2\left\{\left(\phi_{0,s2} - \frac{\omega_0}{c}d\right) + \left(T_{g,s2} - \frac{d}{c}\right)(\omega - \omega_0) + \beta_{2,s2}(\omega - \omega_0)^2 + \cdots\right\}(5.9)$$

$T_{g,s1} = \frac{\partial\phi_{s1}}{\partial\omega}|_{\omega_0}$, $T_{g,r1} = \frac{\partial\phi_{r1}}{\partial\omega}|_{\omega_0}$, and $T_{g,s2} = \frac{\partial\phi_{s2}}{\partial\omega}|_{\omega_0}$ are the group delay over the phase change of ϕ_{s1}, ϕ_{r1}, and ϕ_{s2} respectively. $\beta_{2,s1} = \frac{\partial^2\phi_{s1}}{\partial\omega^2}|_{\omega_0}$, $\beta_{2,r1} = \frac{\partial^2\phi_{r1}}{\partial\omega^2}|_{\omega_0}$, and $\beta_{2,s2} = \frac{\partial^2\phi_{s2}}{\partial\omega^2}|_{\omega_0}$ are the group delay dispersion over the phase change of ϕ_{s1}, ϕ_{r1}, and ϕ_{s2} respectively.

In order to reduce the number of unknown variables, a calibration is performed without a DUT. In this case of a zero-length DUT, $\phi_{s2} = \phi_{r2} = 0$. We can also adjust the position of the silver mirror in the reference path such that $T_{g,s1} = T_{g,r1}$. Since the group delays are wavelength-dependent, the silver mirror position should change depending on at which wavelength the condition $T_{g,s1} = T_{g,r1}$ needs to be met.

For the calibration without a DUT, the phase is simplified as

$$\phi_{cal}(\omega) = 2\left\{(\phi_{0,s1} - \phi_{0,r1}) + \frac{1}{2}(\beta_{2,s1} - \beta_{2,r1})(\omega - \omega_0)^2 + \cdots\right\} \qquad (5.10)$$

$$\equiv \phi_{0,cal} + \frac{1}{2}\beta_{2,cal}(\omega - \omega_0)^2 + \cdots . \qquad (5.11)$$

The constant phase term $\phi_{0,cal}$ and the second order dispersion term $\beta_{2,cal}$ can be extracted by fitting the measured fringe pattern. Then, a similar process is performed with a DUT inserted to estimate $\phi_{0,DUT}$ and $\beta_{2,DUT}$ using

$$\phi_{DUT}(\omega) = \phi_{cal}(\omega) + 2\left\{\left(\phi_{0,s2} - \frac{\omega_0}{c}d\right) + \frac{1}{2}\beta_{2,s2}(\omega - \omega_0)^2 + \cdots\right\} \qquad (5.12)$$

$$\equiv \phi_{0,DUT} + \frac{1}{2}\beta_{2,DUT}(\omega - \omega_0)^2 + \cdots . \qquad (5.13)$$

In Equation 5.12, a matched group delay is assumed, or $T_{g,s1} + T_{g,s2} = T_{g,r1} + \frac{d}{c}$, eliminating the first-order term. Dividing $\beta_{2,DUT} - \beta_{2,cal}$ by the physical length of the
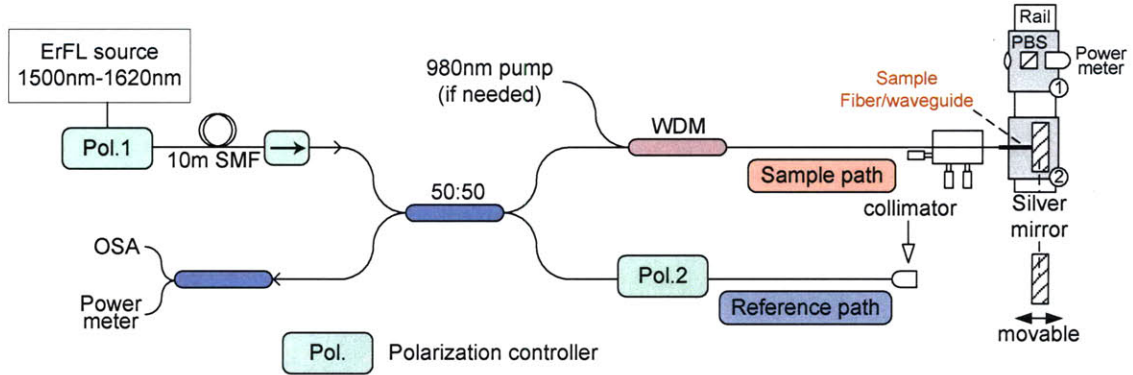
Figure 5-2: A setup to measure the dispersion of fiber or waveguide-based samples by using the spectrally resolved method.

DUT will provide us with the second order dispersion per unit length of the DUT. For higher order dispersions, corresponding terms can be added, such as $\frac{1}{6}\beta_{3,DUT}(\omega-\omega_0)^3$, into Equation 5.12.

5.1.2   Measurement setup

Shown in Figure 5-2 is the schematic of the setup to measure the dispersion with the spectrally resolved method. A mode-locked laser that uses the polarization additive pulse mode-locking (P-APM) method provides a white-light source. The laser spans from 1500 nm to 1620 nm and emits an output power of about 12 mW. The optical spectrum is shown in Figure 5-3. The laser output maintains a stable single polarization, which is an important characteristic to allow the dispersion measurement of polarization-sensitive samples, such as waveguides or polarization-maintaining fibers. A set of a quarter-wave plate and a half-wave plate (labeled as 'Pol.1' in Figure 5-2) follows the laser output to convert the output polarization to any arbitrary state [69], such that we control the polarization that enters the sample. The laser output pulses are chirped to more than 10-ps through the 10-m fiber to avoid any nonlinear effect due to the femtosecond pulse width. Without the chirp fiber, the optical spectral shape of the light reflected from a silver mirror in the sample path is noticeably different from that from the reference path. The chirped pulses pass through an iso-

131
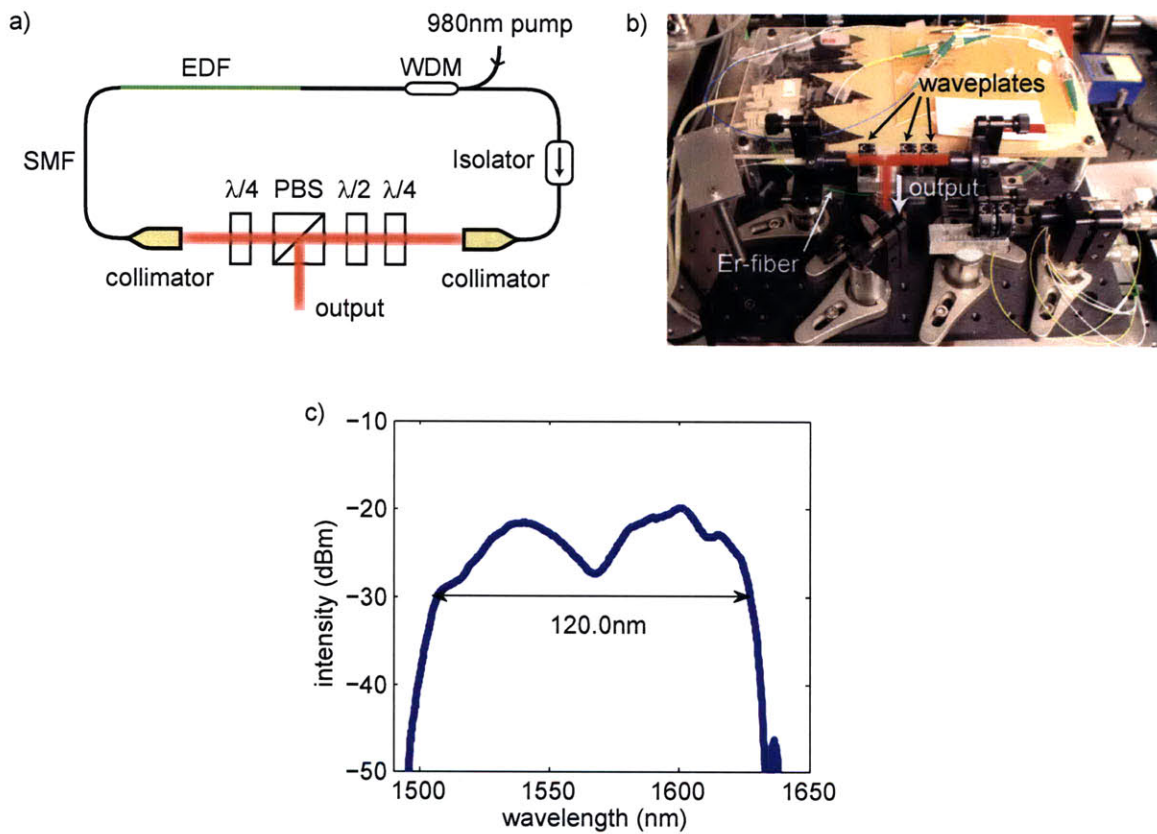
Figure 5-3: (a) Schematic, (b) setup picture and (c) optical spectrum of the mode-locked Er-doped fiber laser that is used for a broadband light source for the dispersion measurement.

lator to protect the laser source from back-reflections from the sample path and the reference path.

The isolator output is split into two paths through a 50:50 coupler - the sample path includes the device under test (DUT) and the reference path contains a silver mirror at the end. A wavelength division multiplexer (WDM) in the sample path can provide 980-nm pump to the sample, such as Er-doped fibers or waveguides. Another important function of WDM and its pigtailed fiber is to enlarge the dispersion difference between the two paths and provides more accurate measurements by using a larger number of fringes in a given wavelength range. The WDM uses Lucent 980 fiber with a dispersion of -7 fs^2/mm, while SMF28e fiber with a dispersion of -24 fs^2/mm is used all along the reference path about 3 meter long. More details are explained in Table 5.1.

Right before the DUT, a cleaved SMF-28 fiber is mounted on a XYZ-translation stage with sub-micron resolution. At the end of the sample path, two different setups sit on independent carriages on a rail. The carriage ② is the DUT butt-coupled to a silver mirror and used for dispersion measurement. The setup on the carriage ① enables measuring the polarization of the incoming whitelight source by using an aspheric lens, a polarizing beam splitter and a power meter. The waveplates near the laser output (labeled as 'Pol.1' in Figure 5-2) are adjusted so that a desirable polarization status is obtained. For more convenience, another silver mirror can be mounted on the carriage ① at an optimized position for silver mirror calibration, in such a way that the DUT can stay aligned with the silver mirror on the carriage ②.

The polarization controller in the reference path (labeled as 'Pol.2' in Figure 5-2) can adjust the polarization of the reference path such that the reflected light from each path has the same polarization and the fringe contrast is maximized. The combined reflected light from the 50:50 coupler is fed into the optical spectrum analyzer (OSA) and the power meter through a 90:10 coupler at the same time. The OSA samples the fringe pattern, while the power meter monitors the alignment of the DUT between the cleaved fiber and the silver mirror.

The distance between the collimator and the reference mirror is about 10-15 cm

	sample path			reference path		
	section	fiber type	length	section	fiber type	length
1	Coupler pigtail	SMF-28	300	Coupler pigtail	SMF-28	300
2	WDM pigtail	Lucent980	1080	Patchcord 1	SMF-28	1050
3	WDM body	Lucent980	60	Patchcord 2	SMF-28	1050
4	WDM pigtail	Lucent980	1080	Connector	SMF-28	225
5	Cleaved fiber	SMF28	>300	Collimator pigtail	HI1060	160
6	DUT		x	Free space		$> 2.3 + x \ n_{eff}$

Table 5.1: Details on each section of the reference path and the sample path for the dispersion measurement. Lengths are in mm. n_{eff} is the effective index of the DUT.

when the cleaved fiber in the sample path is directly butt-coupled to a silver mirror without any DUT. With a sample fiber or waveguide inserted, the length of the free-space section should increase by the optical path length of the sample. The length of the sample needs to be as large as possible to reduce measurement error per unit length, but practically the sample length is bounded by (1) available lab space for the reference path and (2) beam divergence from the collimator. The first reason is obvious since longer free space section takes up correspondingly larger space on the optical table. If the free-space section is too long compared to the working distance of the collimator, we may end up with too little optical power coupled back into the collimator. In this thesis, the optical length of the sample ranged from 10 cm to 50 cm.

Detailed description of the experiment setup is listed in Table 5.1. Each arm, the sample path or the reference path, is composed of about 2.5-m long fibers. The reference path fiber length is slightly shorter than the sample path, in order to allow a few cm of free-space section for the case of a zero-length DUT. The WDM in the sample path naturally gives enough difference ($\sim$90,000 fs^2 in this thesis) of dispersion between the two paths. With too small dispersion difference between two paths, it is difficult to fit the measured fringe, especially within a limited wavelength range of available light sources. Figure 5-4 simulates the normalized fringe pattern, $\cos(\phi(\omega))$, for three different β_2 values. 10,000 fs^2 produces only 3 periods of sinusoidal pattern and may reduces the accuracy of fitting. 80,000 fs^2 can generate almost 30 periods that can allow reasonable accuracy. A higher dispersion difference gives an even
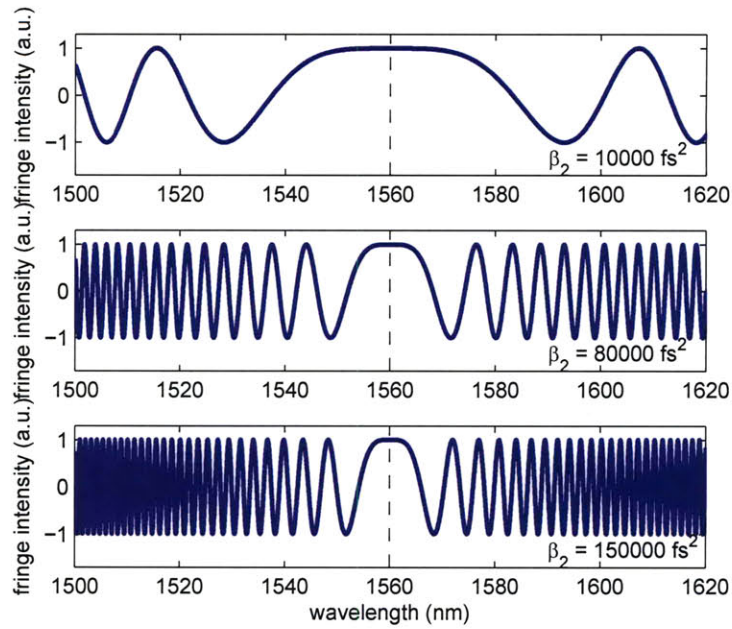
Figure 5-4: Fringe patterns for various β_2 values.

larger number of periods, while the dispersion difference is bounded by the resolution of OSA.

5.1.3 Measurement procedure

The dispersion of a sample is measured through the following steps.

1. Polarization adjustment (only for a polarization-sensitive measurement)

   The waveplates following the source laser are adjusted such that we obtain desired polarization state at the end of cleaved fiber in the sample path. For this purpose, the carriage ① with a PBS and a power meter can be used. To obtain a TE polarization, the waveplates are rotated such that the transmitted power is maximized through the PBS. Similarly, a maximum reflected power ensures a TM polarization.

2. Silver mirror alignment

   The cleaved fiber in the sample path is butt-coupled to a silver mirror on either

135

the carriage ① or ②. The alignment can be optimized by monitoring the power meter across the coupler. A small amount of index fluid, such as glycerin, can improve the alignment quality.

3. Baseline measurement

The intensity I_s and I_r in Equation 5.3 are measured such that the fringe pattern can be normalized as

$$\cos\left(\phi(\omega)\right) = \frac{I - I_s - I_r}{2\sqrt{I_s I_r}}. \tag{5.14}$$

The sample path intensity I_s is measured by physically blocking the reference path with a paper, between the collimator and the silver mirror. The measurement of the reference path intensity I_r requires to disconnect one of the fiber connectors in the sample path since the sample path does not contain any free-space section. After measuring I_r, enough care is needed to ensure the fiber connection is fully recovered by monitoring the power meter. Cleaning the fiber ferrule surface is strongly recommended after several times of re-connection.

4. Silver mirror calibration

As mentioned in Section 5.1.1, the dispersion of the experiment setup needs to be measured without a DUT, in order to calibrate the dispersion measured with a DUT inserted. The polarization controller (Pol. 2) in the reference path is adjusted such that the fringe pattern on the OSA has a maximum contrast between extrema, or, in other words, such that the polarization of the reflected light from each path coincides.

> □ Determination of the dispersion sign
>
> The sign of the dispersion can be determined by tuning the translation stage for the air path mirror. If the length of the air path increases and the interference pattern shifts to a shorter wavelength, the sample fiber is exhibiting normal dispersion in this wavelength range.

136
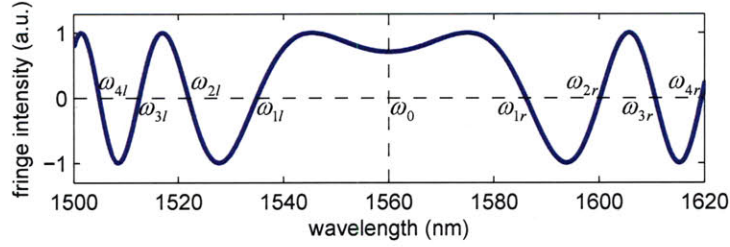
Figure 5-5: Fringe pattern for $\beta_2 = 13000\text{fs}^2$ with each zero-crossing frequencies labeled.

5. DUT measurement

The DUT is aligned with the cleaved fiber and the dispersion is measured. The baseline alignment must be performed again for this DUT measurement, since the DUT changes the reflected power both from the sample path and from the reference path.

5.1.4 Data processing

After we obtain the fringe pattern according to above-mentioned procedure, dispersion values are estimated by using the following algorithm.

1. Normalize

The acquired fringe pattern is normalized as described in Equation 5.14 by using the measured intensity profile I_s and I_r from the sample path and the reference path respectively.

2. Find zero-crossing frequencies

The zero-crossings of the normalized fringe pattern, $\cos(\phi(\omega))$, are used to construct a fitting to Equation 5.10 or 5.12. For more accurate calculation of zero-crossings, each segment of the fringe is fit to a cubic polynomial. Then, the zero-crossings of the piecewise cubic polynomials are calculated. The zero-crossings in the longer-wavelength direction from the center frequency ω_0 are labeled as $\omega_{1r}, \omega_{2r}, \cdots, \omega_{mr}$ with an order of increasing difference from ω_0.

137
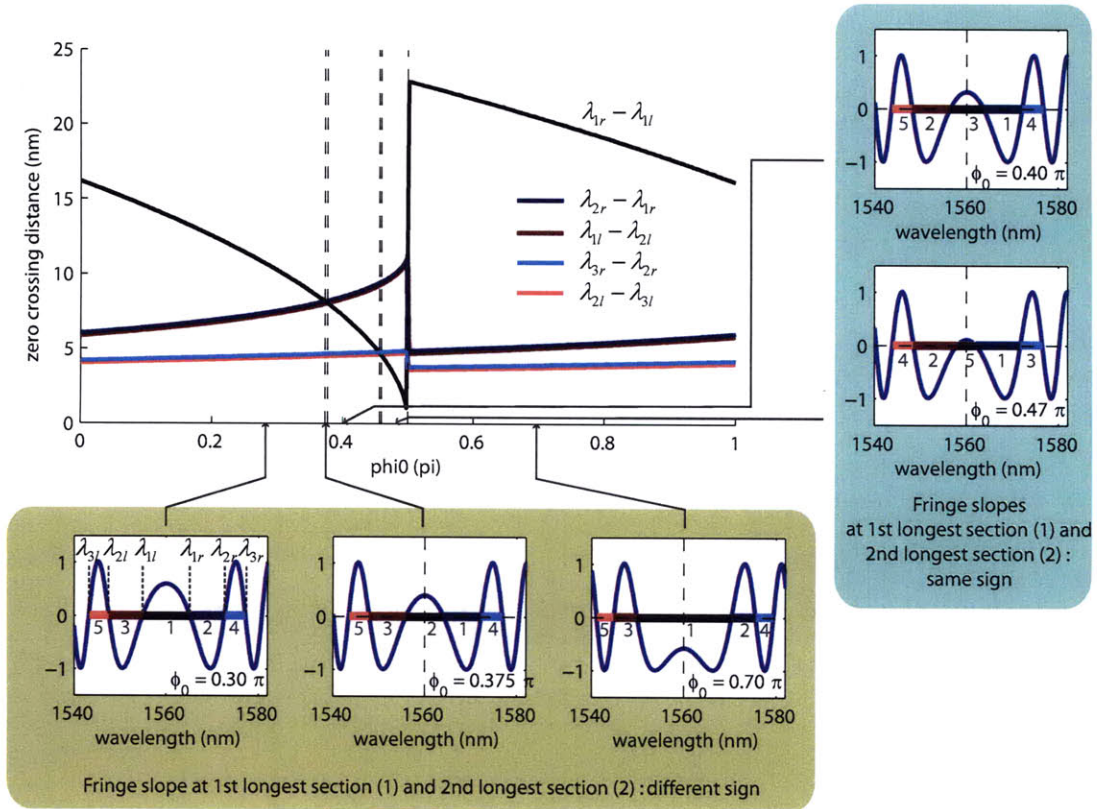
Figure 5-6: Distances between consecutive zero crossings for various ϕ_0 values. β_2=80,000 fs^2 was used. Depending on ϕ_0 values, different methods are used to estimate the center wavelength.

Similarly, the shorter-wavelength zero-crossings are labeled as ω_{1l}, ω_{2l}, $\cdots$, ω_{nl} (see Figure 5-5).

3. Estimate center wavelength

Knowing the center wavelength can significantly simplify the estimation of dispersion coefficients. It is important to estimate the center wavelength as accurately as possible since the estimated dispersion is sensitively affected by the accuracy of the center wavelength.

Here, we define

$$\lambda_x \equiv \frac{2\pi c}{\omega_x}, \tag{5.15}$$

where $x = mr$, $(m-1)r$, $\cdots$, $1r$, 0, $1l$, $\cdots$, $(n-1)l$, nl.

138

The center wavelength of the fringe pattern can be found by identifying λ_{1l} and λ_{1r}, which requires a different calculation scheme for different ϕ_0 (constant phase term). Figure 5-6 illustrates how to determine which zero-crossing frequencies correspond to λ_{1l} and λ_{1r} respectively. The larger graph shows the distance between two consecutive zero-crossing wavelengths along $\phi_0{=}0$ through π for six zero-crossings around the center wavelength, thus, including five curves. For example, the black curve indicates the distance between the first zero-crossing wavelength left from the center and the first zero-crossing wavelength right from the center.

Depending on ϕ_0, the magnitude relation of five curves varies. For example, the black curve ($\lambda_{1r} - \lambda_{1l}$) has a larger zero-crossing distance than the dark blue curve ($\lambda_{2r} - \lambda_{1r}$) only for $0 < \phi_0 < 0.373\pi$ and $0.5\pi < \phi_0 < \pi$. The magnitude relation is divided into six regions along $0 < \phi < \pi$. The graph shows the curves for $0 < \phi_0 < \pi$, but they repeat themselves also for $\pi < \phi_0 < 2\pi$ since the fringes are only inverted around the wavelength axis and the zero-crossing position does not change $(\cos(\theta + \pi) = -\cos(\theta))$.

The smaller graphs at lower and right part of Figure 2-5 plot the fringe patterns for five different ϕ_0 values, each of which has a different magnitude relation among the five zero-crossing distances. The sorted order (1 to 5) of the five zero-crossing distances is indicated with gray numbers in each fringe graph. The five fringe patterns are categorized into two types: 1) the three fringes in the dark yellow shade have *different* signs of slope at the left zero-crossing in the interval of the largest zero-crossing distance (λ_{1l} for $\phi_0 = 0.30\pi$ and λ_{1r} for $\phi_0 = 0.47\pi$) and at the left zero-crossing (λ_{1r} for $\phi_0 = 0.30\pi$ and λ_{2r} for $\phi_0 = 0.47\pi$) in the interval of the second largest zero-crossing distance respectively, 2) while the two fringes in the blue shade have the *same* signs of slope.

(a) Different signs of slope

This case occurs for $0 < \phi_0 < 0.373\pi$ and $0.5\pi < \phi_0 < \pi$. Three largest zero-crossing distances labeled as 1, 2 and 3, are always forming a con-

tinuous line. From the three, the middle section is chosen and the center wavelength is calculated by an arithmetic average of the left zero-crossing and the right zero-crossing of that middle section.

(b) Same signs of slope

This case occurs for $0.373\pi < \phi_0 < 0.5\pi$. The center wavelength is calculate by an arithmetic average of the right zero-crossing of the second largest zero-crossing distance section (labeled as '2' along the wavelength axis) and the left zero-crossing of the largest zero-crossing distance section (labeled as '1' along the wavelength axis).

4. Estimate dispersion coefficients by using the least-mean-square method

The dispersion coefficients are estimated by using the fact that there is phase difference of π between two consecutive zero-crossings in the normalized fringe pattern. An example of estimating up to third order dispersion is shown in the following.

$$\left(\tfrac{1}{2}\beta_2\Omega_{1l}^2 + \tfrac{1}{6}\beta_3\Omega_{1l}^3\right) - \left(\tfrac{1}{2}\beta_2\Omega_{2l}^2 + \tfrac{1}{6}\beta_3\Omega_{2l}^3\right) \quad = \quad \pi$$

$$\vdots \qquad\qquad \vdots$$

$$\left(\tfrac{1}{2}\beta_2\Omega_{(n-1)l}^2 + \tfrac{1}{6}\beta_3\Omega_{(n-1)l}^3\right) - \left(\tfrac{1}{2}\beta_2\Omega_{nl}^2 + \tfrac{1}{6}\beta_3\Omega_{nl}^3\right) \quad = \quad \pi$$

$$\left(\tfrac{1}{2}\beta_2\Omega_{1r}^2 + \tfrac{1}{6}\beta_3\Omega_{1r}^3\right) - \left(\tfrac{1}{2}\beta_2\Omega_{2r}^2 + \tfrac{1}{6}\beta_3\Omega_{2r}^3\right) \quad = \quad \pi$$

$$\vdots \qquad\qquad \vdots$$

$$\left(\tfrac{1}{2}\beta_2\Omega_{(m-1)r}^2 + \tfrac{1}{6}\beta_3\Omega_{(m-1)r}^3\right) - \left\{\tfrac{1}{2}\beta_2\Omega_{mr}^2 + \tfrac{1}{6}\beta_3\Omega_{mr}^3\right) \quad = \quad \pi$$

$\Omega_x = \omega_x - \omega_0$ is the frequency difference between each zero-crossing and the center frequency. The above equation array can be represented in a matrix form

of $Ax = b$, where

$$A = \begin{bmatrix} \Omega_{1l}^2/2 - \Omega_{2l}^2/2 & \Omega_{1l}^3/6 - \Omega_{2l}^3/6 \\ \vdots & \vdots \\ \Omega_{(n-1)l}^2/2 - \Omega_{nl}^2/2 & \Omega_{(n-1)l}^3/6 - \Omega_{nl}^3/6 \\ \Omega_{1r}^2/2 - \Omega_{2r}^2/2 & \Omega_{1r}^3/6 - \Omega_{2r}^3/6 \\ \vdots & \vdots \\ \Omega_{(m-1)r}^2/2 - \Omega_{mr}^2/2 & \Omega_{(m-1)r}^3/6 - \Omega_{mr}^3/6 \end{bmatrix},$$

$$x = \begin{bmatrix} \beta_2 \\ \beta_3 \end{bmatrix} \text{ and } b = \begin{bmatrix} \pi \\ \vdots \\ \pi \\ \pi \\ \vdots \\ \pi \end{bmatrix}.$$

The dimension of A, x, and b is $(n + m - 2) \times 2$, 2×1, and $(n + m - 2) \times 1$ respectively. Then, the vector x can be solved by $x = \left(A^T A\right)^{-1} A^T b$.

5. Estimate ϕ_0 (optional)

The constant phase term ϕ_0 can also be estimated. Figure 5-7 illustrates normalized fringe patterns for various ϕ_0 values from 0 to 2π. It is possible to estimate ϕ_0 through (1) the fringe value at the center wavelength and (2) the direction of curvature (convex or concave). However, since at this stage ϕ_0 is the only unknown, a brute-force search of optimal ϕ_0 can be quickly performed to find the maximum-likelihood value.

5.1.5 Guide to MATLAB GUIs

Shown in this section is an example of dispersion measurement procedure that uses the custom-made Matlab GUIs (Graphic User Interfaces). The dispersion of a 40-mm Er-doped waveguide in Section 3.1 is measured. The alignment setup in the sample path around the waveguide chip is shown in Figure 5-8. The waveguide chip is first
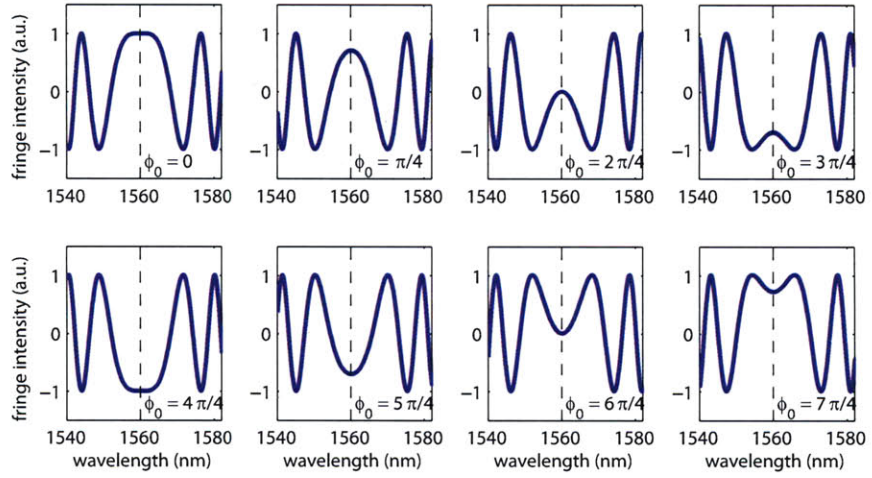
Figure 5-7: Fringe patterns for various ϕ_0 values.
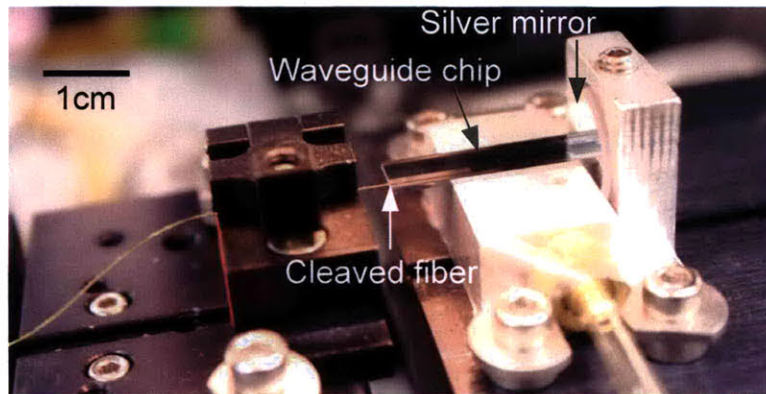
Figure 5-8: A photo of setup to align the cleaved fiber to the waveguide chip that was used for the dispersion measurement.
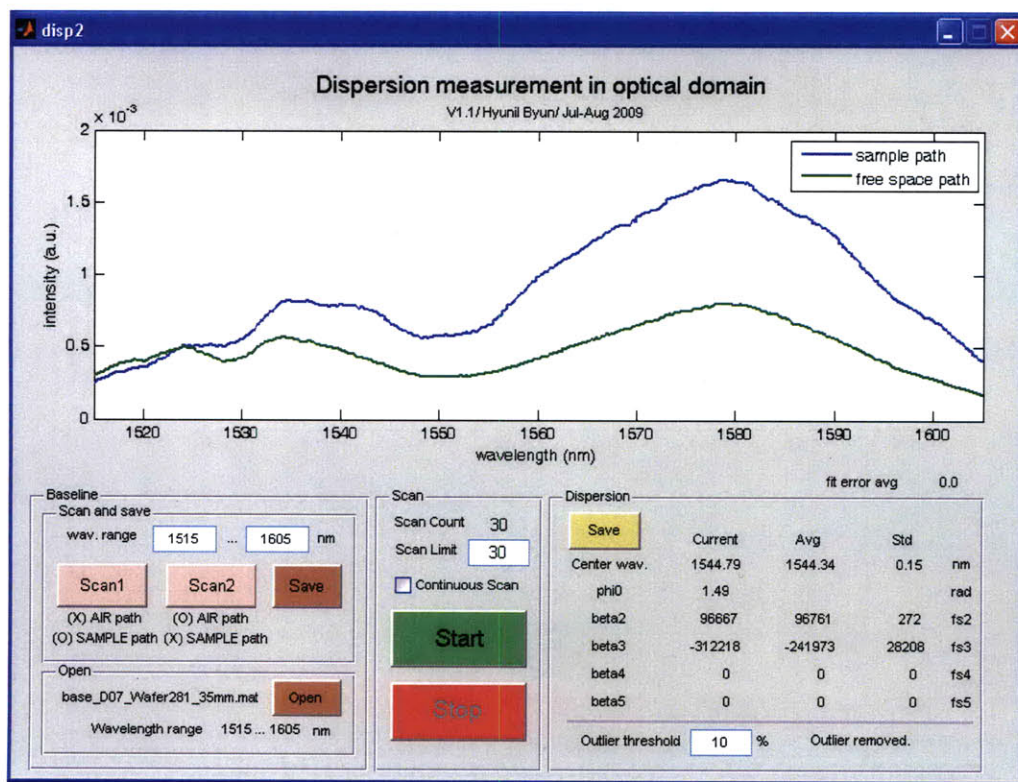
Figure 5-9: A screen shot of **disp2** program after loading the baseline measurement results. Intensities from the sample path and the reference path are plotted.

butt-coupled to a silver mirror and aligned with a cleaved fiber on a XYZ-translation stage.

Three GUIs are used for the dispersion measurement:

1. **disp2** - measures the dispersion at a single wavelength,

2. **step** - tunes the air path length by controlling a stepper motor, and

3. **disp_anal** - compiles the dispersion data from the silver mirror and the DUT at multiple wavelengths, and calculates the net dispersion values.

The baseline measurement is performed by using the panel on the lower left part of **disp2** (Figure 5-9). Wavelengths are set for a range with sufficient spectral power, $\sim$10 dB down from the peak, from the mode-locked laser. Clicking 'Scan1' button measures the reflected spectrum from the sample path, while 'Scan2' button does for the air
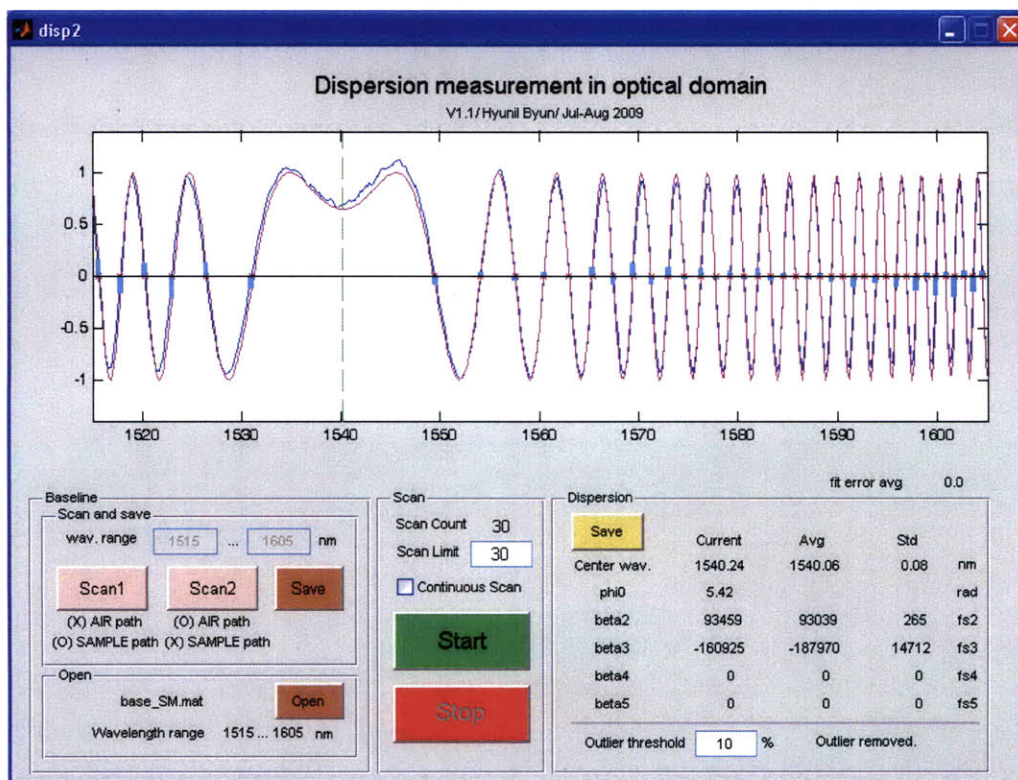
Figure 5-10: A screen shot of **disp2** program after finishing the assigned number of scan. The measured fringe is plotted with the least-mean-sqaure fitting.

path. Before clicking either of button, the unused path should be disconnected - the air path can be blocked by some paper, while the sample path requires disconnecting a FC/APC mating. For each scan, the measured spectrum is displayed on the window. After finishing 'Scan1' and 'Scan2', both paths are recovered. The spectrum data is saved and then loaded by clicking 'Save' and 'Load' button respectively. Previously saved data can be directly open, but it is recommended that the baseline reflectivity is re-measured every day.

With a baseline file open, the dispersion measurement can be started by clicking the 'Start' button (Figure 5-10). The number of scans can be set to 30 by default, which takes about 1 minute. After each scan, the dispersion value is updated on the lower right part of the window. The fringe pattern is fitted by using the second and the third order dispersion only. Increasing the order only enlarges the variance due
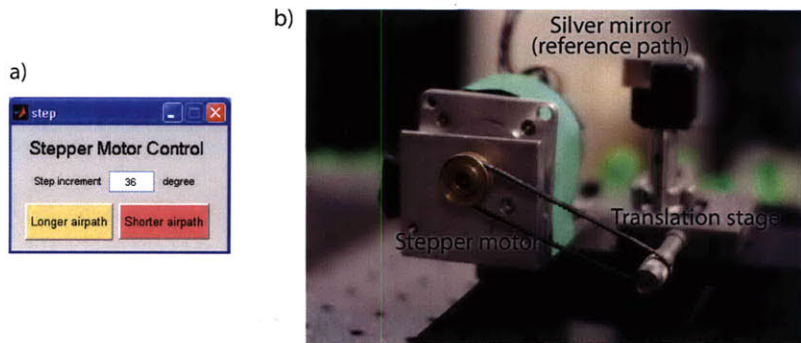
Figure 5-11: (a) A screen shot of **step** program that is used to control the stepper motor and translate the silver mirror in the reference path, (b) picture of the setup to tune the air path length of the reference path.

to the larger degree of freedom to fit the fringes and thus, the fitting is limited by the third order. The 'Outlier threshold' defines how many scans are discarded outside the average, which is set to 10% by default.

The measurement procedure that uses **disp2** can be repeated for different wavelengths. In order to change the center wavelength, the silver mirror in the air path is moved by using **step**, shown in Figure 5-11. Rotating the motor axis by 36 degrees translates the mirror by 50 μm and shifts the fringe wavelength by about 5 nm. Since the silver mirror tuning does not require very good precision or linearity, this setup can be built at a low cost. The motor is TL57ST56-02B2 from Interinar Electronics and controlled by BSD-02LH from the same company via a parallel port.

After gathering dispersion data for the silver mirror calibration and the DUT at multiple wavelengths, **disp_anal** is used to calculate the net dispersion at those wavelengths, shown in Figure 5-12. The standard deviation about 300 fs^2 is also plotted as an error bar at each wavelength. The variation is considered as uncertainty due to the air/temperature fluctuations affecting the length and birefringence of the fiber.
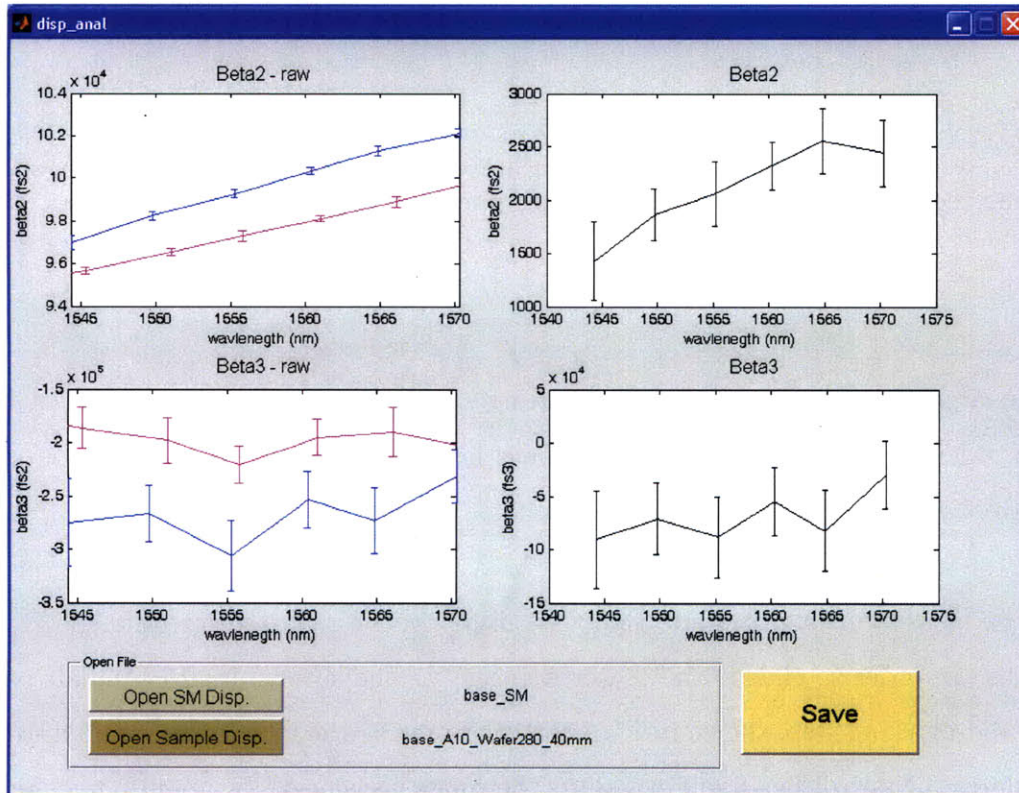
Figure 5-12: A screen shot of **disp_anal** program. The dispersion values from silver-mirror-only case (red) and DUT-inserted case (blue) are shown at the left column, while the net dispersion of the DUT is shown at the right column. The DUT is a 40-mm Er-doped waveguide with 5.75-mm fused-silica waveguides attached on both ends.
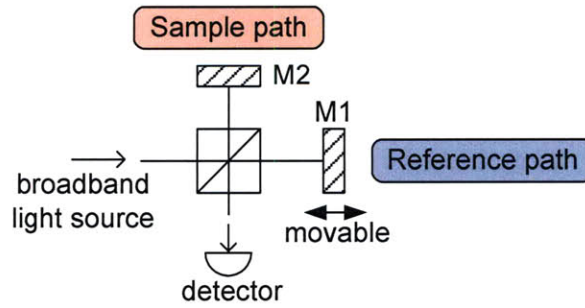
Figure 5-13: A schematic of the balanced Michelson interferometer.

5.1.6 Future work

The measurement setup can be improved by putting electrically-controlled shutters in both the sample path and the reference path. The improvement comes from (1) a faster automated baseline measurement, and (2) no need to disconnect/reconnect the FC/APC connection in the sample path, thus easier to maintain the FC/APC mating quality.

5.2 Spectrally integrated interferometry

This section documents the principle of operation, experimental setup and procedures for the spectrally integrated interferometry built by Jonathan Birge.

5.2.1 Theory [1]

We start from the balanced Michelson interferometer in Figure 5-13, where path lengths in both arms are equal for all frequencies. Let the input field be $\tilde{\mathcal{E}}(t)$ in complex amplitude form. The field from the movable mirror M1 is $\tilde{\mathcal{E}}_1(t - \tau)$ and the field from the mirror M2 is defined $\tilde{\mathcal{E}}_2(t)$. The interferogram on the square-law

147

detector has the form

$$I(\tau) \quad \propto \quad \langle \tilde{\mathcal{E}}_1^2(t-\tau) \rangle + \langle \tilde{\mathcal{E}}_2^2(t) \rangle +$$

$$\langle \tilde{\mathcal{E}}_1(t-\tau)\tilde{\mathcal{E}}_2^*(t) \rangle \exp(-i\omega_l\tau) +$$

$$\langle \tilde{\mathcal{E}}_1^*(t-\tau)\tilde{\mathcal{E}}_2(t) \rangle \exp(i\omega_l\tau), \tag{5.16}$$

where ω_l is the average frequency of the input light. The first two terms are simply the constant average intensity and the second two terms carry the interference information. Let us define the positive spectral component as

$$\tilde{\mathcal{A}}_1^+(\tau) = \langle \tilde{\mathcal{E}}_1^*(t-\tau)\tilde{\mathcal{E}}_2(t) \rangle, \tag{5.17}$$

where $\tilde{\mathcal{A}}_1^+$ is a correlation of $\tilde{\mathcal{E}}_1(t)$ and $\tilde{\mathcal{E}}_2(t)$ and is obtained by recording the interferogram from the detector. Using the fact that the Fourier transform of a correlation of two functions is equal to the product of the Fourier transforms of the respective functions[1], we obtain

$$\tilde{\mathcal{A}}_1^+(\Omega) = \tilde{\mathcal{E}}_1^*(\Omega)\tilde{\mathcal{E}}_2(\Omega), \tag{5.18}$$

where $\Omega = \omega - \omega_l$ is a shifted frequency. For an ideal interferometer, $\tilde{\mathcal{E}}_1(\Omega) = \tilde{\mathcal{E}}_2(\Omega)$, but practically, there can be an arbitrary amplitude and phase difference between the two fields. Therefore, Equation 5.18 takes more general form

$$\tilde{\mathcal{A}}_1^+(\Omega) \quad = \quad \tilde{\mathcal{E}}_1^*(\Omega)\left(\tilde{r}_{12}(\Omega)\tilde{\mathcal{E}}_1(\Omega)\right)$$

$$= \quad \tilde{r}_{12}(\Omega)|\tilde{\mathcal{E}}(\Omega)|^2. \tag{5.19}$$

Equation 5.19 indicates that the Michelson interferometer can be used to measure the spectrum of the source. Now, the mirror M2 is replaced with a device under test (DUT) that has an amplitude and phase response of $T(\Omega)$ and $\delta(\Omega)$. The resultant

---

[1]To be strict, Wiener-Khinchin theorem [70] should be used since the lamp is a random source and the signal we see for each mirror delay is not the same.

correlation in frequency domain becomes

$$\tilde{\mathcal{A}}_2^+(\Omega) = \tilde{r}_{12}(\Omega)|\tilde{\mathcal{E}}(\Omega)|^2 T(\Omega) \exp[-i\delta(\Omega)] \tag{5.20}$$

Dividing Equation 5.21 by Equation 5.19, the amplitude and phase response of the DUT is obtained

$$\tilde{\mathcal{A}}_2^+(\Omega)/\tilde{\mathcal{A}}_1^+(\Omega) = T(\Omega) \exp[-i\delta(\Omega)]. \tag{5.21}$$

We are more interested in the phase information $\delta(\Omega)$, which can be expanded about $\Omega_0 = 0$ (the center frequency) by using the Taylor expansion:

$$\delta(\Omega) = \frac{\partial k}{\partial \Omega}\Omega + \frac{1}{2}\frac{\partial^2 k}{\partial \omega^2}\Omega^2 + \frac{1}{6}\frac{\partial^2 k}{\partial \omega^3}\Omega^3 + \cdots . \tag{5.22}$$

By fitting the measured phase response of the DUT to Equation 5.22, the dispersion coefficients, $\frac{\partial^2 k}{\partial \omega^2}, \frac{\partial^3 k}{\partial \omega^3}, \cdots$ are obtained.

5.2.2 The frequency resolution limit by the delay range

The resolution of any Fourier spectrometer is proportional to the inverse of the delay amount of one mirror, or how long the interferogram is recorded. For example, a recording involving 300 fs of delay (or mirror translation of 45 μm) would have a spectral resolution of 5 nm near 750 nm. In order to obtain a resolution of 0.1 nm, the time delay range needs to be extended to 15 ps (or mirror translation of 1.35 mm).

Figure 5-14 illustrates how the resolution is limited by the delay range. Assume the delay range is $\pm\Delta$ and the input beam is monochromatic at wavelength λ_1, or frequency ν_1. The original interferogram is $\cos\left(\frac{2\pi\tau}{\lambda_1}\right)$, but the sampled interferogram during the limited delay of $\pm\Delta$ is $\cos\left(\frac{2\pi\tau}{\lambda_1}\right)\text{rect}\left(\frac{\tau}{2\Delta}\right)$. After a Fourier transform, the frequency component is $2\Delta\text{sinc}\left(2\Delta(\nu - \nu_1)\right)$ and the distance between the zero crossings around the peak is $1/\Delta$. If there is another wavelength components λ_2, or frequency ν_2, its Fourier-transformed interferogram is $2\Delta\text{sinc}\left(2\Delta(\nu - \nu_2)\right)$. If the two

149

(a) Interferogram   (b) Fourier transform
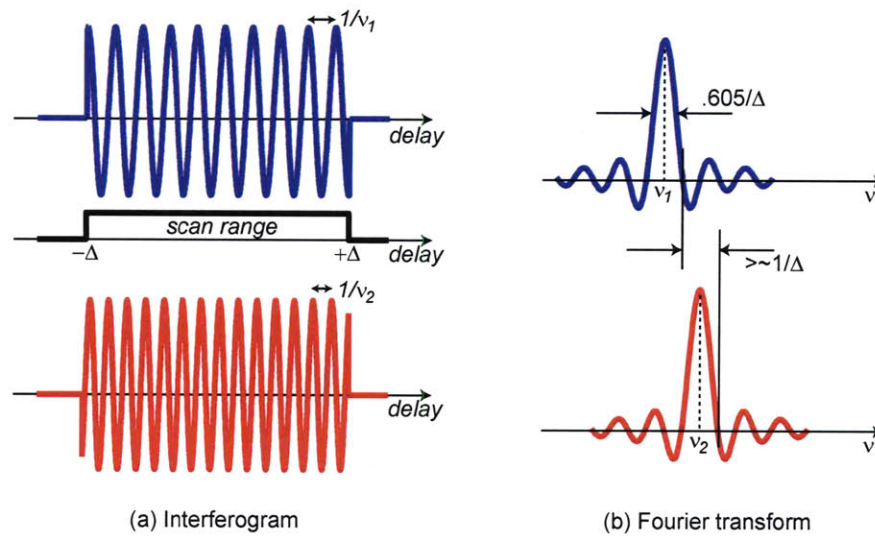
Figure 5-14: (a) Interferograms of monochromatic beams at two different frequencies (ν_1 and ν_2) with a boxcar truncation of a 2Δ-width and (b) the Fourier transform of the truncated interferograms (sinc function). The finite width of the sinc function requires about $1/\Delta$ separation between two different frequencies to resolve.

frequency components are separated more than $1/\Delta$, or if $|\nu_2 - \nu_1| > 1/\Delta$, those two frequencies can be resolved. In fact, since two lines separated by $1/\Delta$ are completely resolved, the practical resolution can be better than $1/\Delta$. Even if the two frequencies are separated by $0.73/\Delta$, those can be resolved with a dip of approximately 20% between two frequency peaks.

The rectangular truncation of the interferogram provides good frequency resolution for signals of comparable strength, but it is poor for signals of disparate amplitudes due to the relatively large sidelobes away from the center frequencies ν_1 or ν_2. This characteristic can be called a low dynamic range. By changing the shape of the truncation function, usually with a smoother transition at each end, the sidelobe amplitude in the Fourier domain can be reduced and signals of disparate amplitudes can be resolved better. Applying various types of truncation functions to the original signal is called apodization that literally means 'removing the foot.' However, with smaller sidelobes, the linewidth of the Fourier transform becomes thicker, which requires larger separation and lowers the resolution for signals of similar strength.

150
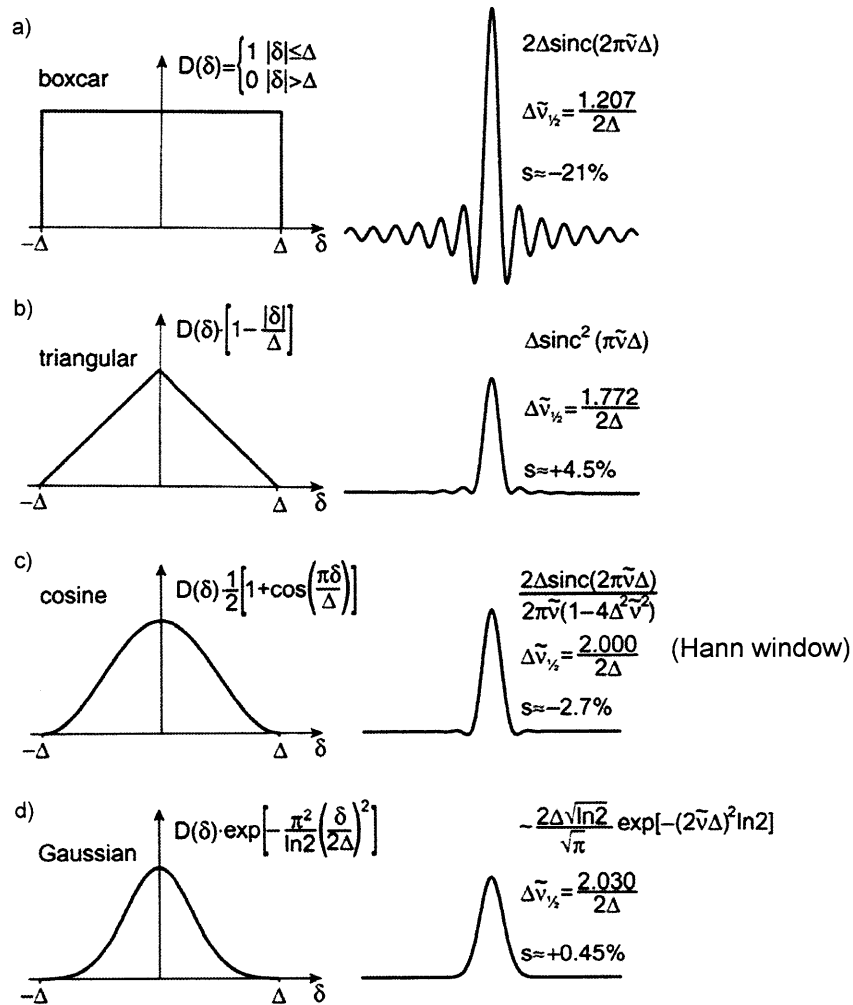
Figure 5-15: Series of apodization function and their Fourier transform: (a) boxcar truncation, (b) triangular, (c) cosine (Hann window), and (d) Gaussian [9]. There is a trade-off between the linewidth in Fourier domain and the sidelobe amplitude. The Hann window in (c) is chosen for our setup as a moderate apodization function.
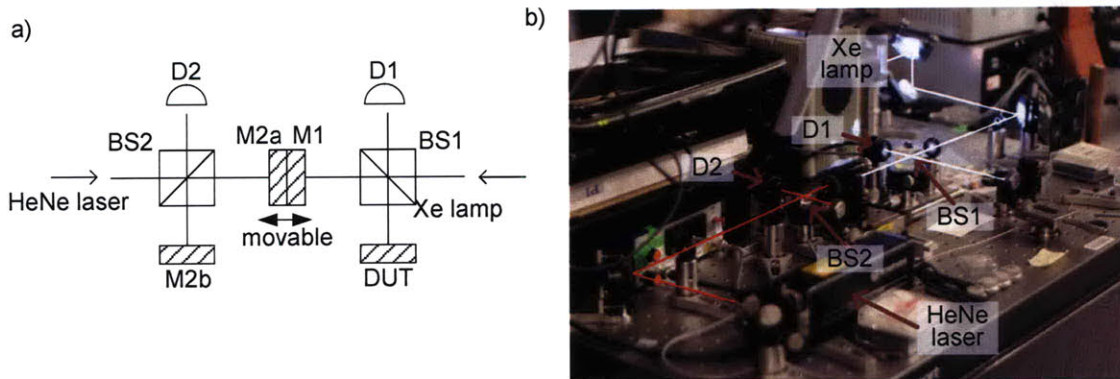
Figure 5-16: (a) A schematic diagram and (b) a picture of experimental setup for the spectrally integrated dispersion. D1, D2: detectors, M1, M2a, M2b: silver mirror, BS1, BS2: beam splitter, DUT: device under test.

Thus, there is a trade-off between the linewidth in Fourier domain and the sidelobe amplitude, shown in Figure 5-15. The Hann function in (c) is chosen for our setup as a moderate apodization function.

The windowing that uses a proper window function with smaller sidelobes is important especially for the Xe lamp that contains spikes on its spectrum. Convolving the Xe source with a sinc function (simple boxcar truncation) would result in large measurement errors.

5.2.3 Measurement setup

Figure 5-16 shows the schematic and the experimental setup for the dispersion measurement. The Xe arc lamp source (Newport 6251NS) is connected to a dedicated power supply (Newport 69907) and enclosed by a housing (Newport 60025). The lamp light itself and its reflection from the real reflector (Newport 60005) inside the housing are collimated by a condenser lens (Newport 60008) mounted in the housing. The collimated whitelight source is split into two paths by the beam splitter BS1, and each path is reflected by the reference mirror M1 and the DUT respectively. The interference fringe is detected by the detector D1, which is chosen by the wavelength range of interest. In our case, an amplified InGaAs detector (Thorlabs PDA400)

152

was used with the lowest amplification setting (1.5×10^4 V/A). The InGaAs detector covers from 800 nm to 1700 nm, and a different detector can be used to detect other wavelength region. The reference mirror M1 is moved back and forth on a translation stage by a pizeo-actuator (Physik Instrumente). The maximum travel range is about 340 μm with 150 V_{pk-pk}. The beam is 2.5" above the bread board surface.

The piezo actuator translates the mirror M1 almost linearly to the applied voltage, but not perfectly. Thus, another interferometer with a HeNe laser (λ=632.991 nm), comprising M2a, M2b, BS2 and D2, is used to compensate the nonlinear translation of the mirror M1. The detector D2 is an amplified silicon detector (Thorlabs PDA55).

The outputs of the detector D1 and D2 are connected to analog input channels of a DAQ box (NI DAQPad-6052E). It is important to sample the signal from both detectors at the same time to avoid extra synchronization process. The synchronized sampling is known to occur at special sampling rates of 55 kSPS or 155 kSPS. A triangular waveform is generated from an analog output channel of the DAQ box and amplified to 0-150 V scale. The triangular waveform output is also fed into the trigger input of the DAQ box to initiate the recording of the interferogram with a pre-defined timing.

5.2.4 Measurement procedure

The dispersion is measured with the following steps:

1. Alignment of silver mirror

   A Ø1" silver mirror is mounted in place of M1 for a baseline measurement. The mirror mount for M1 has tilt adjustments in two axes and the mount is sitting on a linear translation stage that can adjust the distance between the beam splitter BS1 and the mirror M1. Thus, there are three knobs to tune for an optimized alignment. The tilt adjustment is first performed such that the interferogram contrast is maximized and then the linear stage is aligned such that the peak centers within the recording range. The tilt adjustment can be assisted by seeking an interference pattern in front of the detector D1, which appears
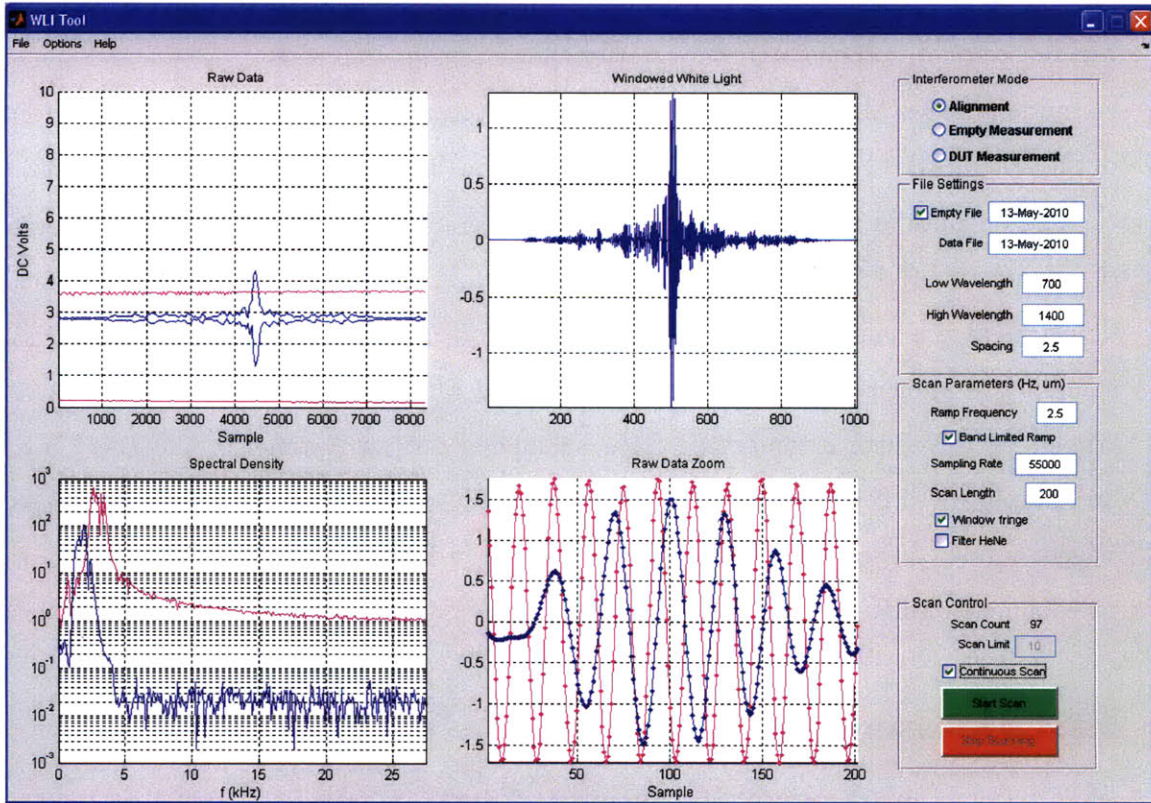
Figure 5-17: A screenshot of **wlitool** for the alignment mode. Upper left: the envelopes of interferometric fringes from the HeNe interferometer (magenta) and the whitelight interferometer (blue). Upper right: Windowed whitelight fringe. Lower left: Spectra of the HeNe fringe (magenta) and the whitelight fringe (blue). Lower rigth: the HeNe fringe (magenta) and whitelight fringe (blue) within 100 samples near the peak.
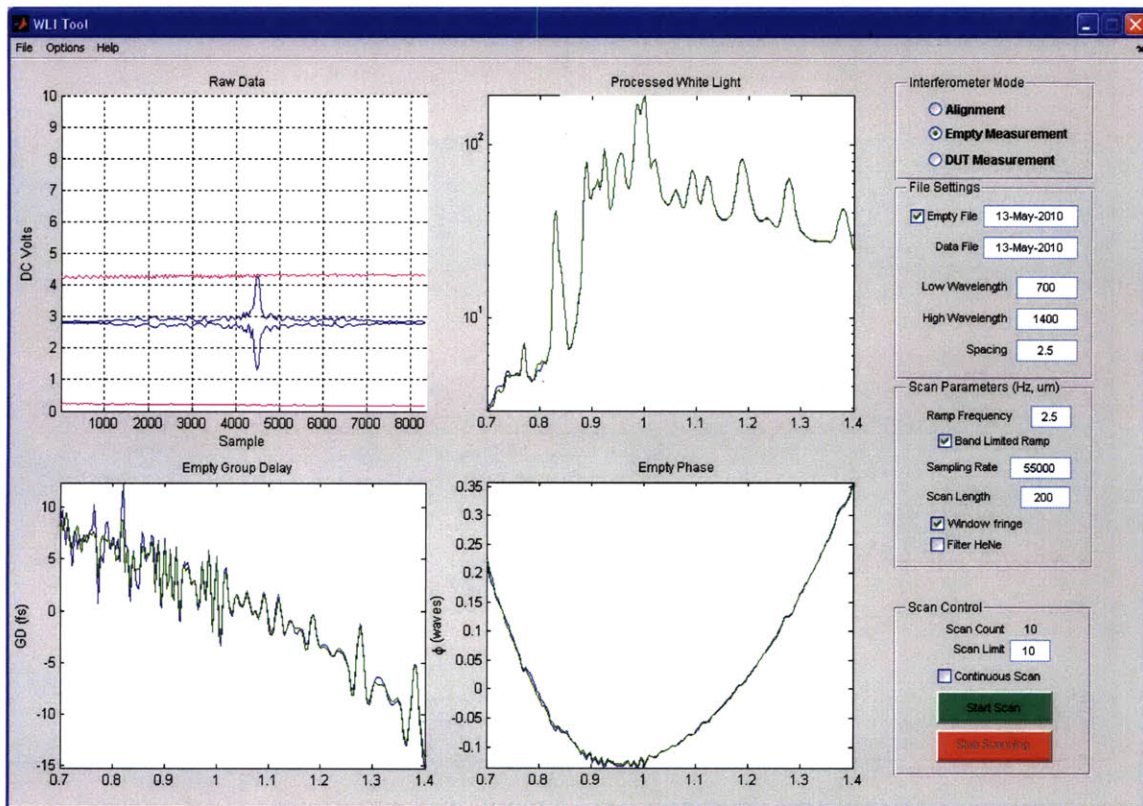
Figure 5-18: A screenshot of **wlitool** for the empty measurement mode. Upper left: the envelopes of interferometric fringes from the HeNe interferometer (magenta) and the whitelight interferometer (blue). Upper right: spectrum of the windowed whitelight fringe in logarithmic scale. Lower left: group delay calculated from the phase of the windowed whitelight fringe. Lower right: Processed phase of the windowed whitelight fringe. Constant and linear phase components are removed such that the curve shows the higher-order dispersions. * In all plots except the upper left one, blue curves show the recent scan results while green curves average all scans.
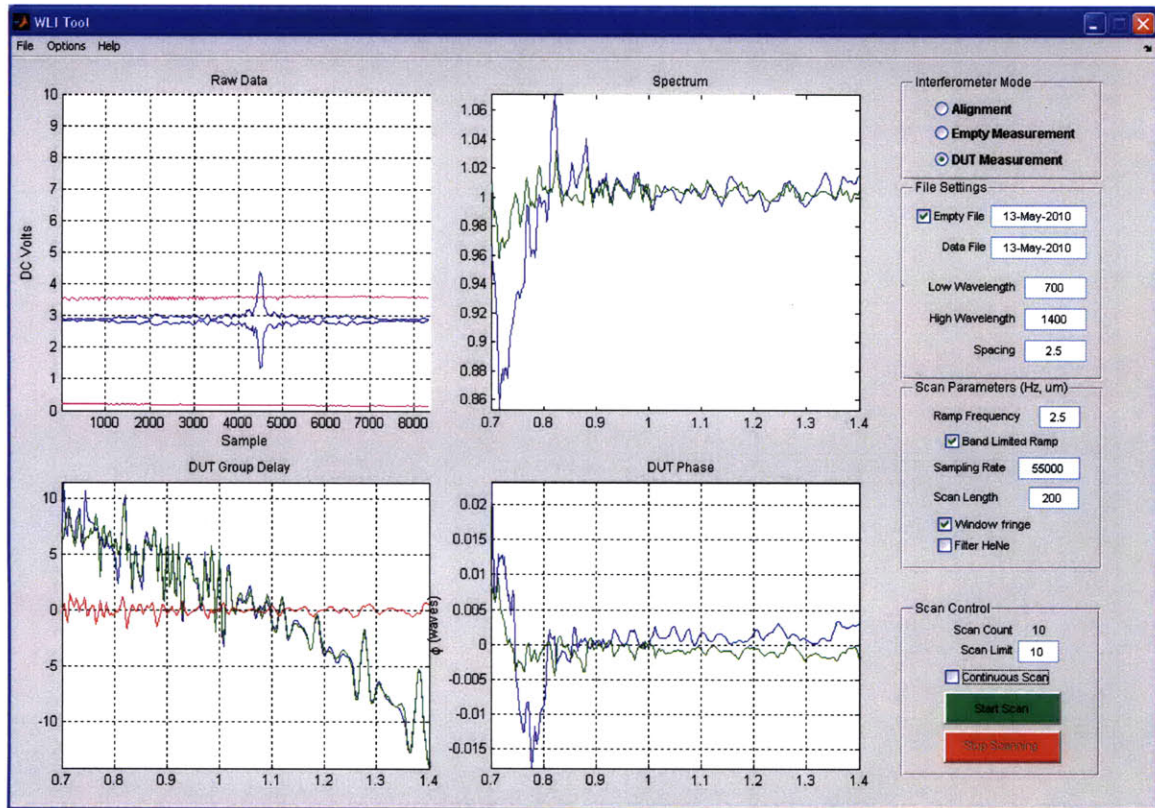
Figure 5-19: A screenshot of **wlitool** for the DUT measurement mode. The DUT is the same silver mirror used for the empty measurement. Upper left: the envelopes of interferometric fringes from the HeNe interferometer (magenta) and the whitelight interferometer (blue). Upper right: spectrum of the windowed whitelight fringe in linear scale, normalized by the spectrum of the empty measurement. Lower left: group delay (red) calculated from the phase of the windowed whitelight fringe, subtracted from the group delay of the empty measurement. Lower right: Processed phase of the windowed whitelight fringe, subtracted from the phase of the empty measurement. Constant and linear phase components are removed such that the curve shows the higher-order dispersions. * In all plots except the upper left one, blue curves show the recent scan results while green curves average all scans.

only when two beams from the two paths are exactly parallel. Filtering out the whitelight source by using a narrow-band filter may help finding the interference pattern. The tilt adjustment can be further optimized while watching the real-time interferogram (wlitool alignment mode) after finishing the linear translation adjustment. Figure 5-17 shows a screen shot of the MATLAB application (wlitool) for the alignment step.

2. Empty measurement

   The empty measurement is performed to measure the phase response of the setup itself. The scans for the empty measurement start by clicking the 'Start' button on the wlitool window. When the scan count reaches a pre-define number, the scan stops and the results are saved onto files. Figure 5-18 shows a screen shot of wlitool for the empty measurement.

3. Alignment of DUT

   Aligning the DUT is very similar to the alignment of the silver mirror. However, the DUT may be much smaller than Ø1" diameter unlike the silver mirror or may reflect only small portion of the incoming beam after transmitting most. In either case, it is usually difficult to see the interference pattern in front of the detector. Additionally, the interference pattern is extremely sensitive to the misalignment of the DUT. The peak value of the interferogram decreases to 10% by rotating the 100-TPI (thread per inch) tilt knob of the DUT mount only by 5°. A CCD camera can be used for the tilt adjustment of the DUT mount:

   (a) The camera is mounted between the detector D1 and the beam splitter BS1.

   (b) The DUT path is blocked and the camera is adjusted such that the beam is centered on the CCD sensor.

   (c) The reference path is blocked and the DUT path is unblocked.

   (d) The beam position will be different from that from the reference path. The

tilt knobs of the DUT mount are adjusted such that the beam on the CCD sensor falls onto the same position as from the reference path.

The above procedure may not perfectly align the tilt of the DUT mount, but it usually allows the interferogram to be distinguishable from the detector noise.

4. DUT measurement

The same procedure as the baseline measurement is performed. The spectrum, group delay and group delay dispersion values are subtracted from the empty measurement, such that those values show the contribution of only the DUT. Figure 5-19 shows a screen shot of **wlitool** for the DUT measurement mode. The DUT here is the same silver mirror used for the empty measurement. The spectrum is close to the unity, and the group delay and the higher-order phase are almost zero, as expected. The deviation of the spectrum and the phase below 800 nm may originate from the lower responsivity of the InGaAs detector.

5.2.5 Data Processing

The ramp signal triggers the DAQ box to start recording the interferogram. When the data acquisition is finished for each scan, a function is called back and performs the following data processing:

1. Two interferograms are retrieved. Let V_{r0} be from the HeNe interferometer and V_{w0} from the whitelight interferometer.

2. Rough AC coupling is implemented by subtracting the average.

$$V_r = V_{r0} - \Sigma V_{r0}/N \qquad (5.23)$$

$$V_w = V_{w0} - \Sigma V_{w0}/N, \qquad (5.24)$$

where N is the number of samples.

3. V_r can be optionally filtered with a 128-tap finite-impulse-response (FIR) filter to reduce its noise.
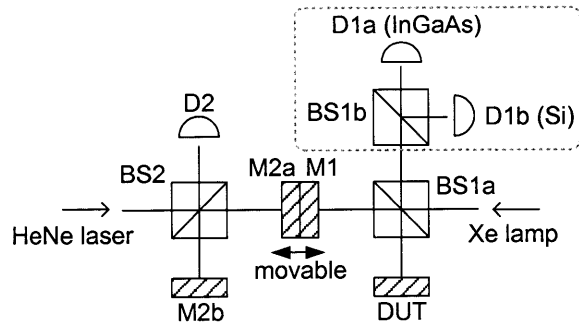
Figure 5-20: A whitelight interferometry with dual detectors to cover a broader range of wavelength. The output of the whitelight interferometer is split by the beam splitter BS1b and fed into two different detectors; Si detector (400 nm - 1100 nm) and InGaAs detector (800 nm - 1700 nm).

4. The Hann window is applied on V_w within the range corresponding to a desired resolution (Section 5.2.2).

5. The normalized phase is computed from the interference fringe V_r. The zero crossings are calculated as accurately as possible by using a spline interpolation. Then, another cubic spline of phase is fitted between the zero crossings. This allows for easy warping of signals; they can simply be interpolated on a regular phase grid by using the output of this method as a new ordinate variable[2].

6. V_w is linearized by using the calculated normalized phase from the above step and Fourier-transformed to retrieve the spectrum and phase.

7. Group delay is calculated by differentiating the phase in frequency domain (not wavelength domain), and similarly group delay dispersion is calculated by differentiating the group delay in frequency domain.

5.2.6 Future work

The wavelength range of the current interferometer is limited by the responsivity of the detector D1. Combining different detectors with different wavelength ranges can

---

[2]The warping of signal can be simply substituted by sampling the signal at every zero-crossing of the HeNe interferogram only if the sampling is slower than the rate of HeNe zero crossings. Otherwise, the signal needs to be properly warped to avoid aliasing.

broaden the wavelength range, as shown in Figure 5-20. The output of the whitelight interferometer is split by the beam splitter BS1b and fed into two different detectors, which can be the combination of a Si detector (400 nm - 1100 nm) and an InGaAs detector (800 nm - 1700 nm). Major work will be implementing the way of combining two fringes from the two detectors.

Chapter 6

Microwave signal extraction from mode-locked lasers

In large-scale, high-precision timing distribution systems [71, 72, 73], a drift-free low-jitter microwave signal is crucial. In the radio astronomy application [71], for example, 64 12-m parabolic antennas are arrayed to detect millimeter and sub-millimeter wavelength microwaves in the frequency band between 31-950 GHz. One critical requirement is that the local oscillator reference signal arriving at any antenna must be stably synchronized within 38 fs; a low-jitter microwave signal is required for the synchronization. Another important motivation of long-term drift-free microwave signal extraction is to read out atomic optical clocks into microwave signals [74, 75].

It is highly nontrivial to transfer the low-jitter property of optical signals into microwave signals. Conventional method of direct detection that uses photodetectors suffers from excess phase noise [76]. Major origin of this excess phase noise is the amplitude-to-phase conversion in the photodetectors. Intensity fluctuation and power drift can be converted significant amount of timing jitter [77]. Although careful suppression of these excess noise demonstrated a short-term (a few second) jitter of 1-fs level [74, 75], slow phase drift of extracted microwave signal is still the major limitation. For example, 0.3% amplitude fluctuation induced 56-fs drift over 100 seconds [74].

To improve long-term stability of microwave signal extraction while circumvent-

ing the amplitude-to-phase conversion, a balanced optical-microwave phase detector (BOM-PD) was proposed and demonstrated [78]. It is based on the precise phase detection in the optical domain, and it uses a differentially-biased Sagnac loop and synchronous detection. Because the phase error between the optical pulse train and the microwave signal is detected by electro-optic sampling in the optical domain, it has a potential to be more robust against power and thermal drifts [79].

A Sagnac loop with phase modulators has recently been integrated by using Silicon waveguide technology in collaboration with the Sandia National Laboratory. In this chapter, we present preliminary results of microwave signal extraction by using the integrated Sagnac loop.

6.1 Principle of operation

In this section, we qualitatively explain the operation of a BOM-PD. Detailed analysis on the operation and noise limit can be found in Kim *et al.* [79].

6.1.1 Pulse train input to a differentially-biased Sagnac loop

General operation of a differentially-biased Sagnac loop is illustrated in Figure 6-1. The loop has the following conditions.

1. A pulse train with a repetition rate of f_R is applied to the Sagnac loop.

2. The phase is modulated by a reference signal at a repetition rate of $(M+0.5)f_R$, where M is a non-negative integer.

3. The phase modulator is placed where the counterclockwise-traveling pulses lag behind the clockwise-traveling pulses by $1/(2M+1)f_R$ or half-period of the reference signal.

Assume that the pulse A is split into A' (clockwise) and A'' (counterclockwise) and the phase is modulated with amplitude of $\varphi/2$. When the pulse A' experiences a phase shift of $+\varphi/2$, the pulse A'' experiences $-\varphi/2$ phase shift since A'' arrives
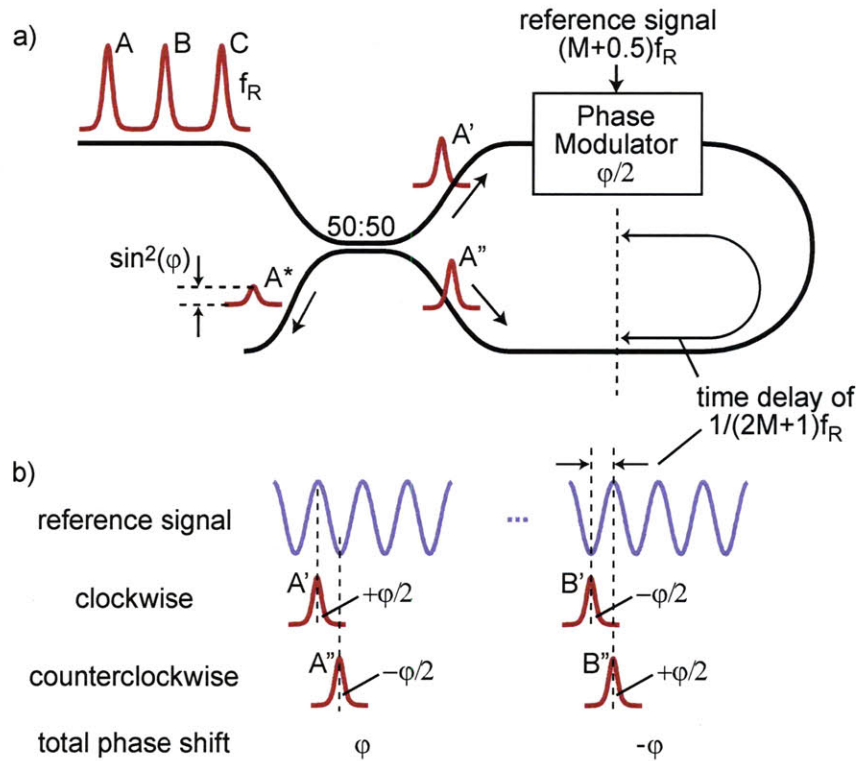
Figure 6-1: (a) Schematic of a Sagnac loop with a phase modulator. Pulse train with a repetition rate of f_R enters the loop and the output pulse height is proportional to $\sin^2(\varphi)$, where $\varphi/2$ is phase modulation in the phase modulator. (b) Timing relation between the reference signal and the pulses inside the loop. The pulses traveling clockwise and counterclockwise are separated by time delay of $1/(2M+1)f_R$ in order to maximize the phase modulation difference.
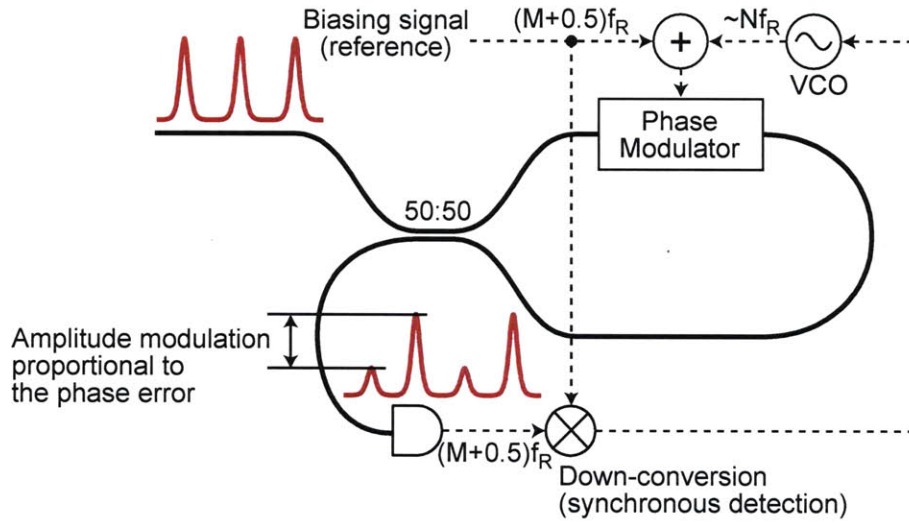
Figure 6-2: Simplified schematic of a BOM-PD. The phase error between the input pulse train and the microwave signal from the VCO is encoded into the amplitude modulation on the output pulses. The modulation strength then adjusts the VCO control voltage such that the phase error is removed. Detailed operation is explained in Figure 6-3.

at the phase modulator later by half-period of the reference signal. Thus the total phase shift of output pulse A^* becomes $+\varphi$. Similarly, the next pulse B^* contains a phase shift of $-\varphi$. In this way, neighboring pulses are biased with the same amount of phase shifts but with alternating signs, although the output pulse amplitudes remain constant.

The position of the phase modulator is critical when the modulation is bidirectional, that is, the pulses propagating in both directions experience phase shift at the modulator. For example, if the phase modulator is placed in the middle of the loop such that the time delay becomes zero, A' and A'' undergo the same phase shift and the total phase shift is canceled to zero.

6.1.2 Balanced optical-microwave phase detection

A simplified schematic of a BOM-PD is described in Figure 6-2. The VCO microwave signal is added to the reference signal such that the phase error between the microwave signal and the laser pulses is converted into the amplitude modulation of the output

pulses. The output optical pulses are transferred to RF domain through a photodetector and mixed with the reference signal to produce a baseband signal containing the amplitude modulation of the output pulses. The down-converted signal alters the VCO control voltage such that the amplitude modulation is minimized and the phase error is removed.

The schematic in Figure 6-2 assumes that the high frequency VCO signal can support a unidirectional phase modulation by using a traveling-wave phase modulator. In contrast, the reference signal at a lower frequency produces a bidirectional phase modulation and requires its position in such a way that counterpropagating pulses at the phase modulator experience opposite phases due to the reference signal, as in the case of Kim *et al.* [79]. If the phase modulator is a lumped element device, the phase modulation is bidirectional for all frequencies, so separate phase modulators for the VCO signal and the reference signal should be placed at different positions.

Detailed operation of a BOM-PD is explained in Figure 6-3. We assume that the pulse repetition rate (f_{rep}) is 508.8 MHz, the reference signal frequency is $12.5f_{rep}$=6.360 GHz, and the VCO signal frequency is roughly $20f_{rep} = 10.176$ GHz. Figure 6-3(a) shows the timing relation between the pulse train and the reference signal. At every pulse peak, the reference signal alternates between its maximum and minimum. Figure 6-3(b1) shows the phase-locked case, where the phase error between the VCO signal and $20f_{rep}$ is zero. The VCO signal crosses with zero at each pulse peak and does not alter the phase modulation by the reference signal. Consequently, the output pulses from the Sagnac loop have constant amplitude of $\sin^2(+\phi_m)$, $\sin^2(-\phi_m)$, $\sin^2(+\phi_m)$, and so on. $\phi_m/2$ is the amplitude of the phase modulation by the reference signal.

Figure 6-3(b2) shows the case of negative phase error, when the VCO signal lags behind the reference signal by θ_e. At each pulse peak, the VCO signal is negative and adds a negative phase to the phase modulation by the reference signal. Thus the odd pulses undergoes a decreased magnitude of phase modulation, while the even pulses experiences an increased magnitude of phase modulation. The phase error θ_e is encoded in the modulated amplitude of output pulses, where odd pulses shrink and
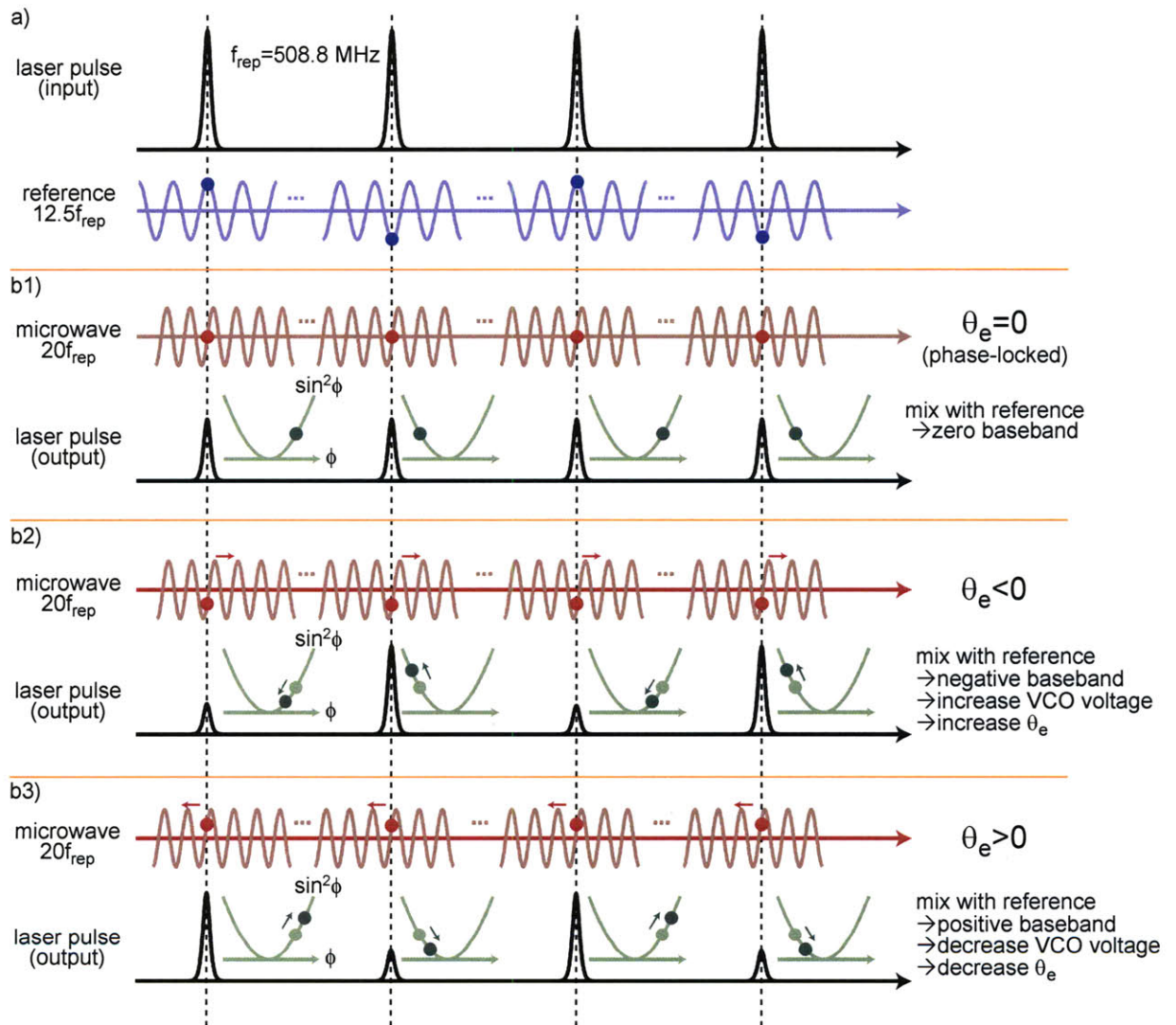
Figure 6-3: (a) Waveforms for the input pulses and the reference signal ($12.5f_R$). (b1)-(b3) Amplitude modulation on the output pulse train; (b1) shows the case of zero phase error, while (b2) and (b3) illustrate the case of phase error θ_e with different signs.

even pulses grow. In this case, the down-converted baseband signal of the output pulses, mixed with the reference signal, is negative on average and the VCO control voltage should increase in order to bring θ_e closer to zero.

Figure 6-3(b3) shows the case of positive phase error, when the VCO signal leads the reference signal by a phase difference of θ_e. In contrast to the case of negative phase error, odd pulses grow and even pulses shrink, resulting in positive baseband signal. The VCO control voltage should decrease in order to bring θ_e closer to zero.

Note the following characteristics:

1. The down-converted signal should connect to the *negative* port of the loop filter that adjusts the VCO voltage, because a negative baseband signal should increase the VCO frequency or phase. This relation assumes that the VCO frequency increases with a higher control voltage, as verified in the lab.

2. The reference signal is desired to be aligned with its extrema to the pulse peak to maximize the differential phase biasing. The VCO signal is aligned such that it zero-crossings fall into the pulse peak to maximize the slope. This relation is valid only when the reference signal is $(M - 0.5)f_R$ and the VCO signal is Nf_R, where M and N are positive integers. In this thesis, M=13 and N=20.

3. In Figure 6-3(b2)-(b3), the phase error θ_e looks constant over the duration of four pulses. It is assumed that the VCO frequency is locked to the repetition rate of the laser pulse. Otherwise we assume that the phase error changes much slower than the pulse repetition rate, such that most of the phase error variation remains within the loop filter bandwidth.

6.2 Integrated Sagnac loop with phase modulators

The Sagnac loop with two phase modulators was designed and fabricated by Jungwon Kim in conjunction with the Sandia National Laboratory by using CMOS-compatible processes. Figure 6-4 shows the picture and schematic of the Sagnac loop on the chip. Each chip, with a dimension of 7.4 × 26.0 mm^2, includes more than 20 Sagnac

167
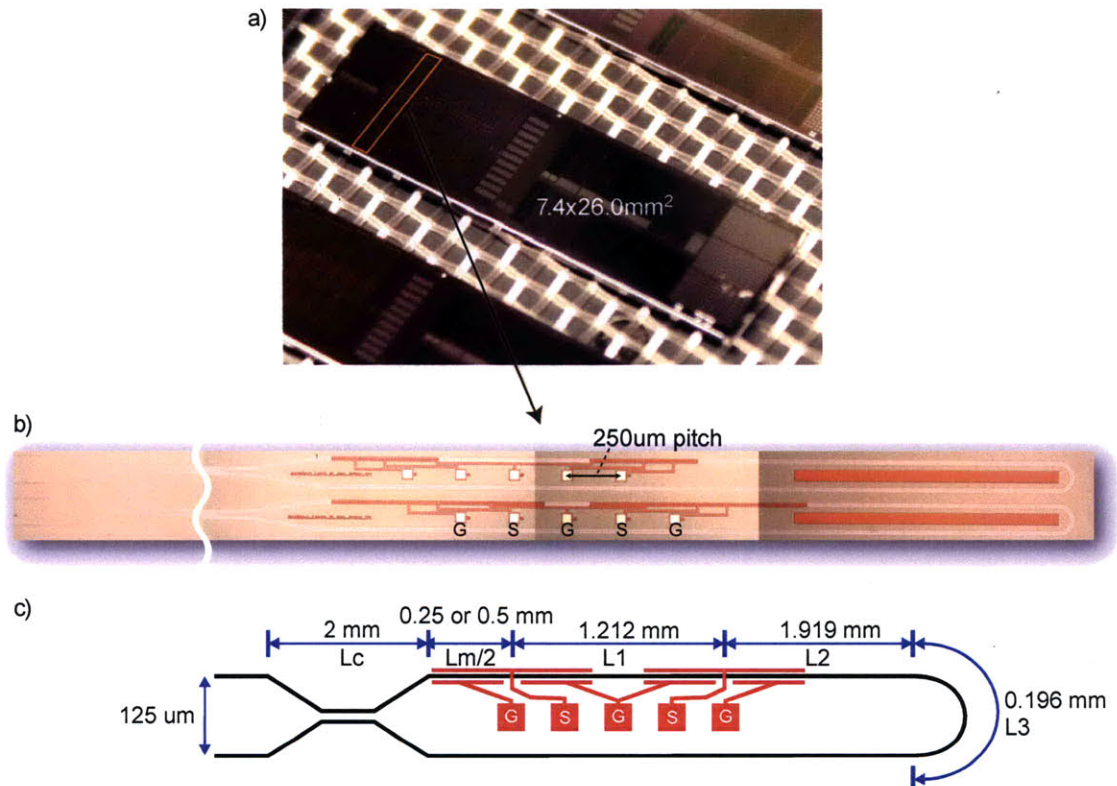
Figure 6-4: (a) Photograph and (b) micrograph of the Sagnac loop chip. In (b), two Sagnac loops are shown with different modulator lengths of 500 μm and 1000 μm respectively. Each Sagnac loop contains two modulators of an identical length at different positions. The electronic contacts are labeled as G-S-G-S-G, where G is ground and S is signal. (c) Schematic of a Sagnac loop with two phase modulators.
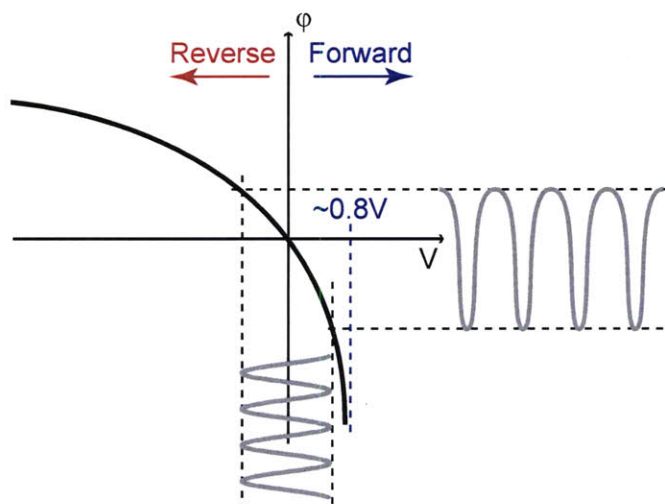
Figure 6-5: Phase modulation curve of a phase modulator as a function of input voltage.

loops with variations of modulator length (500 μm or 1000 μm), loop length (-5%, 0, +5%) or input/output coupling method. In Figure 6-4(b), two Sagnac loops are shown with different modulator lengths of 500 μm and 1000 μm respectively. Each Sagnac loop contains two modulators of identical length at different position; left one for the reference signal at $12.5f_R$=6.360 GHz and right one for the VCO signal at $20f_R$=10.176 GHz respectively. The electronic contacts, with a 250-μm pitch, are labeled as G-S-G-S-G, where G is ground and S is signal.

Detailed dimension of each Sagnac loop is shown in Figure 6-4(c). The pitch between input and output of the loop is set to 125 μm and correspondingly L_3, the bend length, is 62.5π μm=0.196 mm. L_2, the distance between the right modulator and the beginning of the bend, is set to 1.919 mm such that $2L_2+L_3$ creates time delay of 49.0 ps that is equivalent to half period of the VCO signal ($20f_R$=10.176 GHz) between the clockwise-traveling pulses and the counterclockwise-traveling pulses. L_1, the distance between the two phase modulators, is set to 1.212 mm such that $2L_1+2L_2+L_3$ creates time delay of 78.4 ps that is equivalent to half-period of the reference signal ($12.5f_R$=6.360 GHz).

The phase modulation curve is sketched as a function of input voltage in Figure

169

6-5. As the voltage decreases from forward to reverse regime, the phase modulation slope decreases. The phase modulator, based on a depletion-mode p-n diode, becomes slower when the applied voltage is over ~0.8 V because it takes much longer time to charge and discharge the modulator [80]. So it is important to limit the maximum voltage under 0.7-0.8 V to ensure a fast response over 10 GHz. Since the phase modulation slope is dependent on the input voltage, the phase modulation by a sinusoidal voltage is not sinusoidal. Within ±0.7 V range of the input voltage, the phase modulation is estimated to be ~0.2 rad/V on average by a separate experiment that uses the same setup sketched in Figure 6-6. The phase modulation can be enhanced by biasing the input voltage signal to a negative DC voltage and by enlarging the swing of the input signal[1].

6.3 Experimental setup and results

The actual setup is slightly different from the schematic shown in Figure 6-2:

1. Instead of using the transmission port of the Sagnac loop, the reflected light from the input port is separated out by a circulator, because an array of lensed fiber with a 125-μm pitch is not available. Subsequent changes in Figure 6-3 include

    (a) $\sin^2 \phi$ is replaced with $\cos^2 \phi$.

    (b) With negative baseband signals, VCO voltage is decreased and thus the down-converted error signal connects to the *positive* port of the loop filter.

2. The phase modulators are not traveling-wave devices, but lumped element devices for design simplicity. Thus, the phase modulation is bidirectional at both the reference signal frequency and the VCO signal frequency. Consequently, separate modulators are required for both the reference signal and the VCO

---

[1]A bias-tee that covers the signal frequency is required to bias the input signal. The DC-biasing needs to be separately applied to the reference signal and/or the VCO signal. Additional amplifiers may be necessary to increase the voltage swing and to benefit from the DC-biasing.

signal, and each modulator should be placed in such a way that the clockwise-traveling pulses and the counterclockwise-traveling pulses experience opposite phases for a maximum phase modulation at the output of the Sagnac loop.

6.3.1 Fiber-to-chip alignment

Before building a complete setup, the light source should be aligned to the waveguide of the Sagnac loop. A lensed fiber with a spot size of 4 μm is used to convey the light source into the waveguide. Figure 6-6 sketches an experimental setup to align the lensed fiber to the waveguide. Monochromatic light at 1550 nm from a tunable laser source is amplified to about 50 mW by an EDFA and, after passing a circulator, aligned to the Sagnac loop waveguide. Even though the reflected power can be measured through the third port of the circulator, it is hard to distinguish the power reflected from the Sagnac loop from the power reflected from the Si-wafer side surface. Thus the VCO signal (10.176 GHz) is applied to the phase modulator and the reflection port of the circulator is observed through a RF spectrum analyzer during the alignment procedure[2]. The alignment of the lensed fiber is performed until the height of 10.176-GHz component is maximized on the spectrum analyzer. The polarization controller, PC, is also tweaked to maximize the output power from the Sagnac loop. The wavelength from the tunable laser source can also be tuned[3]. Figure 6-6(b) shows the screen of the spectrum analyzer after the alignment is finished with -65 dBm power at 10.176 GHz. When the alignment is finished, the reflected power from the circulator is about 5 mW.
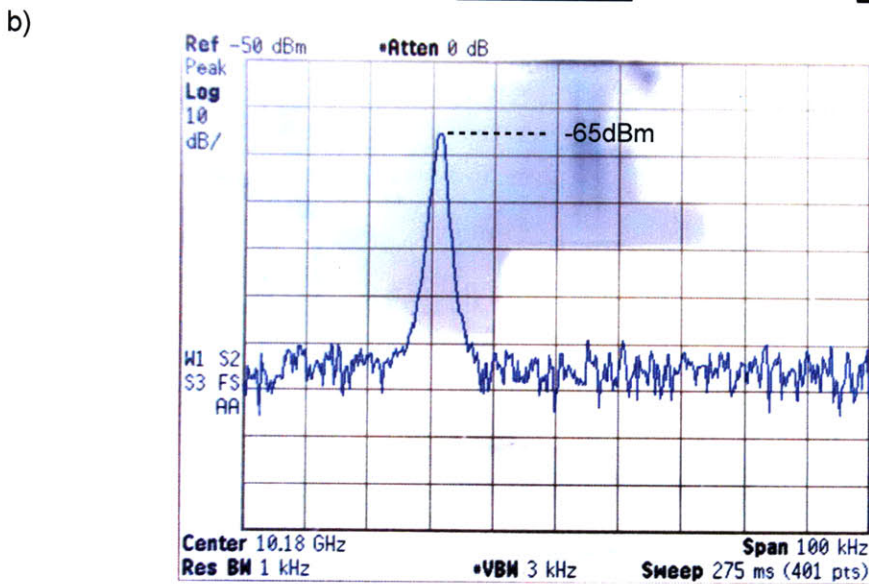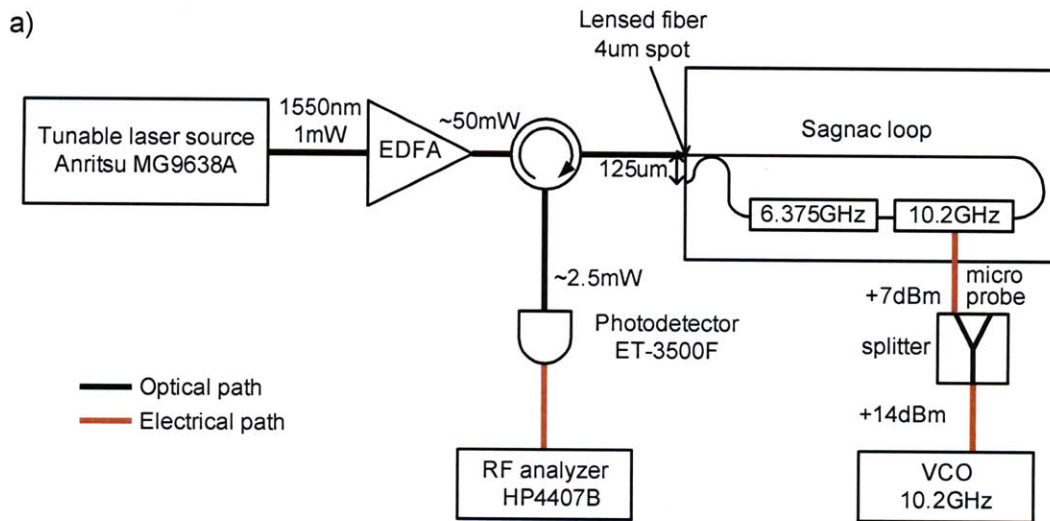
Figure 6-6: (a) Schematic of an experimental setup to align the lensed fiber. The 10.2-GHz phase modulator is modulated by the VCO. (b) RF spectrum of the reflected modulated signal.
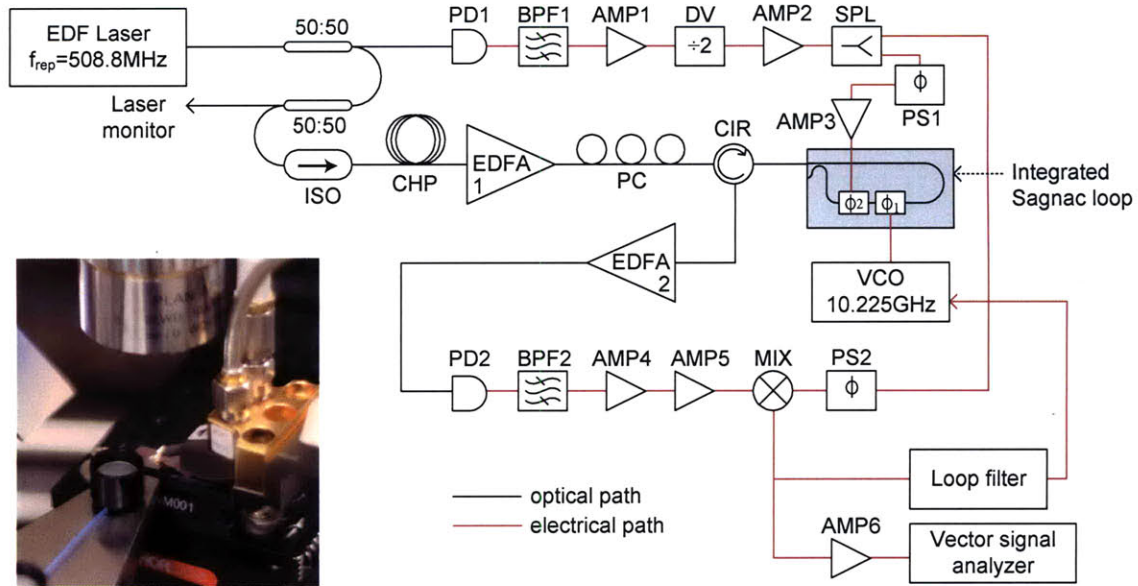
Figure 6-7: Schematic of experimental setup to lock the VCO output frequency to a multiple of the laser repetition rate. The inset is a photograph around the integrated Sagnac loop chip. Each component is detailed in Table 6.1.

Symbol	Description	Model name	Vendor
AMP1	RF amp.	HMC-C016	Hittite
AMP2	RF amp.	HMC-C001	Hittite
AMP3	RF amp.	HMC-C001	Hittite
AMP4	RF amp.	H564 eval. board	Hittite
AMP5	RF amp.	H564 eval. board	Hittite
AMP6	Baseband amp.	AD797	Analog Device
BPF1	Bandpass filter (customized)	K5573 12.75-GHz BPF	TTE
BPF2	Bandpass filter (customized)	K5574 6.375-GHz BPF	TTE
CHP	Pulse-chirping fiber	10-m SMF-28 fiber	Corning
DV	Divider	107197-1 (eval. board)	Hittite
Loop filter		LB1005	NewFocus
MIX	Mixer	ZX05-153-S+	MiniCircuits
PD1, PD2	Photodetector	DSC50S	Discovery
PS1	Phase shifter	P1506	ATM
SPL	Splitter	ZX-10-2-98-S+	MiniCircuits
VCO	Voltage controlled oscillator	DRO-10.225	PSI

Table 6.1: Part list of the experimental setup for microwave signal extraction (in alphabetical order).

6.3.2 Experimental setup

The entire setup to extract a low-noise microwave signal is shown in Figure 6-7, with details of each component listed in Table 6.1. The mode-locked laser provides the phase reference to transfer into the microwave signal, with the same cavity configuration as in Figure 4-16[4]. The laser output power is 7.3 mW and its optical spectrum is 7.8-nm wide, centered at 1569 nm. The optical spectral width corresponds to a 330-fs transform-limited pulse width, assuming a $sech^2$ shape. The repetition rate is 508.8 MHz.

The laser output is split into two paths by a 50:50 coupler. The upper path is detected by a photodetecter PD1, filtered out only for $25f_R$=12.720 GHz, amplified by AMP1, frequency-divided to $12.5f_R$=6.360 GHz by DV, and amplified again by AMP2. The output of AMP2, the reference signal, is split into to two paths; one is used to drive the phase modulator after passing through a phase shifter, PS1, that aligns the extrema to the pulse peaks, and the other is connected to the mixer to down-convert the amplitude-modulated output pulse train, also passing through a phase shifter, PS2.

The lower path from the split laser output passes an isolator to prevent the back-reflection from being re-injected to the laser. Then it is chirped through 10-m SMF to reduce the peak power of pulses and subsequently the TPA-induced loss inside the Si-waveguide. A 330-fs pulse is chirped to a 4-ps pulse before entering the chip waveguide after passing all fiber section. The chirped pulses are amplified by EDFA1 and injected into the Sagnac loop chip through a polarization controller, PC, and a circulator, CIR. We assume that the lensed fiber is already aligned to the waveguide.

The output from the Sagnac loop is amplified by EDFA2, detected by a photodetector PD2, filter out only for $12.5f_R$=6.360 GHz, and amplified by AMP4 and AMP5.

---

[2]The microprobe should have already been contacting the chip electrodes before starting the lensed fiber alignment. The contact of microprobe can be verified by measuring current with a voltage of ~0.8 V applied to one of the modulator. At ~0.8 V, the modulator is slightly turned on and a current of 50-200 μA should be measured.

[3]Due to the Fabry-Perot effect between the lensed fiber and the chip facet, the reflected power is sensitive the incident wavelength. The FSR is about 50 pm in wavelength domain.

[4]The polarization controller is omitted for the experiment in this section and the fiber cavity is enclosed in a box to minimize the temperature-dependent fluctuation of the repetition rate.

The amplified signal, containing the amplitude modulation that corresponds to the phase error θ_e, is down-converted by the mixer and fed into the positive input of the loop filter. The output voltage of the loop filter controls the VCO frequency such that the phase error θ_e becomes zero and the VCO phase is locked to the laser pulses. The down-converted signal is amplified by a low-noise baseband amplifier, AMP6, and measured for the phase noise by a vector signal analyzer (VSA, HP89410a). AMP6 is a non-inverting amplifier that provides a high impedance and the resistance at the inverting port of the OP amp is 10 Ω. The gain of AMP6 is adjusted through a 1-kΩvariable resistor between the non-inverting port and the output port of the OP amp, such that the signal to the VSA is sustained above the noise floor.

6.3.3   Results

The laser output power of 7.3 mW is amplified to about 50 mW by EDFA1. The reflected power is measured about 250-300 μW after the circulator. No matter how much of optical power is coupled into the Sagnac loop, the reflected power is clipped at those levels due to the TPA-induce loss. Using a longer chirping fiber may increase the clipped power level. The reflected power is amplified by EDFA2 to about 5-6 mW before saturating the photodetector PD2.

Before closing the feedback loop, the amplitude-modulated pulse train was measured by a RF spectrum analyzer, shown in Figure 6-8. A RF spectrum around $f_R/2$=254.4 MHz is shown with sidebands around $f_R/2$, caused by frequency difference between $20f_R$ and VCO frequency. The amplitude modulation of output pulses is actually modulated again at the speed of the frequency difference. As the VCO voltage is altered, we note that the frequency difference between $20f_R$ and VCO frequency is also changed. Between 0.3 V and 2.2 V to the VCO voltage, the VCO seems to be locked to the laser with $\sim$0.7 V of the control voltage.

In order to facilitate the locking of the phase-locked loop, it is recommended to bring the sidebands in Figure 6-8 as close as possible to the center at $f_R/2$=254.4 MHz by fine-tuning the VCO with the adjustment screw. The sidebands can also be seen after the mixer, MIX, but the center will be DC instead.
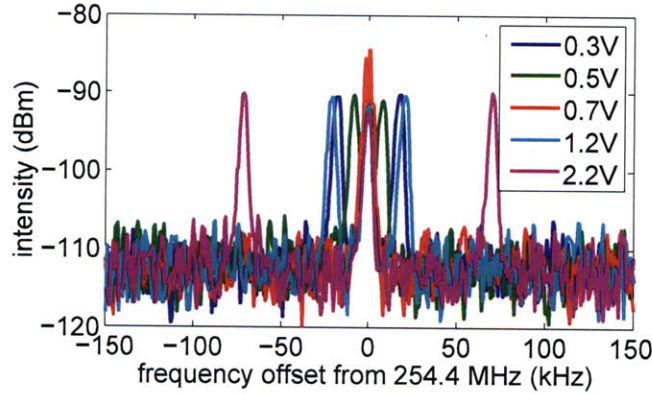
Figure 6-8: Amplitude modulation of output pulses from the Sagnac loop, shown around $f_R/2$=254.4 MHz in RF domain. There are sidebands around $f_R/2$, caused by frequency difference between $20f_R$ and VCO frequency. The amplitude modulation of output pulses is actually modulated again at the speed of the frequency difference. Measured after AMP5, but without EDFA2.

Figure 6-9(a) shows the in-loop single sideband (SSB) phase noise of the phase-locked VCO signal. The phase noise was measured without AMP6. The data from vector signal analyzer in unit of V^2/Hz is normalized to the phase detection sensitivity [V/rad] that is roughly the amplitude of the down-converted signal when the loop is open. The phase detection sensitivity was about 80 mV/rad right after the mixer.

The VCO phase noise was greatly suppressed below 10 kHz, while above 100 kHz an increased noise was measured. The peak near 400-500 kHz comes from the resonance of the feedback loop since the peak frequency changes along with the loop filter bandwidth. The plateau at -100 dBc/Hz after 1 MHz originates from the amplified spontaneous emission (ASE) from the EDFA, further amplified by AMP4 and AMP5. The plateau height substantially increased after adding another amplifier right after AMP5. Because the laser center wavelength is 1569 nm that is far from the gain peak of the EDFA, the amount of ASE is considerably large and increases the higher-frequency phase noise, while the ASE over lower frequencies was suppressed by the feedback loop. Further research will be continued to minimize the phase noise, especially on the higher frequencies over 100 kHz.

The integrated timing jitter is also plotted in Figure 6-9(b), integrated from each

176
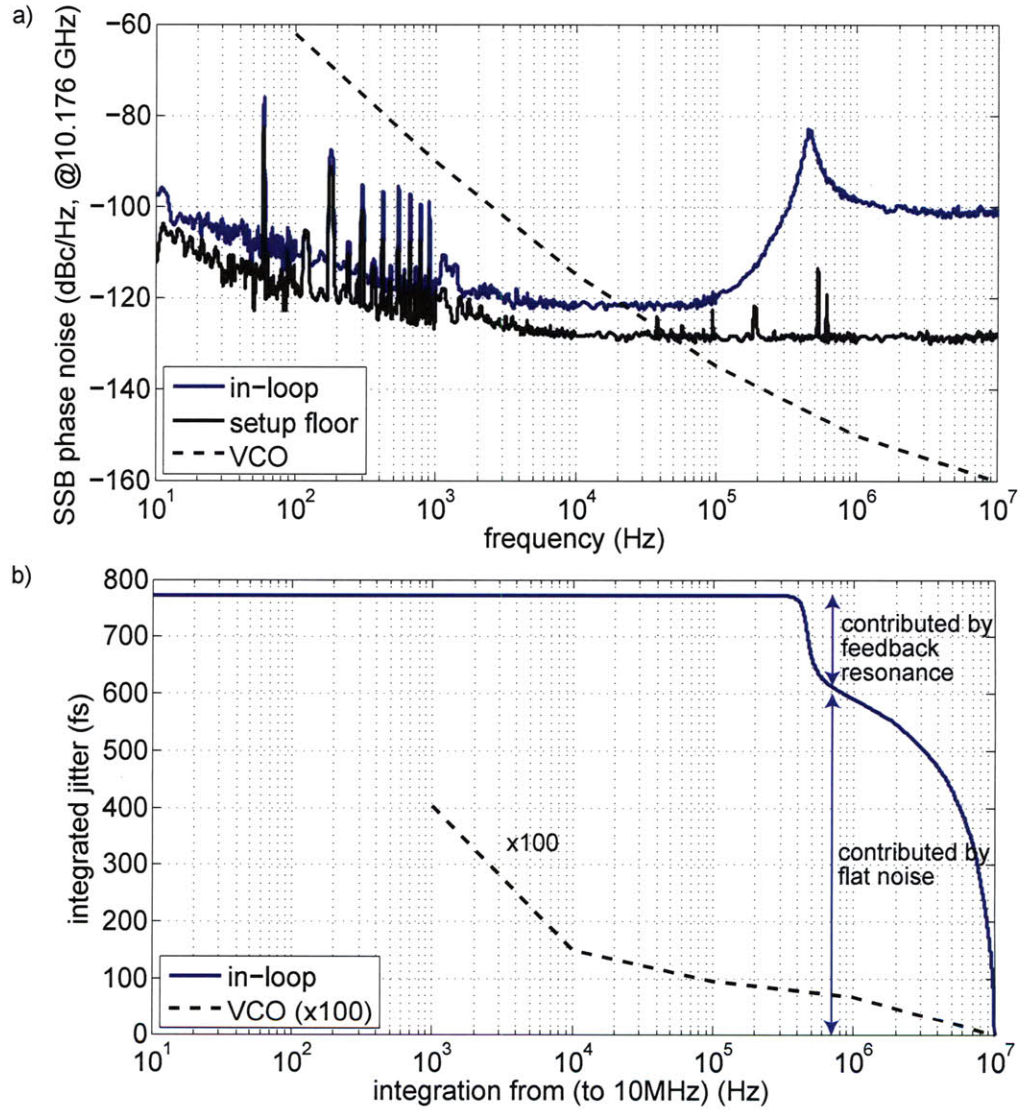
Figure 6-9: (a) In-loop single-sideband (SSB) phase noise of the extracted microwave signal, compared with the setup noise floor and the VCO phase noise from the datasheet. The setup noise floor is measured with the optical input removed from PD2. (b) Integrated timing jitter from each frequency to 10 MHz. The phase noise over MHz-range and the feedback resonance contribute most of the timing jitter.

frequency to 10 MHz at a carrier frequency of 10.225 GHz. The timing jitter from 10 Hz to 10 MHz is calculated to be 772 fs and most of the jitter comes from the feedback resonance and the flat high-frequency noise. The integrated timing jitter from 10 Hz to 100 kHz is only 8.1 fs.

6.4 Summary

The basic operation of a balanced optical-microwave phase detector (BOM-PD) was explained. A BOM-PD converts the phase error between an optical signal and a microwave signal into baseband signal by using a differentially-biased Sagnac loop and synchronous detection. Further the operation of phase locking of a VCO signal into a laser pulse train with a lower timing jitter was explained.

An integrated Sagnac loop with phase modulators based on CMOS-compatible processes was used inside the BOM-PD to demonstrate a phase detection sensitivity of 80 mV/rad. The VCO signal was phase-locked to the pulse train of a 508.8-MHz Er-fiber laser. The phase noise of the VCO was effectively suppressed under 10 kHz, but the suppression was limited by the feedback resonance and the ASE noise from the EDFA over 100 kHz.

6.5 Future work

The first thing to do in the future is to replace current EDFAs with L-band amplifiers to reduce the noise contributed by ASE. After removing the ASE in the C-band, we expect that the high-frequency phase noise will significantly decrease. The L-band amplifier is commercially available from Nuphoton technologies, IPG photonics, Fiber Labs Inc., or Huatai Optic Tech, while it can also be custom-built in the lab [81, 82, 83].

Another thing that can be done for the laser source is to stabilize the output polarization. A rotating polarization would not add any advantages to the operation of the BOM-PD, especially including polarization-sensitive Si-waveguides. A proper

control of polarization on the cavity fiber is required to lock the output polarization as demonstrated in section 4.3.4. The laser source is already equipped with a polarization controller, but needs to be enclosed in a box for further stabilization and a longer-term locking of the output polarization.

The photodetectors with integrated trans-impedance amplifiers (TIA) save the amplifiers, especially AMP4 and AMP5, and reduce the total noise figure of the loop. Because PD1 and PD2 detect signal only within narrow bandwidth around 12.720 GHz and 6.360 GHz respectively, the design constraint of TIAs can be alleviated to some degree.

Once the noise performance is improved, further integration can be attempted. Currently most of the electronics in the loop are made of III-V compound semiconductor and cannot be integrated with the Sagnac loop that is CMOS-compatible. Thus a new scheme to detect the phase error may need to be developed to circumvent the use of III-V materials. On the other hand, high-speed Ge-photodetectors can be integrated by using current technologies at the Sandia National Laboratory. For further integration, current phase modulators can be substituted with traveling-wave phase modulators, which allow for a single phase modulator instead of two inside the Sagnac loop.

Appendix A

Acronyms

ADC	Analog to Digital Conversion
ASE	Amplfied Sponataneous Emission
BOM-PD	Balanced Optical-Microwave Phase Detector
BPF	Band Pass Filter
DAQ	Data AQuisition
DBS	Dichroic Beam Splitter
DFB	Distributed Feed-Back
DUT	Device Under Test
DWDM	Dense Wavelength Division Multiplexing
EDF	Er-Doped Fiber
EDFA	Er-Doped Fiber Amplifer
EPIC	Electronic Photonic Integrated Circuit
Er-doped	Erbium-doped
FSA	Fast Saturable Absorber
FSR	Free Spectral Range
FWHM	Full Width Half Maximum
Ge-doped	Germanium-doped
GTI	Gires-Tournois Interferometer
HT	Hankel Transform

IAC	Interferometric AutoCorrelation
IBS	Ion Beam Sputtering
IHT	Inverse Hankel Transform
LC	Liquid Crystal
MZI	Mach-Zehnder Interferometer
OAWG	Optical Arbitrary Waveform Generation
OC	Output Coupler
OSA	Optical Spectrum Analyzer
PBS	Polarizing Beam Splitter
PD	PhotoDetector
P-doped	Phosphor-doped
PEF	Polarization Evolution Frequency
PLL	Phase Locked Loop
PLVS	Polarization-Locked Vector Soliton
RMS	Root Mean Square
RTD	Resistance Temperature Detector
SMF	Single Mode Fiber
SNSPD	Superconduting Nanowire Single Photon Detector
SOI	Silicon-On-Insulator
SPM	Self Phase Modulation
SSA	Slow Saturable Absorber
SSB	Single Side Band
TIA	Trans-Impedance Amplifier
TLS	Tunable Laser Source
TPA	Two Photon Absorption
VCO	Voltage Controlled Oscillator
VSA	Vector Signal Analyzer

Appendix B

Thin film simulation with beam divergence effect

Given a dielectric coating, the divergence of incident beam can almost be ignored with a beam diameter much larger than the coating thickness. However, as the incident beam diameter becomes comparable to the coating thickness, the effect of beam divergence inside the coating structure becomes significant. For example, a beam radius of 2 μm at a wavelength of 1.55 μm can decrease the reflectivity of a GTI-like layer structure down to 40%, when compared to the large beam reflectivity of 98% (Figure 3-1).

In this appendix, a technique is discussed to simulate any layer structure with a beam divergence effect.

The schematic of a layer structure for simulation is shown Figure B-1. The layers are numbered from 0 to $L+1$, from left to right. The layer 0 and the layer $L+1$ correspond to air and substrate respectively, and the light is incident from the air layer. The radial distribution starts from the center of the beam toward the outer regime with N slices, assuming a cylindrical symmetry.

The incident field and reflected field is defined as E_i and E_r respectively at the boundary of layer 0 (air) and layer 1 (top layer). The transmitted field is named as E_t at the beginning of layer L (substrate). All of E_i, E_r, and E_t are vectors with a dimension of $N \times 1$.
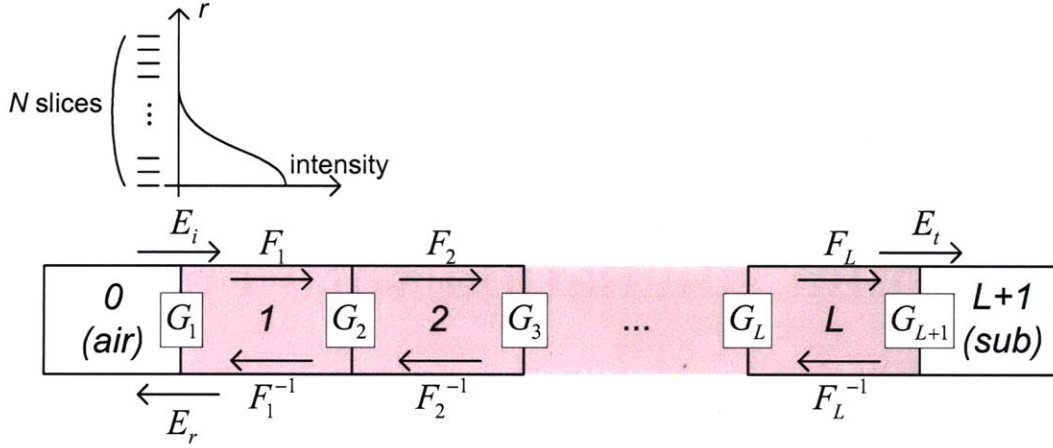
Figure B-1: Structure for the simulation of thin film layers with a beam divergence effect, exemplified by a L-layer film, which is surrounded by air and substrate. In each layer, the light has a distribution over N slices along radial direction. The incident beam is assumed to be cylindrically symmetric.

Figure B-2: Matrix representation for beam propagation at an interface between two different materials with refractive indices n_1 and n_2. S denotes scattering matrix and G does propagation matrix. The propagation matrix can be represented with the scattering matrix coefficients, S_{11} through S_{22}.

The matrices G_1, G_2, $\cdots$, G_L describe the field propagation between layers with different refractive indices. Let a_1 and b_1 be the copropagating and the counterpropagating field in a medium with n_1, respectively, and let b_2 and a_2 be the copropagating and the counterpropagating field in a medium with n_2 respectively (Figure B-2). Then, a scattering matrix S relates the fields:

$$\begin{bmatrix} b_1 \\ b_2 \end{bmatrix} = S \begin{bmatrix} a_1 \\ a_2 \end{bmatrix}, \text{ where } S = \begin{bmatrix} S_{11} & S_{12} \\ S_{21} & S_{22} \end{bmatrix}. \tag{B.1}$$

The scattering matrix S can be converted to a propagation matrix G to describe the field propagation from left to right.

$$\begin{bmatrix} b_2 \\ a_2 \end{bmatrix} = G \begin{bmatrix} a_1 \\ a_2 \end{bmatrix}, \text{ where } G = \begin{bmatrix} S_{21} - S_{22}S_{11}/S_{12} & S_{22}/S_{12} \\ -S_{11}/S_{12} & 1/S_{12} \end{bmatrix}. \tag{B.2}$$

The components of the propagation matrix, S_{11} through S_{22}, are matrices with a dimension of $N \times N$, and thus G is a matrix with a dimension of $2N \times 2N$. The matrix components are defined through

$$S_{11} = \frac{n_1 - n_2}{n_1 + n_2} I_N \tag{B.3}$$

$$S_{12} = \frac{2n_1}{n_1 + n_2} \sqrt{\frac{n_2}{n_1}} I_N \tag{B.4}$$

$$S_{21} = S_{12} \tag{B.5}$$

$$S_{22} = -S_{11}, \tag{B.6}$$

where I_N is a $N \times N$ identical matrix.

The matrices F_1, F_2, $\cdots$, F_L define the propagation of the field in a homogeneous material, in each layer from 1 to L. The input field is decomposed into different frequency components and those components are combined again after experiencing different propagation.

The dimension of F_i is $N \times N$, where $i = 1, 2, \cdots, L$. The calculation of F_i is based on the p-th order quasi-discrete Hankel transform [10] that is implemented in
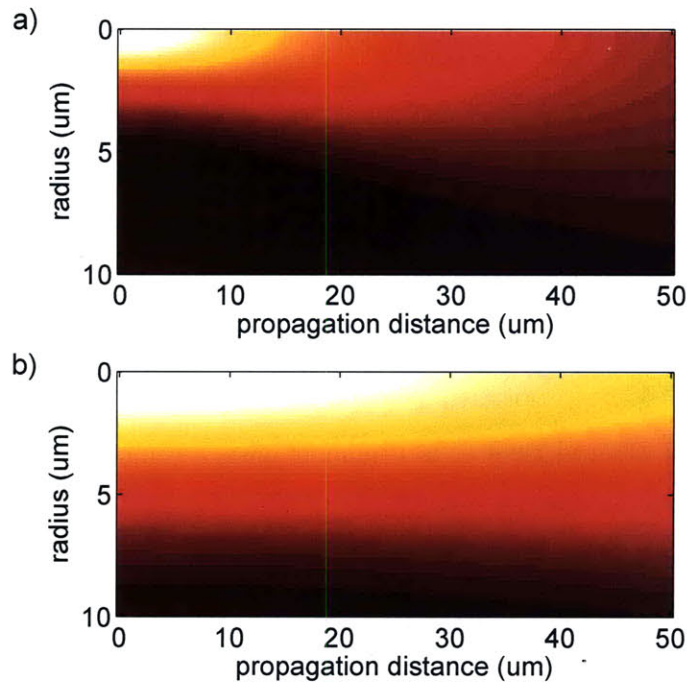
Figure B-3: Calculated propagation of Gaussian beam with its waist at zero distance. (a) Radius of 3 μm and (b) radius of 6 μm. Step sizes are 500 μm along the propagation direction and 0.1 μm along the radial direction. The calculation is based on the p-th order quasi-discrete Hankel transform [10] that is implemented in MATLAB by Gilberto Abram.

MATLAB by Gilberto Abram. The p-th order Hankel transform (HT) and the inverse Hankel transform (ITH) are defined as

$$f_2(\nu) \;\; = \;\; 2\pi \int_0^\infty f_1(r) J_p(2\pi\nu r) r\, dr, \tag{B.7}$$

$$f_1(r) \;\; = \;\; 2\pi \int_0^\infty f_2(\nu) J_p(2\pi r\nu) \nu\, d\nu. \tag{B.8}$$

HT and IHT are especially difficult due to the oscillatory behavior of the Bessel function and the infinite length of the integral. The computation of the integral is also dependent of specific shape of the function to be transformed, so difficult to optimize. After some algebraic manipulation, the HT and the IHT can be discretized to

$$F_2(m) \;\; = \;\; \sum_{n=1}^{N} T_{mn} F_1(n), \tag{B.9}$$

$$F_1(n) \;\; = \;\; \sum_{m=1}^{N} T_{nm} F_2(m), \tag{B.10}$$

where

$$T_{mn} = \frac{2 J_p(\alpha_{pn}\alpha_{pm}/S)}{|J_{p+1}(\alpha_{pn})||J_{p+1}(\alpha_{pm})|S}, \tag{B.11}$$

and α_{pn} is the mth root of the pth Bessel function, and $S \equiv 2\pi RV$. R and V are the truncated radii of the spatial variable and the frequency variable respectively. Equation B.11 is used to calculate the propagation matrix F_i and, once calculated, it is saved as a cache file that can be reused to accelerate similar calculations later. The propagation of a Gaussian beam is simulated using the above HT/IHT calculation in Figure B-3 for beam radii of 3 μm and 6 μm.

The relation between the input field and the reflected/transmitted field is defined by

$$\begin{bmatrix} E_t \\ Z_N \end{bmatrix} = G_{L+1} \left(\Pi_{i=1}^{L} P_i G_i \right) \begin{bmatrix} E_i \\ E_r \end{bmatrix}, \tag{B.12}$$

187
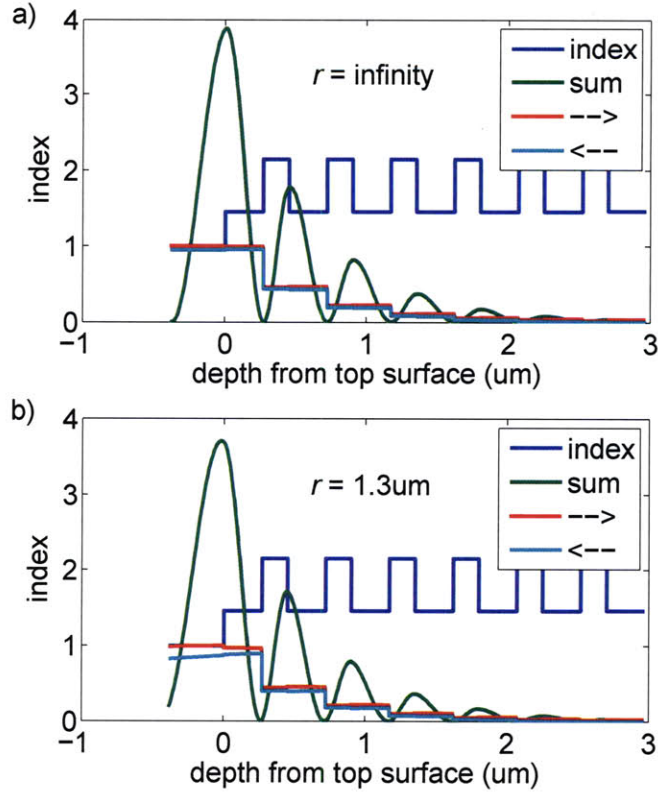
Figure B-4: Field distribution over a 6-pair Bragg reflector made of Nb_2O_5/SiO_2 (a) with infinitely large beam incident and (b) with 1.3-μm radius beam incident. Due to the beam divergence, the reflectivity decreases from 94.7% in (a) to 81.8% in (b).

where

$$P_i = \begin{bmatrix} F_i & Z_{NN} \\ Z_{NN} & F_i^{-1} \end{bmatrix}, \tag{B.13}$$

and Z_N is a $N \times 1$ zero matrix and Z_{NN} is a $N \times N$ zero matrix. The reflected field E_r and the transmitted field E_t can be solved analytically.

$$E_r = -D^{-1}CE_i, \tag{B.14}$$

$$E_t = AE_i + BE_r, \tag{B.15}$$

188

where

$$\begin{bmatrix} A & B \\ C & D \end{bmatrix} \equiv G_{L+1} \left(\Pi_{i=1}^{L} P_i G_i \right), \tag{B.16}$$

and A, B, C, and D are all $N \times N$ matrices.

After the reflected field and the transmitted field are found, the field can be calculated at any point using similar beam propagation. The calculation of the fields can be repeated for various wavelengths. Then, group delay and group delay dispersion can also be evaluated using the phase information of the calculated fields.

A 6-pair Bragg reflector is exemplified for the field calculation with two different beam diameters, in Figure B-4. In (a), the field distribution of the propagating beam, the counter-propagating beam and the combined beam, is plotted for a infinitely large beam radius, that is, a plane wave. The case of a beam radius of 1.3 μm is plotted in (b). In the context of this chapter, the incident beam is assumed to be guided through a fiber or waveguide, so the reflectivity is defined as how much of the reflected field is coupled back into the fiber or waveguide. The reflectivity dropped from 94.7% (infinitely large beam) to 81.8% (1.3-μm radius beam) due to the beam divergence effect.

Bibliography

[1] Scott Diddams and Jean-Claude Diels. Dispersion measurements with white-light interferometry. *J. Opt. Soc. Am. B*, 13(6):1120–1129, 1996.

[2] C. W. Holzwarth, R. Amatya, M. Araghchini, J. Birge, H. Byun, J. Chen, M. Dahlem, N. A. DiLello, F. Gan, J. L. Hoyt, E. P. Ippen, F. X. Kärtner, A. Khilo, J. Kim, M. Kim, A. Motamedi, J. S. Orcutt, M. Park, M. Perrott, M. A. Popovic, R. J. Ram, H. I. Smith, G. R. Zhou, S. J. Spector, T. M. Lyszczarz, M. W. Geis, D. M. Lennon, J. U. Yoon, M. E. Grein, R. T. Schulein, S. Frolov, A. Hanjani, and J. Shmulovich. High speed analog-to-digital conversion with silicon photonics. volume 7220, pages 72200B–15, San Jose, CA, USA, 2009. SPIE.

[3] E. Ippen, A. Benedick, J. Birge, H. Byun, L.-J. Chen, G. Chang, D. Chao, J. Morse, A. Motamedi, M. Sander, G. Petrich, L. Kolodziejski, and F. Kärtner. Optical arbitrary waveform generation, May 16-21 2010.

[4] Felix J. Grawert. *Stabilization Techniques and Silicon-Germanium Saturable Absorbers for High Repetition Rate Mode-Locked Lasers*. PhD thesis, MIT, September 2005.

[5] C. Batten, A. Joshi, J. Orcutt, A. Khilo, B. Moss, C. W. Holzwarth, M. A. Popovic, Li Hanqing, H. I. Smith, J. L. Hoyt, F. X. Kärtner, R. J. Ram, V. Stojanovic, and K. Asanovic. Building many-core processor-to-DRAM networks with monolithic CMOS silicon photonics. *Micro, IEEE*, 29(4):8–21, 2009.

[6] Andrew J. Kerman, Eric. A. Dauler, Bryan S. Robinson, Richard Barron, David O. Caplan, Mark L. Stevens, John J. Carney, Scott A. Hamilton, William E. Keicher, Joel K.W. Yang, Kristine Rosfjord, Vikas Anant, and Karl K. Berggren. Superconducting nanowire photon-counting detectors for optical communications. *Lincoln Laboratory Journal*, 16(1):217–224, 2006.

[7] X. Hu, F.N.C. Wong, and K.K. Berggren. Packaging superconductive nanowire single-photon detectors. Technical report, Massachusetts Institute of Technology, 2008.

[8] N. N. Akhmediev, J. M. Soto-Crespo, S. T. Cundiff, B. C. Collings, and W. H. Knox. Phase locking and periodic evolution of solitons in passively mode-locked fiber lasers with a semiconductor saturable absorber. *Opt. Lett.*, 23(11):852–854, 1998.

[9] Peter R. Griffiths and James A. de Haseth. *Fourier Transform Infrared Spectrometry*. Chemical Analysis: A series of Monographs on Analytical Chemistry and Its Application. Wiley, second edition, 2007.

[10] Manuel Guizar-Sicairos and Julio C. Gutiérrez-Vega. Computation of quasi-discrete hankel transforms of integer order for propagating optical wave fields. *J. Opt. Soc. Am. A*, 21(1):53–58, 2004.

[11] R.H. Walden. Analog-to-digital converter survey and analysis. *IEEE Journal on Selected Areas in Communications*, 17(4):539–550, 1999.

[12] George C. Valley. Photonic analog-to-digital converters. *Opt. Express*, 15(5):1955–1982, 2007.

[13] S. J. Spector, T. M. Lyszczarz, M. W. Geis, D. M. Lennon, J. U. Yoon, M. E. Grein, R. T. Schulein, R. Amatya, J. Birge, J. Chen, H. Byun, F. Gan, C. W. Holzwarth, J. L. Hoyt, E. P. Ippen, F. X. Kärtner, A. Khilo, O. O. Olubuyide, J. S. Orcutt, M. Park, M. Perrott, M. A. Popovic, T. Barwicz, M. Dahlem, R. J.

Ram, and H. I. Smith. Integrated optical components in silicon for high speed analog-to-digital conversion. volume 6477, page 64770O. SPIE, 2007.

[14] J.Shmulovich, A.J.Bruce, G.Lenz, P.B.Hansen, T.N.Nielsen, D.J.Muehlner, G.A.Bogert, I.Brener, E.J.Laskowski, A.Paunescu, I.Ryazansky, D.C.Jacobson, and A.E. White. Integrated planar waveguide amplifier with 15 dB net gain and 1550 nm. *OFC*, 13(16):PD42-1 3, 1999.

[15] F. J. Grawert, J. T. Gopinath, F. Ö. Ilday, H. M. Shen, E. P. Ippen, F. X. Kärtner, S. Akiyama, J. Liu, K. Wada, and L. C. Kimerling. 220-fs erbium-ytterbium:glass laser mode locked by a broadband low-loss silicon germanium saturable absorber. *Optics Letters*, 30(3):329–331, 2005.

[16] Thomas R. Schibli, Kaoru Minoshima, Hiromichi Kataura, Emiko Itoga, Madoka Tokumoto, and Youichi Sakakibara. Saturable absorber mirrors based on polymer-embedded carbon nanotubes and their application to ultrashort pulse generation. In *Conference on Lasers and Electro-Optics/Quantum Electronics and Laser Science Conference and Photonic Applications Systems Technologies*, Technical Digest (CD), page CMJJ2. Optical Society of America, 2006. TY - CONF.

[17] Simon C. Zeller, Thomas Südmeyer, Ursula Keller, and Kurt J. Weingarten. 77-GHz pulse train at 1.5 μm directly generated by a passively mode-locked high repetition rate ErYb:glass laser. In *Conference on Lasers and Electro-Optics/Quantum Electronics and Laser Science Conference and Photonic Applications Systems Technologies*, OSA Technical Digest Series (CD), page CTuC2. Optical Society of America, 2007. TY - CONF.

[18] Christopher Gilmour. Leburn, Alexander A. Lagatsky, Christian Thomas. Brown, and Wilson Sibbett. Femtosecond Cr^{4+}:YAG laser with a 4GHz pulse repetition rate. In *Advanced Solid-State Photonics*, OSA Technical Digest, page WE4. Optical Society of America, 2004. TY - CONF.

[19] A.G. Deryagin, D.V. Kuksenkov, V.I. Kuchinskii, E.L. Portnoi, and I.Yu. Khrushchev. Generation of 110 GHz train of subpicosecond pulses in 1.535 μm spectral region by passively modelocked InGaAsP/InP laser diodes. *Electronics Letters*, 30(4):309–311, 1994.

[20] H.-J. Lohe, R. Scollo, J.F. Holzman, F. Robin, D. Erni, W. Vogt, E. Gini, and H. Jackel. Comparison of monolithically integrated mode-locked laser diodes with uni-traveling carrier and multi-quantum well saturable absorbers. In *The 18th Annual Meeting of the IEEE Lasers and Electro-Optics Society, 2005.*, pages 874–875, 2005.

[21] D. J. Derickson, P. A. Morton, J. E. Bowers, and R. L. Thornton. Comparison of timing jitter in external and monolithic cavity mode-locked semiconductor lasers. *Applied Physics Letters*, 59(26):3372–3374, 1991.

[22] M.G. Thompson, A.R. Rae, R.V. Penty, I.H. White, A.R. Kovsh, S.S. Mikhrin, D.A. Livshits, and I.L. Krestnikov. Absorber length optimisation for sub-picosecond pulse generation and ultra-low jitter performance in passively mode-locked 1.3 μm quantum-dot laser diodes. In *OFC*, volume OthG3, Anaheim, 2006.

[23] Jian Chen, Jason W. Sickler, Erich P. Ippen, and Franz X. Kärtner. High repetition rate, low jitter, low intensity noise, fundamentally mode-locked 167-fs soliton Er-fiber laser. *Opt. Lett. Optics Letters*, 32(11):1566–1568, 2007. TY - JOUR.

[24] Hyunil Byun, Dominik Pudo, Jian Chen, Erich P. Ippen, and Franz X. Kärtner. High-repetition-rate, 491 MHz, femtosecond fiber laser with low timing jitter. *Opt. Lett.*, 33(19):2221–2223, 2008.

[25] Roberto Osellame, Giuseppe Della Valle, Nicola Chiodo, Giulio Cerullo, Stefano Taccheo, Paolo Laporta, Orazio Svelto, Uwe Morgner, Alex Rozhin, and Andrea C. Ferrari. Mode-locked and single-longitudinal-mode waveguide lasers

fabricated by femtosecond laser pulses in Er:Yb-doped phosphate glass. In *Conference on Lasers and Electro-Optics/Quantum Electronics and Laser Science Conference and Photonic Applications Systems Technologies*, OSA Technical Digest Series (CD), page CTuII3. Optical Society of America, 2007. TY - CONF.

[26] J. B. Schlager, B. E. Callicoatt, R. P. Mirin, N. A. Sanford, D. J. Jones, and J. Ye. Passively mode-locked glass waveguide laser with 14-fs timing jitter. *Optics Letters*, 28(23):2411–2413, 2003.

[27] E. P. Ippen. Principles of passive mode locking. *Appl. Phys. B*, 58:158–170, 1994.

[28] Franz X. Kärtner, Juerg Aus der Au, and Ursula Keller. Mode-locking with slow and fast saturable absorbers – what's the difference? *Journal of Selected Topics in Quantum Electronics*, 4(2):159–168, 1998.

[29] U. Keller, K. J. Weingarten, F. X. Kärtner, D. Kopf, B. Braun, I. D. Jung, R. Fluck, C. Hönninger, N. Matuschek, and J. Aus der Au. Semiconductor saturable absorber mirrors (SESAMs) for femtosecond to nanosecond pulse generation in solid-state lasers. *Special issue on Ultrafast Electronics, Photonics and Optoelectronics, IEEE J. Selected Topics in Quantum Electronics (JSTQE)*, 2(3):435–453, 1996.

[30] David Chao, Guoqing Chang, Jonathan L. Morse, F. X. Kärtner, and E. P. Ippen. Octave-spanning supercontinuum generation for an Er-doped fiber laser frequency comb at a 1 GHz repetition rate. page CMN6. Conference on Lasers and Electro Optics (CLEO), May 16-21 2010.

[31] Danna Rosenberg, Adriana E. Lita, Aaron J. Miller, and Sae Woo Nam. Noise-free high-efficiency photon-number-resolving detectors. *Physical Review A*, 71(6):061803, 2005. Copyright (C) 2010 The American Physical Society Please report any problems to prola@aps.org PRA.

[32] J. Zhang, N. Boiadjieva, G. Chulkova, H. Deslandes, G. N. Gol'tsman, A. Korneev, P. Kouminov, M. Leibowitz, W. Lo, R. Malinsky, O. Okunev, A. Pearl-

man, W. Slysz, K. Smirnov, C. Tsao, A. Verevkin, B. Voronov, K. Wilsher, and R. Sobolewski. Noninvasive cmos circuit testing with nbn superconducting single-photon detectors. *Electronics Letters*, 39(14):1086–1088, 2003.

[33] Hiroki Takesue, Sae Woo Nam, Qiang Zhang, Robert H. Hadfield, Toshimori Honjo, Kiyoshi Tamaki, and Yoshihisa Yamamoto. Quantum key distribution over a 40-db channel loss using superconducting single-photon detectors. *Nat Photon*, 1(6):343–348, 2007.

[34] Eric. Dauler. *Multi-element Superconducting Nanowire Single Photon Detectors*. PhD thesis, 2009.

[35] Faraz Najafi *et al.* publication in preparation.

[36] J.-M. P. Delavaux, C. McIntosh, J. Shmulovich, A.J. Bruce, R.K. Pattnaik, and B.R. Wirstiuk. Gain flatness of a planar optical waveguide amplifier. *OFC*, 2000.

[37] Ruby N. Ghosh, Joseph Shmulovich, Casey F. Kane, Miriam R.X. de Barros, Gerald Nykolak, Allan J. Bruce, and Philippe C. Becker. 8-mW threshold Er^{3+}-doped planar waveguide amplifer. *IEEE Photonics Technology Letters*, 8(4):518–520, 1996.

[38] G. Della Valle, R. Osellame, N. Chiodo, S. Taccheo, G. Cerullo, and P. Laporta. C-band waveguide amplifier produced by femtosecond laser writing. *Optics Express*, 13(16):5976–5982, 2005.

[39] Y. C. Yan, A. J. Faber, H. de Waal, P. G. Kik, and A. Polman. Erbium-doped phosphate glass waveguide on silicon with 4.1 dB/cm gain at 1.535 μm. *Applied Physics Letter*, 71(20):2922–2924, 1997.

[40] S. V. Frolov, J. Shmulovich, and A. Bruce. Advances in planar waveguide integration. volume 6389, pages 638905–6, Boston, MA, USA, 2006. SPIE.

[41] J. T. Gopinath. *Studies of third-order nonlinearities in materials and devices for ultrafast lasers*. PhD thesis, Massachusetts Institute of Technology, 2005.

[42] G. Agrawal. *Nonlinear Fiber Optics*. Academic Press, 2001.

[43] Jonathan Birge. *Sub-Two-CycleMode-Locked Lasers*. PhD thesis, Massachusetts Institute of Technology, 2009.

[44] Jungwon Kim, Jeff Chen, Jonathan Cox, and Franz X. Kärtner. Attosecond-resolution timing jitter characterization of free-running mode-locked lasers. *Opt. Lett.*, 32(24):3519–3521, 2007.

[45] F. X. Kärtner and U. Keller. Stabilization of solitonlike pulses with a slow saturable absorber. *Opt. Lett.*, 20(1):16–18, 1995.

[46] Chih-Hao Li, Andrew J. Benedick, Peter Fendel, Alexander G. Glenday, Franz X. Kartner, David F. Phillips, Dimitar Sasselov, Andrew Szentgyorgyi, and Ronald L. Walsworth. A laser frequency comb that enables radial velocity measurements with a precision of $1\,\mathrm{cm\,s^{-1}}$. *Nature*, 452(7187):610–612, 2008. 10.1038/nature06854.

[47] Jason W. Sickler. *High Repetition Rate Mode-locked Erbium-Doped Fiber Lasers with Complete Electric Field Control*. PhD thesis, Massachusetts Institute of Technology, 2008.

[48] C. Hönninger, R. Paschotta, F. Morier-Genoud, M. Moser, and U. Keller. Q-switching stability limits of continuous-wave passive mode locking. *J. Opt. Soc. Am. B*, 16(1):46–56, 1999.

[49] T.R. Schibli, E.R.Thoen, F.X. Kärtner, and E.P. Ippen. Suppression of Q-switched mode locking and break-up into multiple pulses by inverse saturable absorption. *Appl. Phys. B*, 70:S41–S49, 2000.

[50] Scott Davidson (Advanced Thin Films). Private communication.

[51] S.G. Lipson, H. Lipson, and D.S. Tannhauser. *Optical Physics*. Cambridge University Press, 3rd edition, 1995.

[52] Douglas B. Leviton and Bradley J. Frey. Temperature-dependent absolute refractive index measurements of synthetic fused silica. volume 6273, pages 62732K-11, Orlando, FL, USA, 2006. SPIE.

[53] Michelle Sander *et al.* submitted to europhotonics. 2010.

[54] Vescent Photonics. http://www.vescentphotonics.com/.

[55] H.A. Haus and A. Mecozzi. Noise of mode-locked lasers. *Quantum Electronics, IEEE Journal of*, 29(3):983 -996, mar 1993.

[56] Hyunil Byun, Jason Sickler, Jonathan Morse, Jeff Chen, Dominik Pudo, Erich P. Ippen, and F. X. Kaertner. Femtosecond passively mode-locked fiber lasers using saturable bragg reflectors. In *Ultrafast Phenomena XIV: Proceedings of the 16th International Conference*, Springer Series in Chemical Physics, Stresa (Lago Maggiore), Italy, 2008.

[57] T. Shintaku, E. Sugita, and R. Nagase. Highly stable physical-contact optical fiber connectors with spherical convex ends. *Lightwave Technology, Journal of*, 11(2):241 -248, feb 1993.

[58] R. Nagase, T. Shintaku, and E. Sugita. Effect of axial compressive force for connection stability in pc optical fibre connectors. *Electronics Letters*, 23(3):103 -105, 29 1987.

[59] J. J. McFerran, L. Nenadovic, W. C. Swann, J. B. Schlager, and N. R. Newbury. A passively mode-locked fiber laser at 1.54 μm with a fundamental repetition frequency reaching 2 GHz. *Opt. Express*, 15(20):13155-13166, 2007.

[60] J.Chen, J. W. Sickler, H. Byun, E. P. Ippen, S. Jiang, and F. X. Kärtner. Fundamentally mode-locked 3 GHz femtosecond erbium fiber laser. In *Ultrafast Phenomena XIV: Proceedings of the 16th International Conference*, pages 727-729, Italy, 2008.

[61] M. Y. Sander, H. Byun, J. Morse, D. Chao, H. M. Shen, A. Motamedi, G. Petrich, L. Kolodziejski, E. P. Ippen, and F. X. Kärtner. 1 GHz femtosecond Erbium-doped fiber lasers. page CTuII1. Conference on Lasers and Electro Optics (CLEO), May 16-21 2010.

[62] Dominik Pudo, Hyunil Byun, Jian Chen, Jason Sickler, Franz X. Kärtner, and Erich P. Ippen. Scaling of passively mode-locked soliton erbium waveguide lasers based on slow saturable absorbers. *Opt. Express*, 16(23):19221–19231, 2008.

[63] L. Li, H. Li, T. Qiu, V. L. Temyanko, M. M. Morrell, A. Schülzgen, A. Mafi, J. V. Moloney, and N. Peyghambarian. 3-dimensional thermal analysis and active cooling of short-length high-power fiber lasers. *Opt. Express*, 13(9):3420–3428, 2005.

[64] D. N. Christodoulides and R. I. Joseph. Vector solitons in birefringent nonlinear dispersive media. *Opt. Lett.*, 13(1):53–55, 1988.

[65] Steven Cundiff, B. Collings, and Wayne Knox. Polarization locking in an isotropic, modelocked soliton Er/Yb fiber laser. *Opt. Express*, 1(1):12–21, 1997.

[66] A. M. Smith. Birefringence induced by bends and twists in single-mode optical fiber. *Appl. Opt.*, 19(15):2606–2611, 1980.

[67] Franz Kärtner. Private communication.

[68] E. Wu. *Measuring Chromatic Dispersion of Single-Mode Optical Fibres using White Light Interferometry*. Master of science, The University of Auckland, 2006.

[69] Jay N. Damask. *Polarization Optics in Telecommunications*. Springer, 2004.

[70] Wikipedia. Wiener-Khinchin theorem. Website. http://en.wikipedia.org/wiki/Wiener-Khinchin_theorem.

[71] J. F. Cliche and B. Shillue. Precision timing control for radioastronomy: maintaining femtosecond synchronization in the atacama large millimeter array. *Control Systems Magazine, IEEE*, 26(1):19–26, 2006.

[72] Seth M. Foreman, Kevin W. Holman, Darren D. Hudson, David J. Jones, and Jun Ye. Remote transfer of ultrastable frequency references via fiber networks. *Review of Scientific Instruments*, 78(2):021101–25, 2007.

[73] J. Kim, J. Chen, Z. Zhang, F. N. C. Wong, F. X. Kärtner, F. Loehl, and H. Schlarb. Long-term femtosecond timing link stabilization using a single-crystal balanced cross correlator. *Opt. Lett.*, 32(9):1044–1046, 2007.

[74] A. Bartels, S. A. Diddams, C.W. Oates, G.Wilpers, J. C. Bergquist, W. H. Oskay, and L. Hollberg. Femtosecondlaser-based synthesis of ultra-stable microwave signals from optical frequency references. *Opt. Lett.*, 30:667–669, 2005.

[75] J. J. McFerran, E. N. Ivanov, A. Bartels, G. Wilpers, C. W. Oates, S. A. Diddams, and L. Hollberg. Low-noise synthesis of microwave signals from an optical source. *Electron. Lett.*, 41:650–651, 2005.

[76] E. N. Ivanov, S. A. Diddams, and L. Hollberg. Analysis of noise mechanisms limiting the frequency stability of microwave signals generated with a femtosecond laser. *IEEE J. Sel. Top. Quantum Electron.*, 9(1):1059–1065, 2003.

[77] E. N. Ivanov, S. A. Diddams, and L. Hollberg. Study of the excess noise associated with demodulation of ultrashort infrared pulses. *IEEE Trans. Ultrason. Ferroelectr. Freq. Control*, 52:1068–1074, 2005.

[78] J. Kim and F.X.Kärtner. Balanced optical-microwave phase detectors for optoelectronic phase-locked loops. *Opt. Lett.*, 31(24):3659–3661, 2006.

[79] J. Kim, F. Ludwig, M. Felber, and F.X.Kärtner. Long-term stable microwave signal extraction from mode-locked lasers. *Opt. Express*, 15(14):8951–8960, 2007.

[80] Watts Michael, A. Zortman William, C. Trotter Douglas, W. Young Ralph, and L. Lentine Anthony. Low-voltage, vertical-junction, depletion-mode, silicon mach-zehnder modulator with complementary outputs. OSA Technical Digest (CD), page PDPC5. Optical Society of America, 2009.

[81] J. Nilsson, S. Y. Yun, S. T. Hwang, J. M. Kim, and S. J. Kim. Long-wavelength erbium-doped fiber amplifier gain enhanced by ase end-reflectors. *Photonics Technology Letters, IEEE*, 10(11):1551–1553, 1998.

[82] Lee Juhan, Ryu Uh-Chan, Ahn Seong Joon, and Park Namkyoo. Enhancement of power conversion efficiency for an l-band edfa with a secondary pumping effect in the unpumped edf section. *Photonics Technology Letters, IEEE*, 11(1):42–44, 1999.

[83] S. Harun, N. Tamchek, P. Poopalan, and H. Ahmad. High gain l-band erbium-doped fiber amplifier with two-stage double-pass configuration. *Pramana*, 61(1):93–97, 2003.